SANDIA REPORT

SAND90—3165 • UC—814
Unlimited Release
Printed December 1991

Yucca Mountain Site Characterization Project

PACE-90 Water and Solute Transport Calculations for 0.01, 0.1, and 0.5 mm/yr Infiltration into Yucca Mountain

R. C. Dykhuizen, R. R. Eaton, P. L. Hopkins, M. J. Martinez

Prepared by
Sandia National Laboratories
Albuquerque, New Mexico 87185 and Livermore, California 94550
for the United States Department of Energy
under Contract DE-AC04-76DP00789

"Prepared by Yucca Mountain Site Characterization Project (YMSCP) participants as part of the Civilian Radioactive Waste Management Program (CRWM). The YMSCP is managed by the Yucca Mountain Project Office of the U.S. Department of Energy, DOE Field Office, Nevada (DOE/NV). YMSCP work is sponsored by the Office of Geologic Repositories (OGR) of the DOE Office of Civilian Radioactive Waste Management (OCRWM)."

Issued by Sandia National Laboratories, operated for the United States Department of Energy by Sandia Corporation.

Available to DOE and DOE contractors from
Office of Scientific and Technical Information
PO Box 62
Oak Ridge, TN 37831

Prices available from (615) 576-8401, FTS 626-8401

Available to the public from
National Technical Information Service
US Department of Commerce
5285 Port Royal Rd
Springfield, VA 22161

NTIS price codes
Printed copy: A05
Microfiche copy: A01

SAND90-3165
Unlimited Release
Printed December 1991

Distribution
Category UC-814

PACE-90 Water and Solute Transport Calculations for 0.01, 0.1, and 0.5 mm/yr Infiltration into Yucca Mountain

R. C. Dykhuizen, R. R. Eaton, P. L. Hopkins, and M. J. Martinez

Fluid and Thermal Sciences Department
Sandia National Laboratories
Albuquerque, New Mexico 87185

Abstract

Numerical results are presented for the Performance Assessment Calculational Exercise (PACE-90). One- and two-dimensional water and solute transport are presented for steady infiltration into Yucca Mountain. Evenly distributed infiltration rates of 0.01, 0.1, and 0.5 mm/yr were considered. The calculations of solute transport show that significant amounts of radionuclides can reach the water table over 100,000 yr at the 0.5 mm/yr rate. For time periods less than 10,000 yr or infiltrations less than 0.1 mm/yr very little solute reaches the water table. The numerical simulations clearly demonstrate that multi-dimensional effects can result in significant decreases in the travel time of solute through the modeled domain. Dual continuum effects are shown to be negligible for the low steady state fluxes considered. However, material heterogeneities may cause local amplification of the flux level in multi-dimensional flows. These higher flux levels may then require modeling of a dual continuum porous medium.

The work contained in this report pertains to WBS Element 1.2.1.4.9.

Contents

Figures

Tables

1 Introduction

The Yucca Mountain Site Characterization Project (YMP) requested our participation in the Performance Assessment Calculational Exercise (PACE-90). This effort was initiated by Department of Energy (DOE) Headquarters to identify the readiness of various computer codes and their sponsors to perform calculations in support of site performance issues relating to licensing regulations. Participants in this effort include Pacific Northwest Laboratory, Los Alamos National Laboratory, and Sandia National Laboratories (SNL) Organizations 1510, 6312, and 6416. The set of problems to be addressed were not fully defined; therefore, this exercise is not benchmarking (*i.e.*, code-to-code comparison) but involves modeler interpretation of the proposed problems. The analyses consider one- and two-dimensional steady flow and subsequent transport of representative radionuclides for a time period of 100,000 yr. Material properties have been supplied for 4 drillholes (G-1, H-1, G-4, and UE-25a), each with approximately 20 different hydrologic layers identified. The material properties used in the calculations were compiled by Merlin Wheeler of Los Alamos Technical Associates, Inc., and are given in Appendix A. Material properties for a total of 22 hydrological units were given. Retention parameters for four radionuclides were defined. The repository and water table elevations were given, along with suggested infiltration rates at the top of the Tpt-TM Unit (elevation of 1200.6 m at Hole G-4) of 0.01 mm/yr for the base case and 0.1, and 0.5 mm/yr for the perturbed cases. The lateral water diversion that would be expected to occur above the Tpc-BT/Tpt-TM interface (elevation of 1200.6 m at Hole G-4) is outside of the domain used in this study.

This report contains four major sections. The first discusses the one-dimensional hydrology results. The two-dimensional hydrology results, and comparisons between one and two dimensions are presented in the second section. The third section contains one- and two-dimensional solute transport results obtained by assuming pressure equilibrium between the fractures and the matrix. The fourth section describes a one-dimensional dual continuum model used to calculate solute transport. Here, transport is calculated in both the fractures and matrix. These results are compared with the equilibrium results.

2 One-Dimensional Hydrology

The one-dimensional, steady flow analyses were well defined. The numerical code LLUVIA (Hopkins and Eaton, 1990) was used to compute the pressure field, matrix saturation, fracture saturation, water velocity in the matrix, and water velocity in the fractures at the nominal infiltration rate of 0.01 mm/yr and for the perturbed cases, 0.1 and 0.5 mm/yr. An alternate solution file was also written for use in subsequent transport calculations. The quantities of interest for transport are matrix and fracture moisture contents and fluxes. Minimum groundwater travel times, based on the fastest (matrix or fracture) average linear fluid velocity, were also computed.

LLUVIA was developed to efficiently solve a particular class of flow problems. The isothermal problem involves the steady flux of an incompressible, Newtonian fluid through a one-dimensional domain of saturated or partially saturated layers of porous media. The media may contain fractures whose properties vary from those of the matrix. The composite matrix/fracture model representation treats the material as a single continuum in solving for the pressure field (Peters and Klavetter, 1988). The first-order differential equation describing such a flow is Darcy's equation. Conservation of mass is ensured by the imposed steady-state condition, and Darcy's equation is a statement of momentum balance. The implicit solution procedure DEBDF (Shampine and Watts, 1980) uses a backward differentiation formula of orders one through five. It is particularly well suited to the solution of nonlinear problems. The specified flux or infiltration rate is an imposed condition and is constant throughout the domain. The pressure field is computed by the solution of Richards' equation. The converged solution also allows output of hydraulic conductivities, saturations, water velocities in both the matrix and fractures (if present) and minimum groundwater travel times. In these calculations, the matrix and fractures are treated as separate continua.

The average linear water velocity is the Darcy flux, v, divided by the area through which the water moves. It is assumed that the water present at residual saturation does not contribute to the effective flow area. This formulation is taken from Dudley, *et al.* (1988).

$$a_m = \frac{v_m}{n_m(S_m - S_{m,r})} = -K_m \cdot \nabla(\psi + z)\left[\frac{1}{n_m(S_m - S_{m,r})}\right] \text{ , and} \quad (1)$$

$$a_f = \frac{v_f}{n_f(S_f - S_{f,r})} = -K_f \cdot \nabla(\psi + z)\left[\frac{1}{n_f(S_f - S_{f,r})}\right] \text{ ,} \quad (2)$$

where

a is the average linear velocity,
v is the darcy velocity,
n is the porosity,
S is the saturation,

S_r is the residual saturation,
K is the bulk saturated conductivity,
ψ is the pressure head,
z is the elevation, and
m, f are subscripts referring to the matrix and fractures.

The detailed stratigraphy of each of the four drillholes was employed. The domain modeled for each hole was from the given water table location to the top of the Tpt-TM unit. The number of nodal points at which the solution is to be reported does not affect the accuracy of the computed pressures because the DEBDF solver will compute a solution at subintervals as needed. Only the subsequent calculation of groundwater travel times is affected by nodal spacing because it is based on average linear fluid velocities between nodes. For the PACE problems, the number of nodes ranged from 268 (UE-25a) to 357 (G-1). These nodes were evenly spaced within each unit and were approximately 1.5 m apart.

The requested output quantities are presented graphically. Results from all three infiltration rates are shown in each figure for ease of comparison. Figures 1 through 4 show the pressure head profiles for the four drillholes. The similarities in material properties between Holes G-1 and H-1 and between Holes G-4 and UE-25a, as well as the differences in elevations of the units, are apparent in these figures. Matrix saturations are shown in Figures 5 through 8. Minimum saturation values increase from a range of 0.35 to 0.65 for the nominal case to 0.88 to 0.91 at 0.10 mm/yr and 0.92 to 0.99 at 0.5 mm/yr. At 0.10 mm/yr, significant increases in fracture saturation occur in layers Tpt-TDL and Tpt-TN for all holes (These units are easily identified as the ones having a non-zero fracture saturation in Figures 9 through 12 at the 0.1 mm/yr infiltration rate). At 0.5 mm/yr, the fracture saturation in these units increases and extends into neighboring units. In general, saturation of the fractures occurs when the infiltration rate approaches the saturated matrix conductivity of a rock unit. Water velocities in the matrix and in the fractures are shown in Figures 13 through 20 (positive values indicate a downward velocity). Trends in water velocities within a unit are more difficult to predict. They are a function of two nonlinear quantities, the flux and saturation, and vary over orders of magnitude.

Minimum groundwater travel times, based on the fastest (matrix or fracture) average linear fluid velocity, were also computed and are shown in Table 1. The travel times range from approximately 19,000 to 5,000,000 yr.

Table 1. GROUNDWATER TRAVEL TIMES (yr) FROM 229.4 m ABOVE WATER TABLE

Hole	q = 0.01 mm/yr	= 0.1 mm/yr	= 0.5 mm/yr
G-1	5.0×10^6	5.3×10^5	1.9×10^4
H-1	4.6×10^6	5.2×10^5	2.9×10^4
G-4	4.2×10^6	4.0×10^5	1.9×10^4
UE-25a	2.9×10^6	3.0×10^5	3.1×10^4

3 Two-Dimensional Hydrology

Two-dimensional solutions for the cross section lying between Drillholes G-4 and UE-25a were calculated using the single phase version (NORIA-SP) of the finite-element code NORIA (Hopkins *et al.*, 1991). This code solves the nonlinear, parabolic, partial differential equation (Richards equation),

$$C_p \frac{\partial P}{\partial t} - \nabla \cdot (K \nabla P) = 0 \ , \tag{3}$$

where

C_p is the moisture capacitance,
P is the effective pressure $\rho g(\psi + z)$, and
K is the hydraulic conductivity.

Steady-state solutions are obtained by calculating a transient solution to reach a steady state. The numerical procedure uses the standard Galerkin finite element method to handle spatial discretization of two-dimensional domains with either planar symmetry or axial symmetry. Time integration is performed by a second-order predictor-corrector scheme that uses error estimates to adjust time-step size automatically to maintain uniform local time truncation error throughout the calculation. Thus, the user is not required to select time-step size except at the first time step. Nearly all material properties, such as permeability, can either be set to constant values or can be defined as functions of the dependent and independent variables by user-supplied subroutines.

Nine different material regions were considered. The geometry of the material outlines is given in Figure 21. All of the material layers defined in the problem definition outline were used down through the Tpt-TN layer. This is a layer that results in appreciable lateral flow. The nine layers below that interface have been lumped together by averaging the material properties to result in a single layer. It was felt that the inclusion of these layers, some of which are less than 1 m thick, would add unnecessary complexity to the problem as these layers do not vary appreciably in their hydraulic properties. A total of 1,260 quadrilateral elements were used (Figure 22). A static initial condition was used (P=constant). The right and left boundaries were specified to be zero flux boundaries. The bottom boundary was held at a pore pressure of zero meters to represent the water table. The top boundary was held at a specified uniform infiltration flux, 0.01, 0.1 and 0.5 mm/yr.

Approximately 3 CRAY XMP hours were required to reach the steady-state condition for the 0.01 mm/yr case, 10 hours for the 0.1 mm/yr case and approximately 30 hr were required to obtain a quasi-steady state solution for the 0.5 mm/yr case. In this case, the pressure solution at the final time (7×10^{12} s) continued to oscillate slightly with time. This oscillation appeared to have no appreciable effect on the moisture saturation distribution, but did slightly affect the resulting velocity distribution. The computer

time requirements increase for the higher infiltration cases because of the additional fracture flow. As the fractures saturate, the equations being solved become more nonlinear because of the extreme variation in moisture capacitance and permeability. Figures 23 through 26 show the steady-state material saturation profiles from the water table to the top of the computed region for the 0.01 and 0.1 mm/yr case. These distributions agree well with the one-dimensional results given in Figures 7 and 8. As a result of lateral water flow, the two-dimensional calculations show a slightly dryer profile below the Tpt-TNV stratum at Hole G-4 and a wetter profile in the down-dip direction, Hole UE-25a (see Figure 21 for the locations of the the geologic layers). The vertical Darcy flux at two horizontal planes (top and bottom) is given in Figures 27 through 29 for the 0.01, 0.1, and 0.5 mm/yr cases. There is no appreciable lateral flow above the Tpt-TNV strata. Below this level, the flux near the right boundary is approximately two orders of magnitude larger on the down-dip side (as compared to the up-dip side). The water velocity vectors and the particle pathlines for the three cases given in Figures 30 through 33 show that there is relatively little water diversion through the region above the Tpt-TNV layer. A considerable amount of lateral diversion of the infiltrating water was calculated below this region even for the low infiltration case (0.01 mm/yr). This is because the saturated conductivity between layers differs by 6 orders of magnitude.

It appears that the 6-order variation in hydraulic conductivity between the Tpt-TV, Tpt-TNV, and Tpt-TN layers is the dominating hydraulic feature which affects these calculations. Earlier studies done by Prindle and Hopkins (1989) show a similar diversion phenomenon when they considered the Tpc-BT/Tpt-TM interface (this is outside of the domain used in this study). To obtain realistic calculations of the hydrologic patterns in the mountain, it will be necessary to understand and predict dissimilar regions such as these.

The effect of geologic dip on particle travel times is summarized in Table 2. The travel times calculated using one-dimensional geometry at the G-4 and UE-25a holes are given for comparison purposes. Near the right boundary, or down-dip side, particle travel times calculated for the two-dimensional cases are shorter than the one-dimensional calculations for the UE-25a hole, even though the paths are considerably longer. The smaller times result from the fact that the down-dip diversion increases the amount of fracture flow along the right boundary and in general, particle velocities in fractures are significantly larger than particle velocities in matrix.

In all cases, the travel times calculated using one-dimensional geometries are within a factor of two of the times calculated using two-dimensional geometries. This agreement is somewhat closer than one might predict from casual observation of the pathline geometries. This should not be considered the norm for all scenarios. In this case, the lateral diversion, and the resulting switch to fracture flow, occurs half way down the mesh. Therefore, the time required to traverse the upper portion of the mesh is hardly changed. The results of Prindle and Hopkins (1989) show much larger differences between one- and two-dimensional flow simulations. In their problem, the lateral diversion

occured above the repository, and the entire flow field from the repository to the water table was affected.

Table 2. TRAVEL TIMES (yr) FOR ONE- AND TWO-DIMENSIONAL GEOMETRIES (SEE FIGURE 32 FOR PATHLINE LOCATIONS)

Pathline Location	q = 0.01 mm/yr	= 0.1 mm/yr	= 0.5 mm/yr
Hole G-4 (1-D results)	4.2×10^6	4.0×10^5	1.9×10^4
a (2-D)	6.4×10^6	2.7×10^5	2.2×10^4
b (2-D)	2.3×10^6	1.6×10^5	2.1×10^4
c (2-D)	1.7×10^6	1.5×10^5	2.7×10^4
d (2-D)	1.5×10^6	1.4×10^5	1.9×10^4
Hole UE-25a (1-D results)	2.9×10^6	3.0×10^5	3.1×10^4

4 One- and Two-Dimensional Single-Continuum Solute Transport

The two-dimensional finite element code FEMTRAN (Martinez, 1985) was used to compute the transport of solutes, using the steady one- and two-dimensional flow fields computed with LLUVIA and NORIA-SP, respectively. FEMTRAN is a single-continuum model and hence cannot use the separate matrix and fracture fluxes computed by the hydrologic codes, both of which assume fracture and matrix pore pressure equilibrium. The two fluxes were summed to form the single-continuum flux used in the FEMTRAN simulations.

Both one- and two-dimensional solutions were computed with FEMTRAN in order to compare differences in dimensionality. The next section presents results obtained with a one-dimensional dual continuum code that accounts for the increased fracture velocities. The one-dimensional results obtained with FEMTRAN are also compared to the limiting case of infinite coupling in the dual continuum model to help verify that code.

Details of the transport equations solved by FEMTRAN and their numerical treatment can be found in the user's manual; however, for completeness the mathematical model is displayed below:

$$(\theta + \rho_s K_d)\frac{\partial C}{\partial t} + v_i \frac{\partial C}{\partial x_i} - \frac{\partial}{\partial x_i}\left(\theta D_{ij}\frac{\partial C}{\partial x_j}\right) + \lambda(\theta + \rho_s K_d)C = 0 \ , \tag{4}$$

where

θ is the moisture content,
ρ_s is the bulk rock density,
K_d is the distribution coefficient,
D_{ij} is the diffusion/dispersion tensor,
λ is the radioactive decay constant,
C is the liquid solute concentration, and
$v = -K(\psi)\nabla P$.

Repeated indices denote summation. The dispersion/diffusion tensor is defined by

$$\theta D_{ij} = \left(a_T v + \theta\frac{D^*}{\tau}\right)\delta_{ij} + (a_L - a_T)\, v_i v_j / v \ , \tag{5}$$

where

$v = (v_i v_i)^{\frac{1}{2}}$ is the Darcy flux magnitude,
D^* is the solute diffusion coefficient, and
a_L and a_T denote longitudinal and transverse dispersivities, respectively.

FEMTRAN uses bilinear basis functions defined on 2x2 quadrilaterals for discretizing the spatial terms in the transport equation via Galerkin's method of weighted residuals. Element calculation of the coefficient matrices are computed with 4-point Gauss-Legendre quadrature. The resulting system of ordinary differential equations describing the time history at all basis points is integrated with the implicit second-order trapezoid rule (Crank-Nicolson scheme).

In order to use the hydrologic fields generated by LLUVIA and NORIA-SP for the transport computation, they must first be translated into a format suitable for FEMTRAN. A translation subroutine was written for LLUVIA and NORIA-SP to enable output in FEMTRAN-compatible format. The computational domain in both the one- and two-dimensional simulations included the region between the repository and the water table. All 1-D simulations were along well G-4 and included all the layers described in the LLUVIA simulations discussed earlier. The 2-D simulations modeled the planar region between G-4 and UE-25a and included the region between the water table and the lower boundary of the repository. Hence, the upper boundary in the computational mesh for transport is the line extending from elevation 966m at G-4 to elevation 903m at UE-25a, see Figures 21 and 22. Because the repository horizon resides in the Tpt-TML, the computational mesh includes the part of this unit that resides below the repository together with the remaining units shown in Figure 21.

For both the one- and two-dimensional problems, zero-flux boundaries were specified along the vertical sides of the mesh and the concentration was specified as zero along the water table. This latter condition models an infinite dilution of solutes transported to the water table. A "Robin" (mixed) boundary condition, equal to the release rate provided, was applied at the upper boundary in the 1-D simulations. The release rate was also specified along the first 680 m (along the top) of the two-dimensional mesh extending from G-4, with the remainder specified as zero-flux. In order to obtain comparable concentrations between one- and two-dimensional results, the release rates were converted to flux rates by dividing the total release rates by the repository area, 5.61 x 10^2 m^2.

The two-dimensional cases were run on the CRAY XMP and required about 4 CPU minutes. The one-dimensional case was run on the VAX 8600 and required about 10–15 CPU minutes.

Before presenting the results, it is instructive to estimate the response that is expected. The following equation estimates the average (one-dimensional) advected distance that the solute will travel in a specified time period t (100,000 yr for this estimate), given an infiltration rate v:

$$X_c = \frac{vt}{(\theta + \rho_s K_d)} \; . \tag{6}$$

Estimates from the above equation are obtained using a representative moisture

content of 0.2 and a matrix density of 2.0 g/cc and are presented in Table 3. From this table, we see that only the nonreactive radionuclides ($K_d = 0$) are advected to the water table (an X_c value greater than 230 m) within the 100,000-yr time period, and that this is only possible for the 0.5 mm/yr infiltration flux.

These estimates assume that the solute is distributed between the matrix and the fractures, which is consistent with the assumptions in the FEMTRAN calculations. The estimates (and the FEMTRAN calculations) will be accurate when the flow is through the matrix subsystem or when very good coupling exists between the matrix and fracture flow subsystems. The solute may be advected farther when fracture flow exists and the coupling is weak. This point is investigated in the next section.

It is instructive to compare this model of the advected distance to one based on a model similar to the one used in Section 2 to obtain minimum groundwater travel times. The obvious difference is the assumption made in Section 2 that the solute particle is not reactive, and will choose the fastest local path (through the fastest flow subsystem). A less obvious difference is the use of the residual saturation parameter in Section 2. In Section 2, the residual saturation level is implicitly assumed to represent dead end pores. It is also assumed that the solute may not diffuse into these dead end pores. This is consistent with the intent of obtaining a minimum groundwater travel time; however, it may not be realistic when considering solute motion in a 100,000 year transient. In the estimate provided here, and in the numerical calculations in this section the solute is assumed to be distributed through the entire moisture content of the domain. In the numerical calculations of the next section, the solute is distributed through the entire moisture content of each of the two flow subsystems, but the coupling between the flow subsystems is explicitly modeled.

Table 3 estimates only the distance that the average solute ion would advect in 100,000 yr. The diffusion/dispersion of the solute will result in some solute traveling farther and some not as far as this average distance. A diffusion/dispersion distance can also be estimated to determine how much the solute can vary from this average. This diffusion/dispersion distance is estimated from the following equation:

$$X_d = \sqrt{2 D_e t} \ , \tag{7}$$

where D_e is the effective diffusion coefficient, estimated here to be

$$D_e = \frac{(\theta_m D^* / \tau_s + \alpha_L v)}{(\theta_m + \rho_s K_d)} \ . \tag{8}$$

To determine the relative importance of the advection versus the diffusion motion, the Peclet number is formed. When the advected distance is used as the length scale,

the Peclet number is found to be double the square of the ratio of the advected distance over the diffused distance:

$$P_E = \frac{V_e X_c}{D_e} = 2\left(\frac{X_c}{X_d}\right)^2 , \tag{9}$$

where V_e is the effective velocity

$$V_e = \frac{X_c}{t} = \frac{v}{(\theta_m + \rho_s K_d)} . \tag{10}$$

Note that this Peclet number is based on the advected distance. Because this distance increases with time, all flows are advection dominated in the limit of large times. However, as shown in Table 3, many of the flow conditions considered are dominated by diffusion, even for the 100,000-yr transient considered.

It is instructive to examine the Peclet number in the limit of high infiltrations. Here, the diffusion/dispersion coefficient is dominated by dispersion and the Peclet number has a very simple form

$$P_E = \frac{vt}{\alpha_L (\theta_m + \rho_s K_d)} = \frac{X_c}{\alpha_L} . \tag{11}$$

The above equation demonstrates how higher retarded solutes will show more diffusive motion than advected motion. This will be shown by example in all flows, not only the ones that are dominated by dispersion.

Time-dependent source terms for I-129, Tc-99, Cs-135, and Np-237, for 6 cases, are given in Figures 34 through 37, respectively. Each case represents a different release scenario. The first four cases were provided by Pacific Northwest Laboratory and represent variations of the continuous liquid diffusion release. The last two cases were provided by Lawrence Livermore National Laboratory, and represent a liquid drip contact. The different cases can be reclassified into two distinct sets. The first set, which is illustrated by Cases 1, 2, and 4 in Figure 35, show a steady release over the 100,000 yr transient. The second case, which is illustrated by Cases 3, 5, and 6, show a quick pulse release (relative to the 100,000-yr transient). The computed results of cases within these two sets are very similar, so only representative results will be presented. Simulations for I-129, Tc-99, and Np-237 were computed with FEMTRAN for several variations of parameters. Only a limited number of parameter variations were considered; however, the variations were chosen to be representative of the entire parameter range specified for PACE. In particular, only two different release rate cases were considered: Cases 3 and 4. These two release cases are fairly representative of all of the 6 cases specified. One-dimensional solutions were obtained only for the 0.5 mm/yr infiltration rate at Hole G-4

Table 3. COMPARISON OF ADVECTION AND DIFFUSION OF SOLUTE

Infiltration Rate (mm/yr)	K_d	X_c (m)	X_d (m)	P_E
0.01	0	5.00	27.0	0.068
	1	0.455	8.1	0.006
	10	0.050	2.7	0.0007
	100	0.005	0.85	0.0001
0.10	0	50.0	40.	3.07
	1	4.55	12.	0.28
	10	0.50	4.0	0.030
	100	0.05	1.3	0.003
0.50	0	250.	75.0	22.0
	1	22.7	23.0	2.0
	10	2.48	7.5	0.22
	100	0.25	2.4	0.02

using the hydrologic field computed with LLUVIA, which includes all material layers. This mesh included 188 4-node elements between the water table and the repository. Two-dimensional solutions were obtained for the 0.01, 0.1, and 0.5 mm/yr infiltration rates. As discussed earlier, the two-dimensional mesh used with FEMTRAN is a subset of the mesh defined for the hydrologic simulations using NORIA-SP. The FEMTRAN mesh included 720 elements and 775 node points between the water table and the repository. The parameters used in the FEMTRAN simulations are listed in Table 4 for the matrix pores. The tortuosity (τ) was assumed independent of the saturation level and α_T was assumed equal to $\alpha_L/2$ in the two-dimensional problem.

The nuclide Tc-99 is sorbed in the Tpt-TML, Tpt-TM, and Tpt-TV (Appendix A). Since the distribution coefficient is identical in the Tpt-TML and Tpt-TM, these two units were combined for purposes of specifing sorption properties; a bulk density of 2.30 g/cm^3 was specified for both layers (This simplification was also used in the Np-237 calculations). Note, however, that the moisture content is specified by the hydrologic solution and hence the distinct porosities between the units are included.

The numerical simulations for the 0.01 mm/yr infiltration rate resulted in little

Table 4. PARAMETER VALUES USED IN TRANSPORT MODELS

	Matrix	Fracture
τ_s	10	1
α_L	10 m	10 m
D^*	10^{-9} m ^{2}/s	10^{-9} m^2/s

motion of any solute (in either the one- or two-dimensional geometries). Because the solute remained in the region near the repository, where the flow is well represented by a one-dimensional flow, the one- and two-dimensional results were almost identical. Some results for the 0.01 mm/yr infiltration using the dual continuum code are presented in the next section. They are almost identical to the FEMTRAN results because the groundwater flow near the repository for this case is entirely through the matrix flow subsystem. Amounts discharged to the water table for the 0.1 mm/yr and the 0.5 mm/yr infiltration cases are summarized in Table 5. Other entries in Table 5 will be explained below.

Figures 38 and 39 show the distribution of I-129 (curie/m^3) in the G-4/UE-25a cross section for q = 0.1 mm/yr and the Case 3 and 4 release rates, respectively. The figures indicate that the I-129, which is not sorbed, travels more or less vertically downward from the repository until the solute body reaches the Tpt-TNV layer which results in significant lateral diversion of moisture and of solute. The cumulative discharge history is shown in Figure 40 for both Case 3 and 4 release models (the Case 4 release is more uniform in time than the Case 3 release as shown in Figure 34). These values were obtained by multiplying the discharge obtained from the two-dimensional solution by the ratio of total repository area (5.61 x 10^6 m^2) to the repository area represented in the two-dimensional model (681 x 1 m^2). Discharge values, for both one-dimensional and two-dimensional geometries, were obtained in a similar manner in order to obtain values which are representative of the total amount of the nuclides that would be discharged by the entire repository. Case 3 results in a total discharge of about 154 curie while Case 4 results in about 28 curie. Both of these values are a relatively small fraction of the source term, which is about 2,280 curie for Case 3 and 2,231 curie for Case 4. The amount of I-129 decayed can by approximated from the values in Table 5 by subtracting the amounts in the last three columns from the amount in the source term column.

I-129 is transported much further for the 0.5 mm/yr infiltration rate, as shown in Figures 41 and 42 for Case 3 in the two-dimensional cross section. As indicated in Table 5, about 62% of the integrated release is discharged to the water table for this infiltration rate. Figure 42 indicates much lower concentration values as compared to Figure 38

Table 5. TRANSPORT RESULTS USING FEMTRAN IN 100,000 YEARS

Nuclide	Release Case	Dimension	Source Term Release (Ci)	Discharge to Water Table (Ci)	Dissolved Content (Ci)	Adsorbed Content (Ci)
q=0.1 mm/yr						
I-129	3	2-D	2278	154	2020	0.0
	4	2-D	2231	28	2164	0.0
TC-99	3	2-D	9.85×10^{5}	0.0	2.10×10^{5}	5.05×10^{5}
	4	2-D	6.86×10^{5}	0.0	1.77×10^{5}	4.10×10^{5}
q=0.5 mm/yr						
I-129	3	1-D	2278	1285	941	0.0
		2-D	2278	1414	708	0.0
	4	1-D	2231	322	1882	0.0
		2-D	2231	915	1213	0.0
TC-99	3	1-D	9.85×10^{5}	1.04×10^{5}	5.54×10^{5}	6.26×10^{4}
	3	2-D	9.85×10^{5}	3.64×10^{5}	3.04×10^{5}	6.79×10^{4}
	4	2-D	6.83×10^{5}	8.32×10^{4}	2.31×10^{5}	2.62×10^{5}
NP-237	3	1-D	0.125	0.0	1.24×10^{-3}	0.119

for q = 0.1 mm/yr. The sequence of contour plots in Figures 43 through 46 illustrate the arrival of I-129 at the Tpt-TNV layer, and the subsequent lateral transport to Hole UE-25a and finally down to the water table. The I-129 travels vertically down from the repository until it arrives at the Tpt-TNV after about 10,000 yr. In a relatively short span of another 8,000 years, a significant discharge to the water table is obtained as a result of the rapid lateral transport along the Tpt-TNV to Hole UE-25a and finally down to the water table. The combination of the high-permeability Tpt-TNV layer and the zero-flux boundary at UE-25a result in a dominant flow mechanism which allows more rapid transport to the water table than would be obtained in a one-dimensional simulation. Profiles of concentration are compared between one- and two-dimensional solutions in Figure 47 after 100,000 yr. The two-dimensional profiles are plots of the

solute concentration distributions along the two edges of the domain (defined as the G-4 and the UE-25a well locations). The effects of lateral diversion are also evident here, resulting in very different concentration profiles. In the one-dimensional problem, the solute body moves much like a "spreading pulse," with a peak concentration which has just arrived at the water table for the present parameters. In the two-dimensional problem, the solute body moves like a pulse only until it reaches the Tpt-TNV where a significant lateral transport develops.

The distribution of I-129 at 50,000 and 100,000 yr for the Case 4 release is shown in Figure 48 and 49. The Case 4 release is relatively uniform for much of the time period and results in a much different distribution of I-129 when compared to results for Case 3 (pulse release). At 50,000 yr, the Case 4 release results in peak concentrations at the repository, while Case 3 (Figure 41 and 42) results in maximum concentration below the Tpt-TNV near the right boundary; i.e., by this time much of the I-129 has been flushed out of the Tpt-TM for Case 3, while the highest concentration is found in this layer in Case 4. At 100,000 yr, the I-129 is distributed throughout the entire region between the repository and water table (Figure 49). The concentration distribution along G-4 and UE-25a at 100,000 yr for the one-dimensional and two-dimensional solutions is shown in Figure 50. The effects of lateral diversion are clearly evident in the two-dimensional results, showing high concentration above the Tpt-TNV along G-4 and much lower below. Conversely, concentrations are highest below the Tpt-TNV at UE-25a. In contrast, the one-dimensional solution shows large concentrations throughout the interval. The cumulative discharge to the water table after 100,000 yr, is 915 curie for the two-dimensional solution compared to 322 curie for the one-dimensional solution (Table 5 and Figure 51). These discharges represent 40% and 15% of the integrated source term. Figure 51 shows the differences between first arrival time and discharge rates that are a result of pulse (Case 3) and continuous (Case 4) releases. Differences are also seen between one- and two-dimensional simulations. The discharge is always higher in the two-dimensional simulations, for either release case, due to the significant lateral diversion feature caused by Tpt-TNV layer. Futhermore, first arrival of I-129 at the water table occurs at 15,000 yr for the two-dimensional solution with Case 3 release, while first arrival is delayed until 40,000 yr in the one-dimensional geometry. Figure 42 shows that after 100,000 yr, most of the I-129 has been flushed out of the layers above the Tpt-TNV, owing to the large mobility of I-129 for this infiltration rate.

After 100,000 yr, the remaining I-129 is largely below the Tpt-TNV, transported there about equally by diffusion and advection from the layers above, and is expected to remain in these layers for some time because transport by advection and diffusion is much less vigorous in this region. This is also indicated by the much reduced discharge rate in the two-dimensional, Case 3 release curve of Figure 51.

Table 5 gives the net discharge to the water table after 100,000 yr. In addition to discharge, several balance integrals are also included in Table 5. The source release column is the integral of the release model over 100,000 yr and represents the total

amount of nuclide injected into the computational region over this time. The total dissolved content of each nuclide in the domain, Ω, at time, t, is given by

$$\int_{\Omega} \theta(\mathbf{x},t)C(\mathbf{x},t)d\Omega \ . \tag{12}$$

Table 5 also gives the total adsorbed content from

$$\int_{\Omega} \rho K_d C d\Omega \ . \tag{13}$$

An indicator of the quality of the numerical solution is obtained by performing a global material balance. By comparing the amount of material dissolved, adsorbed, decayed, and discharged to the water table with the integrated source term, we find less than 6% difference in all the cases considered, a fairly good balance given the coarseness of the mesh. The largest errors are obtained with the 0.5 mm/yr infiltration. A better comparison could be obtained with increased mesh refinement, which of course increases CPU requirements.

The distribution of Tc-99, which is sorbed in the Tpt-TML, Tpt-TM and the Tpt-TV layers (see data in Appendix A), is shown in Figures 52 and 53 for the 0.1 mm/yr infiltration rate and the Case 3 and 4 release models. As indicated, the Tc-99 is not transported to the water table over 100,000 yr, and in fact is not transported out of the sorbing layers below the repository. The ratio of adsorbed to dissolved material is about 2.4 for Case 3 and 2.3 for Case 4. Hence, no other simulations of Tc-99 for this infiltration were carried out. Because Tc-99 remains above the Tpt-TNV layer (where the lateral diversion occurs), the results are essentially one-dimensional. Also, because there is negligible fracture flow in the regions that contain Tc-99, the dual continuum results from the next section agree with the two-dimensional results obtained here.

The distribution of Tc-99 for the 0.5 mm/yr infiltration is shown in Figures 54 through 57. These figures depict the Case 3 and 4 releases, and show concentration distributions at 50,000 and 100,000 years. Note that these figures show only the liquid concentration of Tc-99 (the adsorbed amount is a factor of $\rho_b K_d$ times the liquid concentration). At 50,000 yr, a significant amount of Tc-99 is still in the Tpt-TM layer, in contrast to I-129 (Figure 41), which has been effectively flushed out of this region by this time. Effects of sorption are still evident at 100,000 yr for both releases, showing some Tc-99 in the Tpt-TM layer, whereas Figure 42 shows I-129 only in the layers below the Tpt-TM. Profiles of liquid concentration at 100,000 yr are shown in Figure 58 for Case 3 release and both one- and two-dimensional geometries. Maximum concentrations are about 50% higher in the one-dimensional profile along G-4 than for either of the two-dimensional profiles (along G-4 and UE-25a). Cumulative discharge histories are compared between one- and two-dimensional solutions and between Case 3 and 4

releases in Figure 59. For Case 3, the two-dimensional discharge after 100,000 yr is larger than the one-dimensional value by about a factor of 3.5 (Table 5). Furthermore, with respect to the amount of material remaining in the domain after 100,000 yr, the ratio of adsorbed to dissolved Tc-99 is 0.11 in the one-dimensional solution as compared to 0.22 in the two-dimensional solution. This is because a larger fraction of Tc-99 resides in the nonsorbing layers in the one-dimensional simulation.

As noted earlier, the above results show only the dissolved concentration of Tc-99. It is instructive to consider the cumulative balance integrals for the total amount dissolved, adsorbed, decayed, and discharged to the water table. These histories are shown in Figure 60 for the Case 3 release and q = 0.5 mm/yr. Up to about 50,000 yr, most of the Tc-99 is in the sorbing layers, the Tpt-TM and Tpt-TV, and Figure 60 shows the adsorbed content is as much as twice the dissolved content. In contrast, at 100,000 yr a significant fraction of the Tc-99 is in the nonsorbed layers and the balance integrals show the adsorbed amount to be 0.22 times the dissolved content. The adsorbed and dissolved content curves cross over at about 55,000 yr, indicating equal distribution between the liquid and solid when integrated over the entire computational region. Note also that the cumulative amount of Tc-99 lost by radioactive decay after 100,000 yr is about 23% of the integrated release.

Np-237 is strongly sorbed in the Tpt-TML and Tpt-TM, resulting in retardation factors of order 100. Therefore, it was determined that the two-dimensional mesh was too coarse to properly resolve the transport. Hence, only one one-dimensional simulation was performed using the LLUVIA solution for q = 0.5 mm/yr (188 elements). Concentration profiles along G-4 are shown in Figure 61 for release Case 3. Table 5 indicates that the majority of the Np-237 is sorbed onto the solid; the ratio of adsorbed to dissolved material in the domain is about 96. The Np-237 calculation presented uses the largest infiltration and the pulse release model, which offers the greatest potential for transport, and yet the Np-237 is transported less than 40 m below the repository over 100,000 yr. None of the Np-237 or the Cs-137, which is even more strongly sorbed, will be transported to the water table over 100,000 yr.

In the beginning of this section, we derived expressions that can be used to estimate the advection and dispersion of solute from the repository. However, these estimates assume a one-dimensional flow system. As we have seen, the two-dimensional simulations demonstrate the possibility that the flow may not be well represented by the one-dimensional assumption. The two-dimensional simulations result in stream tubes that are not straight or of constant width. The contraction of the stream tubes results in two effects that can increase the motion of the solute. First, the flow area is reduced, which leads directly to an increased fluid velocity. Secondly, the increased velocities in the stream tube results in higher dispersion rates. Transport by dispersion is a significant contributor to solute releases in our model.

5 One-Dimensional Dual Continuum Solute Transport

A dual continuum model was used to evaluate the effect of fracture flow on the solute transport. This model includes two flow fields through the porous medium. In regions with significant fracture flow, the solute can bypass much of the retention capabilities of the matrix pore system. This may result in solute traveling faster than the average water velocity that was used in the FEMTRAN simulations (Section 4).

Our one-dimensional dual continuum solute transport code (Dykhuizen, 1987) was modified to accept the hydrologic output from LLUVIA. This ensured internal consistency in generating the two flow fields. The code was further modified to use the more accurate matrix fracture coupling model recently developed (Dykhuizen, 1990) and in turn required incorporation of a more accurate time integrator to account for the increased stiffness of the equation set.

Flow rates on the order of .01 mm/yr did not result in significant fracture flow. Therefore, the dual continuum model would not be required. For the higher flow rates that are considered in this report, the fractures are saturated in some of the geologic layers. Thus the transport of solutes through the fracture system is of importance. However, these conditions may still not require the complexity of a dual continuum model if it is shown that the two flow subsystems are tightly coupled. A dual continuum model was therefore used to determine if the assumptions from the single continuum model in the previous section are valid. The following are the governing equations solved in the dual continuum model:

$$(\theta_m + \rho_s K_d)\frac{\partial C_m}{\partial t} - v_m\frac{\partial C_m}{\partial z} - \frac{\partial}{\partial z}\left[\theta D_m \frac{\partial C_m}{\partial z}\right] = -WC_x + \Psi - \lambda(\theta_m + \rho_s K_d)C_m \ , and \tag{14}$$

$$\theta_f\frac{\partial C_f}{\partial t} - v_f\frac{\partial C_f}{\partial z} - \frac{\partial}{\partial z}\left[\theta D_f \frac{\partial C_f}{\partial z}\right] = +WC_x - \Psi - \lambda\theta_f C_f \ , \tag{15}$$

where

θ is the moisture content,
ρ_s is the bulk rock density,
K_d is the distribution coefficient,
v is the infiltration flux (positive downward),
D is the diffusion/dispersion coefficient,
λ is the radioactive decay constant,
W is the cross flow rate,
C_x is the cross flow solute concentration,
Ψ is the cross diffusion rate, and

subscripts m and f refer to the matrix and fracture systems.

The submodels for W, C_x, and Ψ are described by Dykhuizen (1987 and 1990). They account for exchange of solute between the two flow systems.

The problem description provides ρ_s, v, λ, and K_d. It was assumed that the distribution coefficient did not vary with the saturation level; θ was obtained from the LLUVIA solution.

A model was constructed to obtain the diffusion/dispersion coefficient. This model is consistant with that used in Section 4 for multidimensional calculations. It is also presented by Freeze and Cherry (1979), but with different notation. The diffusion/dispersion coefficient using our notation is,

$$D_m = \frac{D^*}{\tau_m} + \frac{\alpha_L v_m}{\theta_m} \ , \tag{16}$$

where

τ is the tortuosity,
α_L is the dispersivity, and
D^* is the molecular diffusion coefficient of the solute in water.

The fracture subsystem diffusion/dispersion coefficient is obtained in an identical manner.

The tortuosity is often considered to be a function of the saturation level of the geologic material, with increasing tortuosity resulting from a decrease in the moisture content. A model from Burdine (1953) was used to describe this effect,

$$\tau = \frac{\tau_s}{\left[\frac{(S-S_r)}{(1-S_r)}\right]^2} \ , \tag{17}$$

where

τ_s is the saturated tortuosity,
S is the saturation level, and
S_r is the residual saturation level.

Table 4 shows the parameter values used in the above models to produce the results presented. It should be noted that these parameter values are thought to be representative; however, experimental data are required to verify these choices.

To solve the solute transport equation, boundary conditions have to be provided. The domain modeled was from the water table up to the repository elevation. The

water table location was provided in the problem statement. It was assumed that the repository would exist 30 m above the lower interface of the Tpt-TML geologic unit. A zero concentration was imposed at the lower boundary. This conservatively assumes that the water table has an infinite capacity with good mixing. A flux boundary condition was imposed at the upper boundary equal to the release rates provided. This conservatively eliminates any diffusion of the solute upward from the repository that occurs at the low infiltrations. The solute was distributed between the two flow systems at the upper boundary porportional to their respective flow rates at that location.

The one-dimensional solute transport calculations were performed for the 0.01, 0.1, and the 0.5 mm/yr infiltration conditions. The output requested was the integrated amount of each of the representative radionuclides that reached the water table in 100,000 yr. For cases where no radionuclides reach the water table, radionuclide distributions in the host rock are given.

Data were provided for the layering of geologic materials from four drillholes (G-4, G-1, H-1, and UE-25a). Also, six different release rates were specified. Finally, the distribution coefficients for four different radionuclides were provided. Because of time constraints, not all of the permutations were examined; however, enough were investigated to enable all trends to be established.

The solute concentration plots presented below are in units of curies per cubic meter of groundwater. They only display the concentration in the matrix pores for clarity. The concentrations in the fractures are typically slightly advanced in the cases where fracture flow exists. The plots do not directly show the amount of solute sorbed onto the geologic media. The plots that show the integrated release to the water table assume that all of the waste packages are the same elevation above the water table and the flow passes through the geologic layering given in the G-4 stratigraphic column. In all cases, the flow just above the water table is dominated by the fracture flow. This is because the fractures become saturated at the water table and the matrix flux goes to zero. Our multidimensional calculations potentially yield a more accurate picture of the solute transport in Yucca Mountain by representing more geometry; however, they do not account for the added dispersion caused by some of the solute traveling faster through the fracture system.

Figure 35 shows the six Tc-99 source terms provided for this exercise. All results will be presented using the layered materials found in the G-4 stratigraphy. The results are somewhat different if other stratigraphies are used. However, the major factor that determines a difference is the assumed distance to the water table that the solute has to travel. Shorter distances yield larger releases.

Figures 62 and 63 show the distribution of Tc-99 in the host rock (C_m) after 100,000 yr, for the infiltration rates of 0.01 and 0.1 mm/yr. The figure shows Tc-99 below the repository (elevation 960 m) and above the water table (elevation 730 m). Tabular values of the integrated releases to the water table (for 0.1 and 0.5 mm/yr infiltrations)

are presented in Tables 6 and 7. As can be expected, the pulse release cases result in higher displacements of the solute pulse. Figure 64 shows that some Tc-99 reaches the water table for an increased infiltration of 0.5 mm/yr. Tc-99 is only slightly retarded by the geologic medium as a result of sorption reactions in layers near the repository. At the 0.5 mm/yr infiltration, the average solute particle does not reach the water table before 150,000 yr. Therefore, the solute that does reach the water table is due to dispersion of the solute. This dispersion is due to some of the radionuclides traveling faster than the average flow velocity. Use of a dual continuum model explicitly accounts for some of this by including a fracture system with its associated higher velocities. The dispersion term within the governing equations also accounts for this effect within each flow system.

To test if the dual continuum model is required, a single continuum model was obtained from simple modifications of the computer code used to calculate the dual continuum results. By deleting the fracture flux, and increasing the matrix conductivity by accounting for the fractures, a single continuum model is created. The 0.5 mm/yr Tc-99 calculation was executed using the modified code. This results in the solute reaching the water table at an identical rate in both the dual and single continuum models. The distribution of the solute through the medium is also identical as shown in Figure 65. In the dual continuum calculations the fracture subsystem concentrations are so close to the matrix subsystem concentrations that there is no way to distinguish them on the scale of this plot. Both the dual and single continuum results agree well with those calculated by FEMTRAN in the previous section. The only difference in the models here and the one in FEMTRAN is that the dispersivity is slightly more complex in this model. Therefore, the agreement between the models here and FEMTRAN helps verify both codes.

The remaining results in this section are calculated using the full dual porosity model for consistency. However, as shown above, the added complexity is not required for the steady state fluxes used.

To test how much numerical dispersion and roundoff errors affected the results, calculations were performed with a finer mesh (double the number of nodes) and finer time steps. These results agreed very well with the standard results presented. A numerical dispersion analysis has shown that if the node size is small when compared to the dispersivity, numerical diffusion will not be a problem. The standard mesh spacing is approximately 1 m and the dispersivity is 10 m.

Figure 34 shows the various source terms for the release of I-129. This isotope is not retarded at all in any of the geologic layers. All of the release cases result in a peak in the release rate near 1,000 yr. However, the majority of the solute in Cases 1, 2, and 4 are released over an extended period. These cases are therefore classified as continuous release cases. Cases 3, 5, and 6 are the pulse release cases. Figures 66 and 67 show the distribution of I-129 for the 0.01 mm/yr and 0.1 mm/yr infiltrations, respectively. Table 6 shows that a small amount of I-129 is predicted to be released to the water table for the

0.1 mm/yr infiltration. Figure 68 shows the integrated release to the water table for the 0.5 mm/yr infiltration rates. In these figures, Case 1 is representative of the continuous release cases, and Case 6 is representative of the pulse release cases. Again, the pulse release results in more radionuclides reaching the water table.

Figure 36 shows the various source terms for the release of Cs-135. The source terms for Cases 1, 3, and 4 are identical within the zero to 100,000 yr period. These cases result in a pulse of Cs-135 within the first 5,000 yr of the transient. Cases 5 and 6 also result in a pulse release, but over a slightly longer time period. Case 2 displays a short pulse at 1,000 yr, and then a continuous release. Because of the large distribution coefficients (up to 3,000 ml/g for some geologic layers) that were provided for Cs-135, the solute does not reach the water table, even for the 0.5 mm/yr infiltration case. Figure 69 shows the distribution of the solute below the repository (elevation 960 m) and above the water table (elevation 730 m) for the six source terms. As can be seen, the Cs-135 does not travel more than 10 m.

Figure 37 shows the six source terms for the release of Np-237. The six source terms form only three distinct functions within the zero to 100,000 yr range. Np-237 is also highly retarded by the geologic materials, but not as strongly as Cs-135. No Np-237 reaches the water table for any of the proposed infiltrations. Figure 70 shows the distribution of Np-237 after 100,000 yr between the water table and the repository elevations for the 0.5 mm/yr infiltration.

Table 6. ONE-DIMENSIONAL SOLUTE TRANSPORT RESULTS FOR THE 0.1 mm/yr INFILTRATION (100,000 years)

Nuclide	Release Case	Total Released (Ci)	Transported to Water Table (Ci)	Decayed (Ci)
Tc-99	1	3.48×10^{5}	0.0	0.49×10^{5}
	2	4.10×10^{5}	0.0	0.62×10^{5}
	3	9.87×10^{5}	0.0	2.67×10^{5}
	4	6.86×10^{5}	0.0	0.98×10^{5}
	5	8.83×10^{5}	0.0	2.38×10^{5}
	6	9.53×10^{5}	0.0	2.57×10^{5}
I-129	1	1183.	3.1×10^{-3}	2.
	2	1240.		
	3	2277.		
	4	2240.		
	5	2164.		
	6	2300.	5.2×10^{-2}	10.
Np-237	1,3,4	0.125	0.0	0.0025
	2	16.11	0.0	0.27
	5,6	0.73	0.0	0.011
Cs-137	1,3,4	371.5	0.0	10.7
	2	6662.0	0.0	8.9
	5	2.37×10^{4}	0.0	0.07×10^{4}
	6	2.64×10^{4}	0.0	0.07×10^{5}

Table 7. ONE-DIMENSIONAL SOLUTE TRANSPORT RESULTS FOR THE 0.5 mm/yr INFILTRATION (100,000 years)

Nuclide	Release Case	Total Released (Ci)	Transported to Water Table (Ci)	Decayed (Ci)
Tc-99	1	3.48×10^{5}		
	2	4.10×10^{5}		
	3	9.87×10^{5}	1.15×10^{5}	2.62×10^{5}
	4	6.86×10^{5}	0.10×10^{5}	0.97×10^{5}
	5	8.83×10^{5}		
	6	9.53×10^{5}		
I-129	1	1183.0	183.	2.0
	2	1240.0		
	3	2277.0		
	4	2240.0		
	5	2164.0		
	6	2300.0	1306.	9.0
Np-237	1,3,4	0.125	0.0	0.0025
	2	16.11	0.0	0.27
	5,6	0.73	0.0	0.011
Cs-137	1,3,4	371.5	0.0	10.7
	2	6662.0	0.0	8.9
	5	2.37×10^{4}	0.0	0.07×10^{4}
	6	2.64×10^{4}	0.0	0.07×10^{4}

6 Conclusions

One- and two-dimensional solutions for hydrology and solute transport for the 0.01, 0.1, and 0.5 mm/yr infiltration rates are complete. Extremely modest amounts of computer time were required to complete the one-dimensional calculations. The two-dimensional hydrology calculations required 3, 10, and 30 hr of CRAY XMP computer time for the 0.01, 0.1, and 0.5 cases, respectively. A significant amount of lateral flow of water was computed for all cases as a result of differences in the permeability between layers, which varied by six orders of magnitude.

Calculations of solute transport show that significant amounts of radionuclides can reach the water table over 100,000 yr at the 0.5 mm/yr infiltration rate. For time periods less than 10,000 yr or infiltrations less than 0.1 mm/yr very little solute reaches the water table.

It is shown that the inclusion of a dual continuum model has negligible effect on the solute releases for the steady state flow rates considered, even when significant fracture flow exists. This is due to the high coupling terms that transfer solute between the two flow systems. However, material heterogeneities may cause local amplification of the flux level in multidimensional flows. These higher flux levels may then require modeling of a dual continuum porous medium.

It is also shown that multidimensional flows can increase the solute releases. This is due to the flow bypassing large stagnant portions of the mountain, resulting in a reduced global capacitance. (The infiltration displaces a smaller volume of water before reaching the water table, resulting in an earlier arrival.) As the volume in a streamtube decreases the average Darcy velocity, and hydrodynamic dispersion increases. Both mechanisms decrease the time to initial solute arivial at the water table. The actual results that we obtained are dependent upon our choice of the side boundary conditions, and the existence of the unbroken layering that caused the lateral diversion.

It is unlikely that one-dimensional models of solute transport will be acceptable for calculating solute transport at Yucca Mountain. If non-steady flows are considered, a dual continuum model may also be required.

Calculational costs for the one-dimensional hydrology calculations were negligible. The cost for the two-dimensional hydrology calculations proved to be much more significant. They were two orders of magnitude greater than the solute transport calculations (which used the hydrology results as an input). This is because the solute transport calculations solve a linear differential equation set.

Therefore, reductions in the cost of the solute transport calculations are not as important as reductions in the hydrology computational costs (unless many transport calculations are to be performed with the same flow field). A dual continuum solute transport code will at least double the computer time for a single continuum equivalent.

Independently, the increase in the number of geometric dimensions can increase the computer time by an order of magnitude.

The two-dimensional problem considered here is somewhat artificial as a result of imposition of zero-flux boundaries requiring the laterally diverted water to be forced down to the water table at Hole UE-25a rather than to continue along the Tpt-TNV. The assumed continuity of this highly permeable layer is also very important. However, imposition of Dirichlet conditions at side boundaries is not a better alternative. Future work should investigate use of more realistic boundary conditions.

7 References

Burdine, T. N., 1953, "Relative permeability calculations from pore size distribution data," *American Institute of Mining Engineers, Petroleum Transactions*, 198, pp 71-77. (NNA.890522.0241)

Dudley, A. L., R. R. Peters, J. H. Gauthier, M. L. Wilson, M. S. Tierney, and E. A. Klavetter, 1988, *Total Systems Performance Assessment Code (TOSPAC) Volume 1: Physical and Mathematical Bases*, SAND85-0002, Sandia National Laboratories, Albuquerque, New Mexico. (NNA.881202.0211).

Dykhuizen, R. C., 1987, "Transport of solutes through unsaturated fractured media." *Wat. Resour. Res.*, 21(12), pp 1531-1539. (NNA.890327.0047)

Dykhuizen, R. C., 1990, "A new coupling term for dual porosity models," *Wat. Resour. Res.*, 26(2), pp 351-356. (NNA.910328.0058)

Freeze, R. A., and J. A. Cherry, 1979, *Groundwater*, Prentice Hall, Englewood Cliffs, NJ. (NNA.870406.0444)

Hopkins, P. L., and R. R. Eaton, 1990, *LLUVIA: A Program for One-Dimensional, Steady-State Flow Through Partially Saturated Porous Media*, SAND88-0558, Sandia National Laboratories, Albuquerque, NM. (NNA.900406.0001)

Hopkins, P. L., N. E. Bixler, and R. R. Eaton, 1991, *NORIA-SP—A Finite Element Computer Program for Analyzing Liquid Water Transport in Porous Media*, SAND90–2542, Sandia National Laboratories, Albuquerque, NM. (NNA.911202.0031)

Martinez, M. J., 1985, *FEMTRAN – A Finite Element Computer Program for Simulating Radionuclide Transport Through Porous Media*, SAND84-0747, Sandia National Laboratories, Albuquerque, NM. (NNA.870728.0029)

Peters, R. R., and E. A. Klavetter, 1988, "A Continuum Model for Water Movement in an Unsaturated Fractured Rock Mass," *Water Resour. Res.*, 24(3), pp. 416-430. (NNA.870323.0453).

Prindle, R. W., and P. L. Hopkins, 1989, *On Conditions and Parameters Important to Model Sensitivity for Unsaturated Flow Through Layered, Fractured Tuff: Results of Analysis for HYDROCOIN Level 3 Case 2*, SAND89-0652, Sandia National Laboratories, Albuquerque, NM. (NNA.900523.0211)

Shampine, L. F. and H. A. Watts, 1980, *DEPAC–Design of a User Oriented Package of ODE Solvers*, SAND79-2374, Sandia National Laboratories, Albuquerque, NM. (NNA.900122.0001)

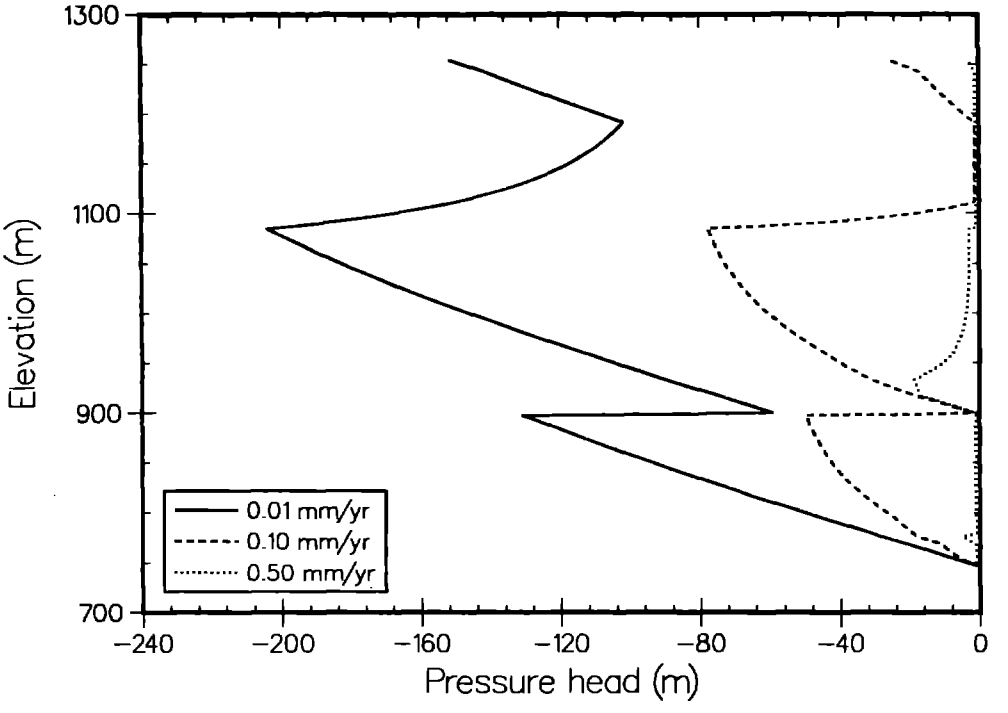

Figure 1. Pressure head for hole G-1.

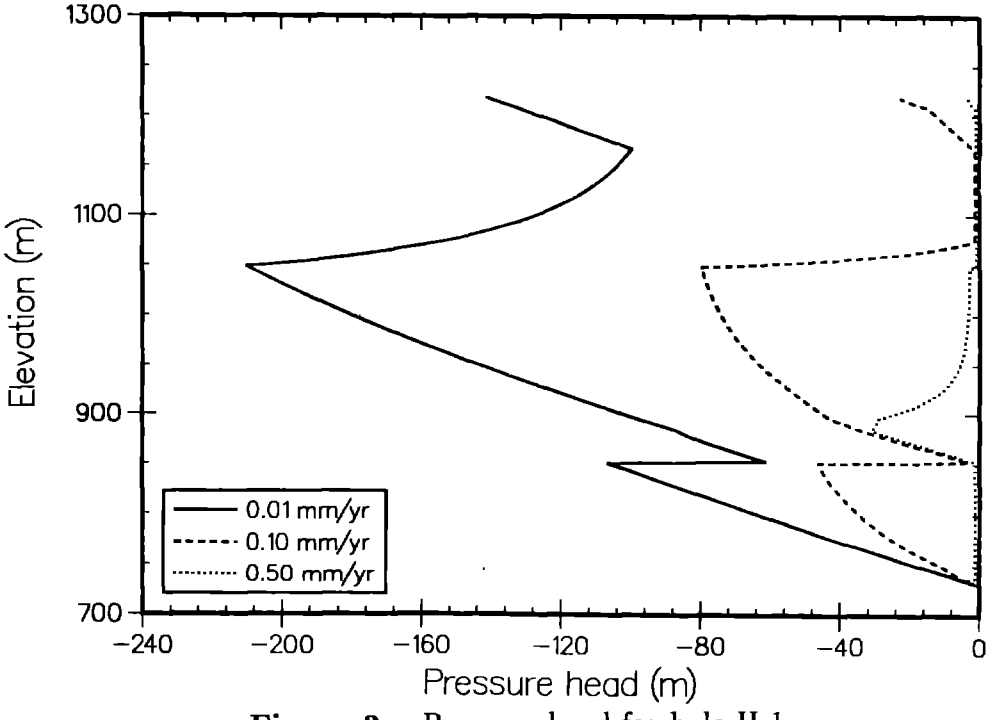

Figure 2. Pressure head for hole H-1.

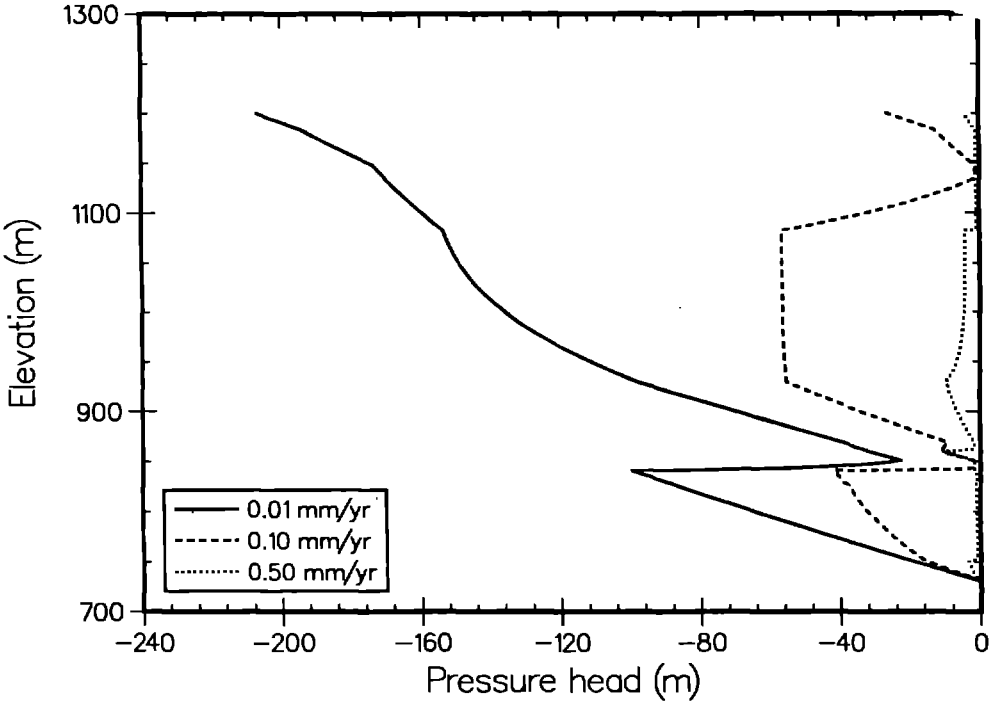

Figure 3. Pressure head for hole G-4.

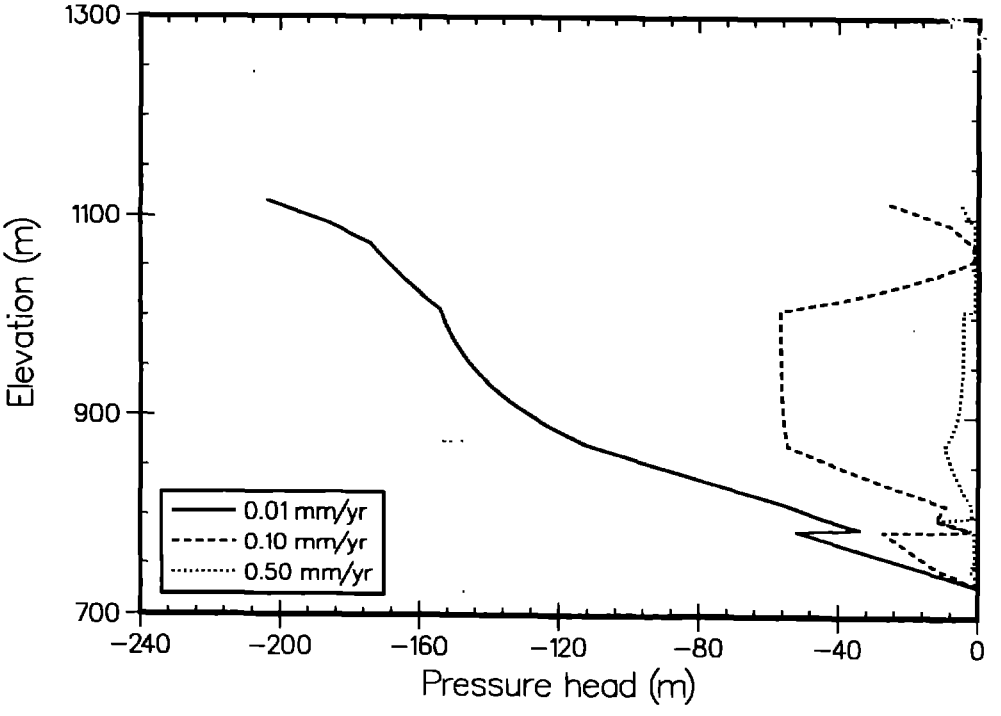

Figure 4. Pressure head for hole UE-25a.

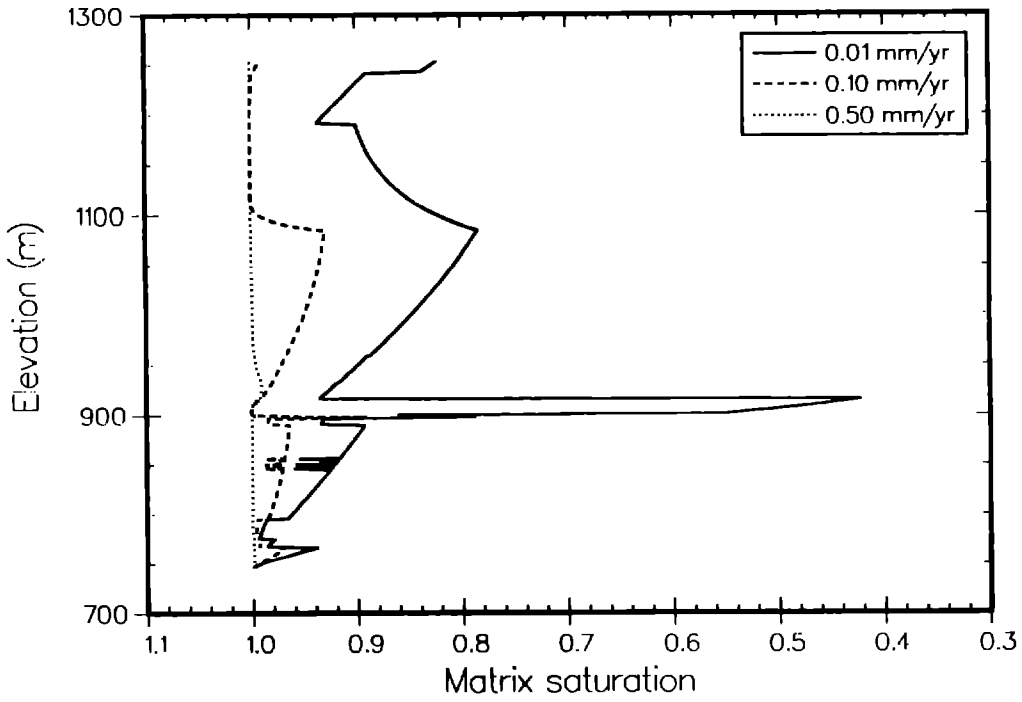

Figure 5. Matrix saturation for hole G-1.

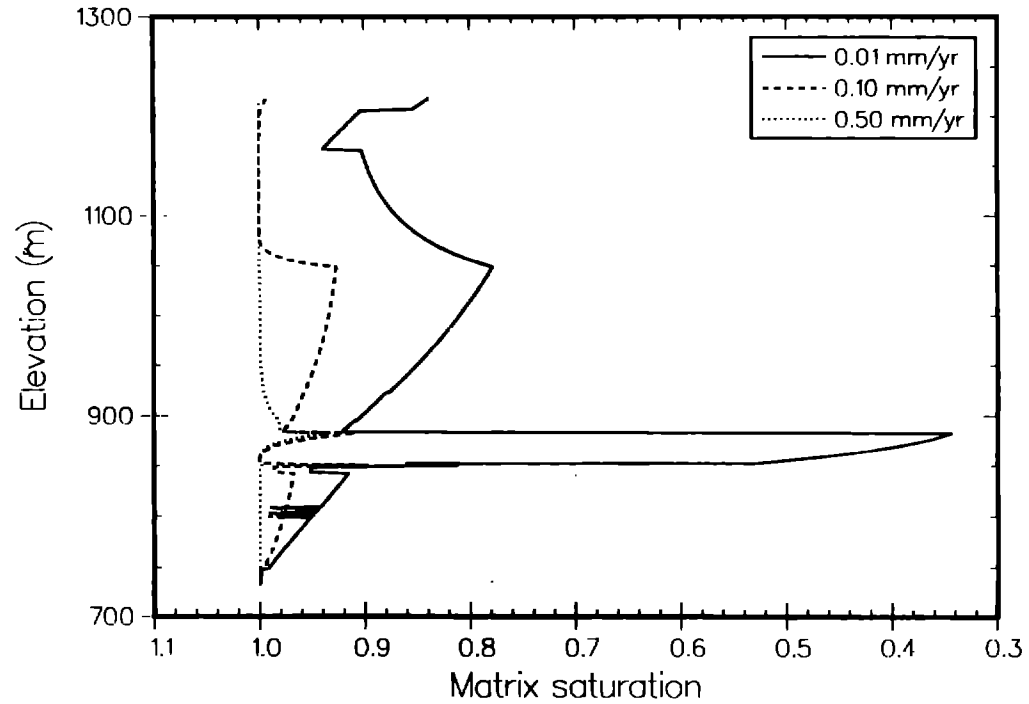

Figure 6. Matrix saturation for hole H-1.

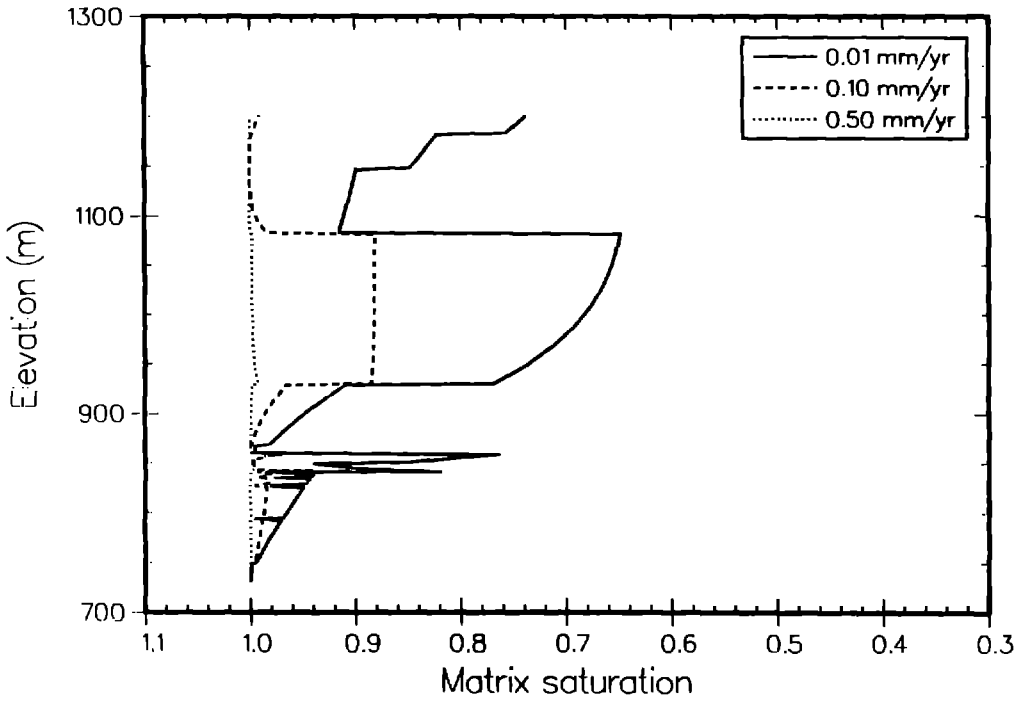

Figure 7. Matrix saturation for hole G-4.

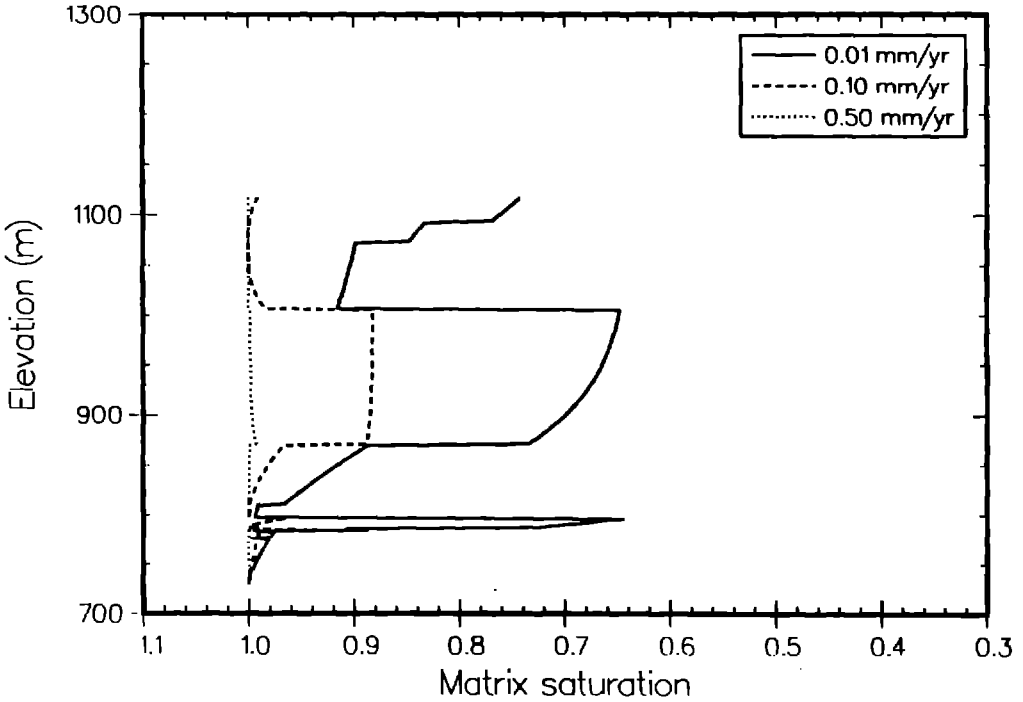

Figure 8. Matrix saturation for hole UE-25a.

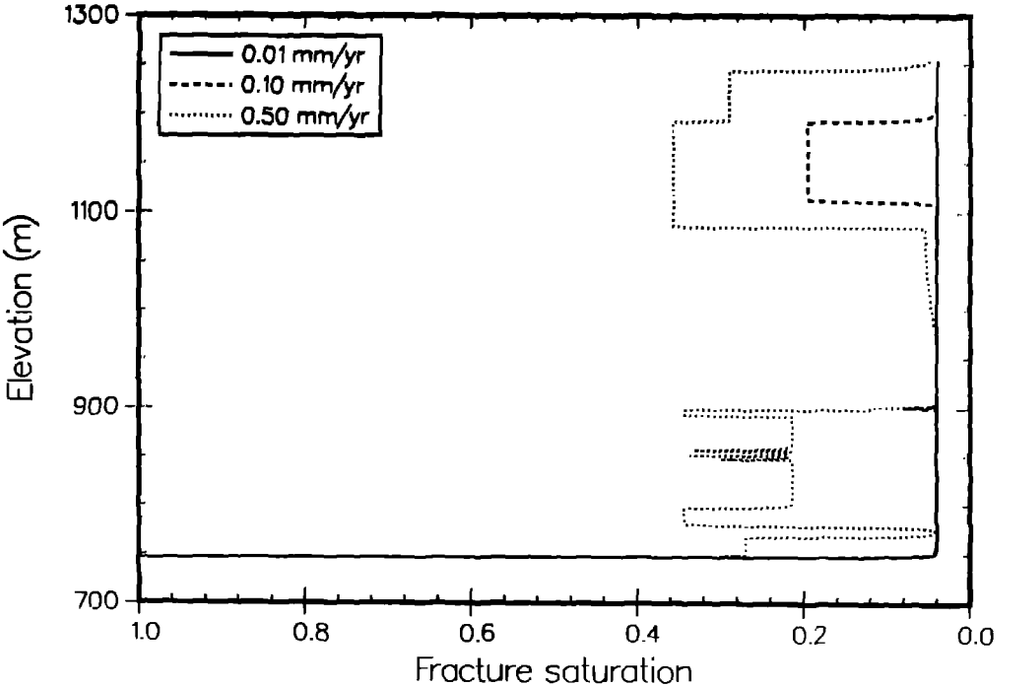

Figure 9. Fracture saturation for hole G-1.

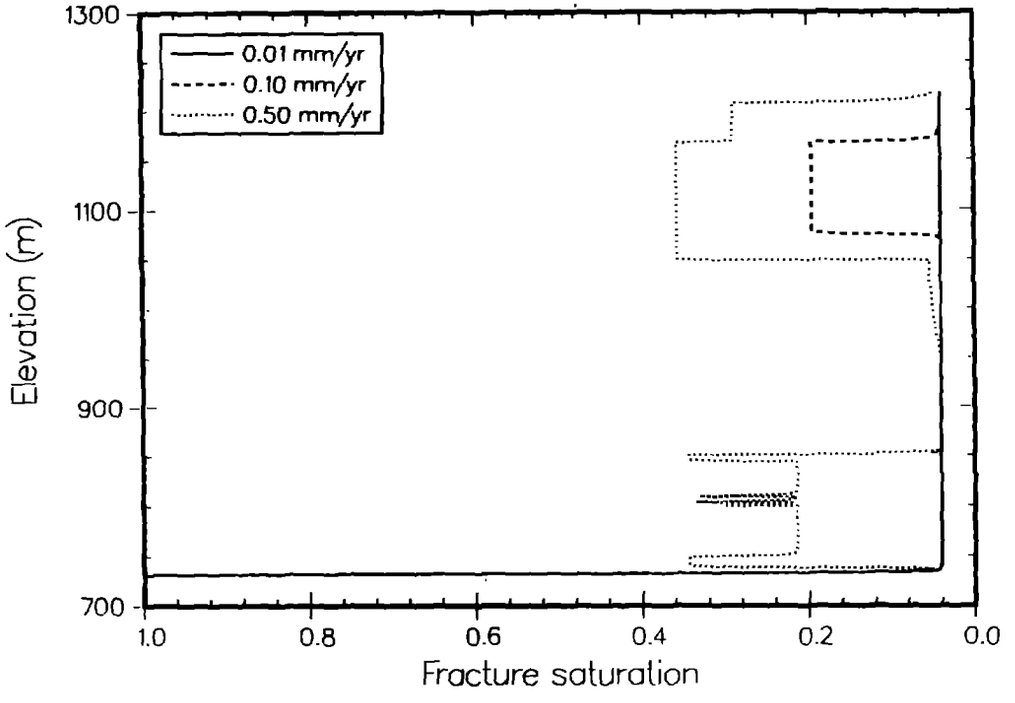

Figure 10. Fracture saturation for hole H-1.

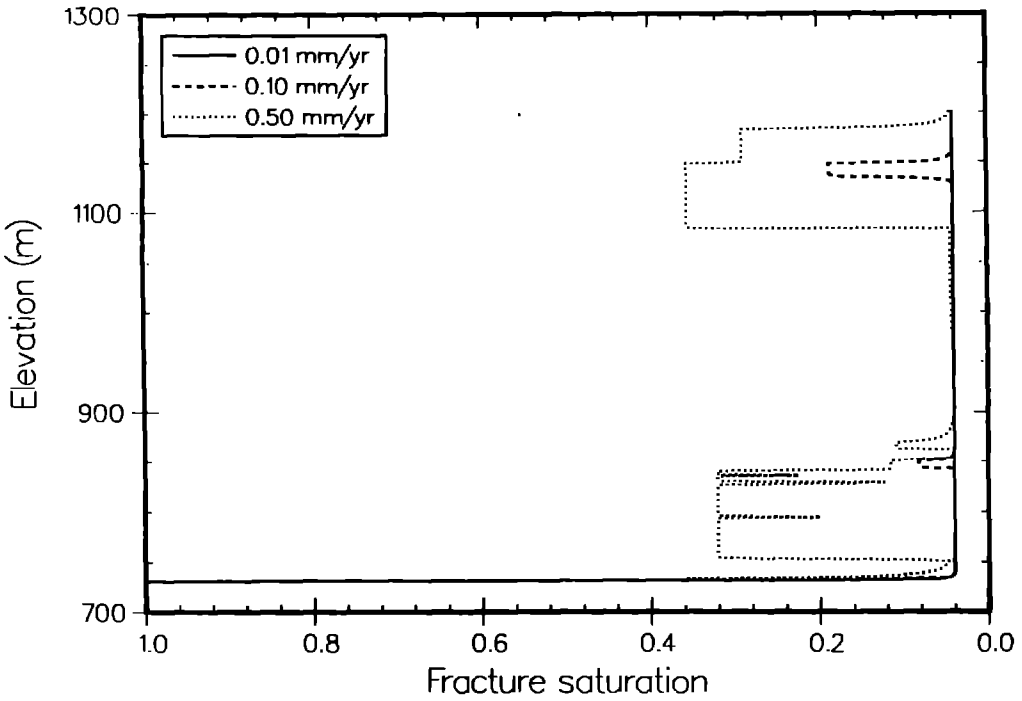

Figure 11. Fracture saturation for hole G-4.

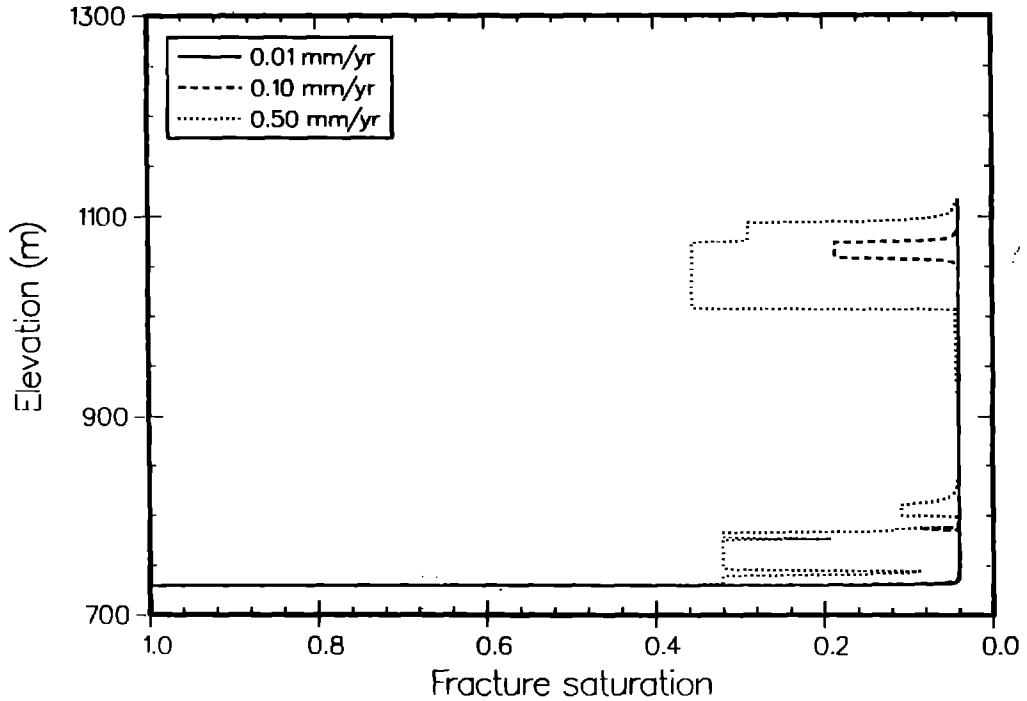

Figure 12. Fracture saturation for hole UE-25a.

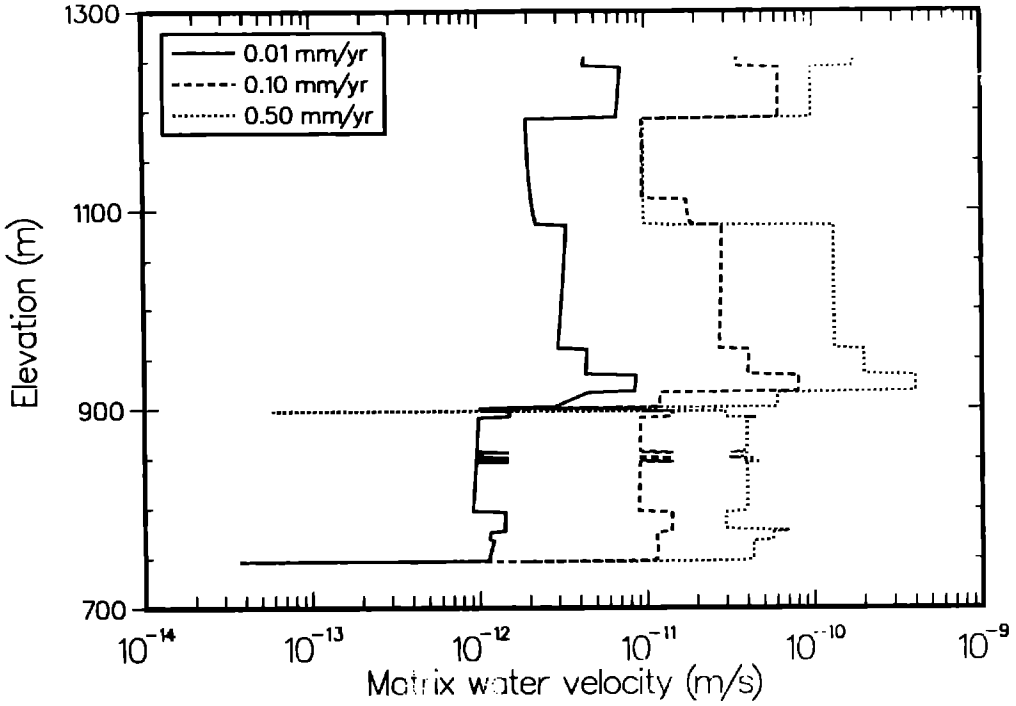

Figure 13. Matrix water velocities for hole G-1.

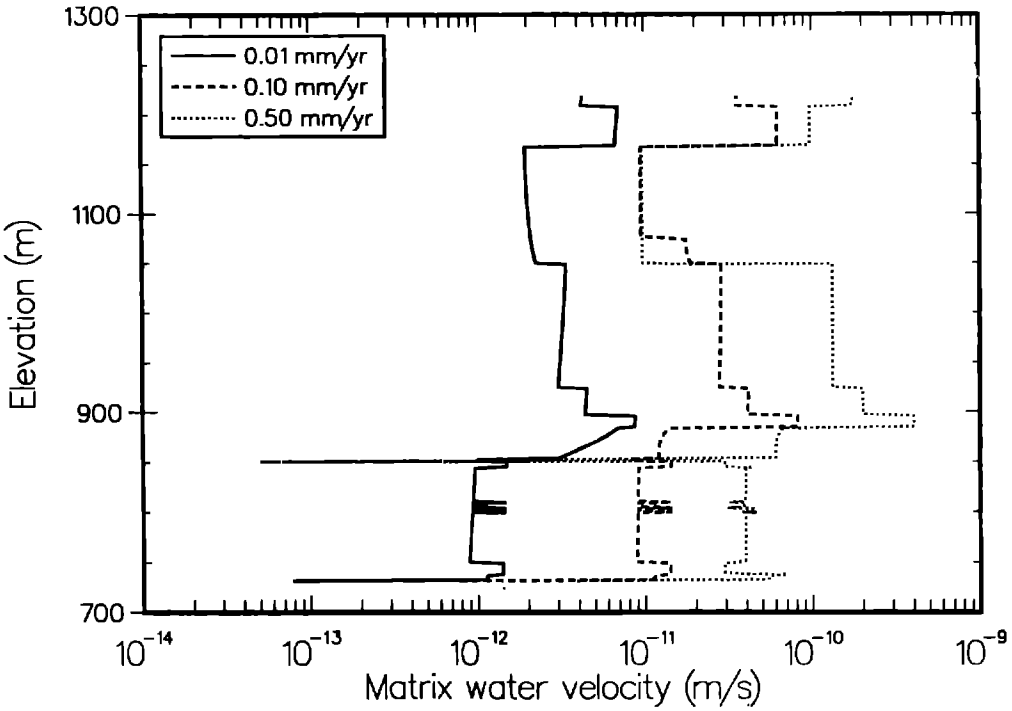

Figure 14. Matrix water velocities for hole H-1.

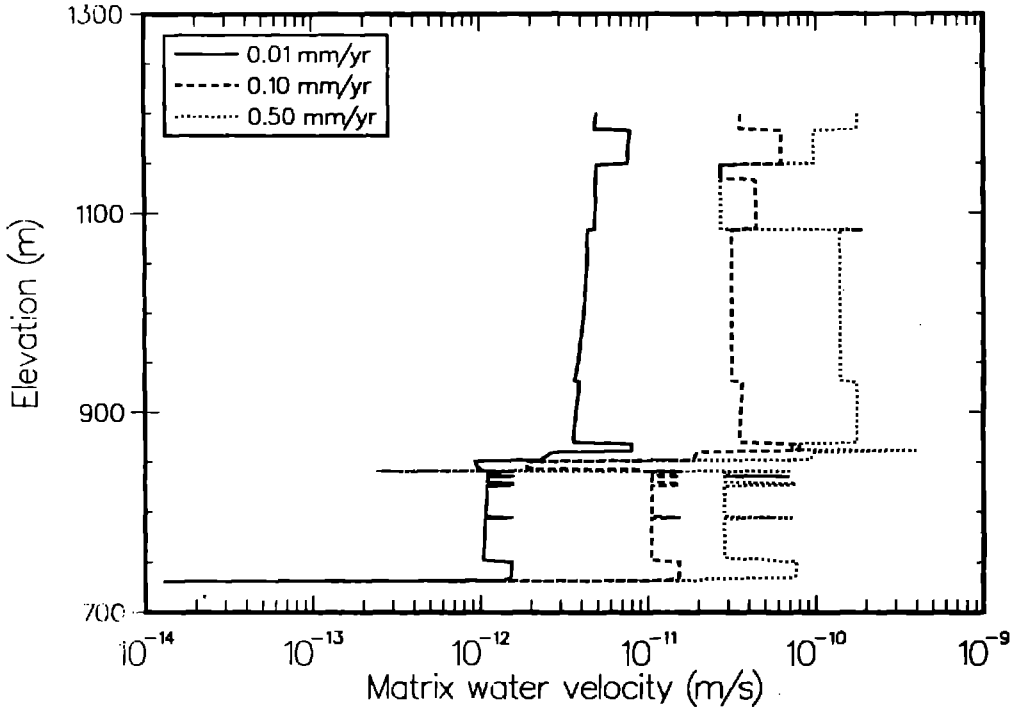

Figure 15. Matrix water velocities for hole G-4.

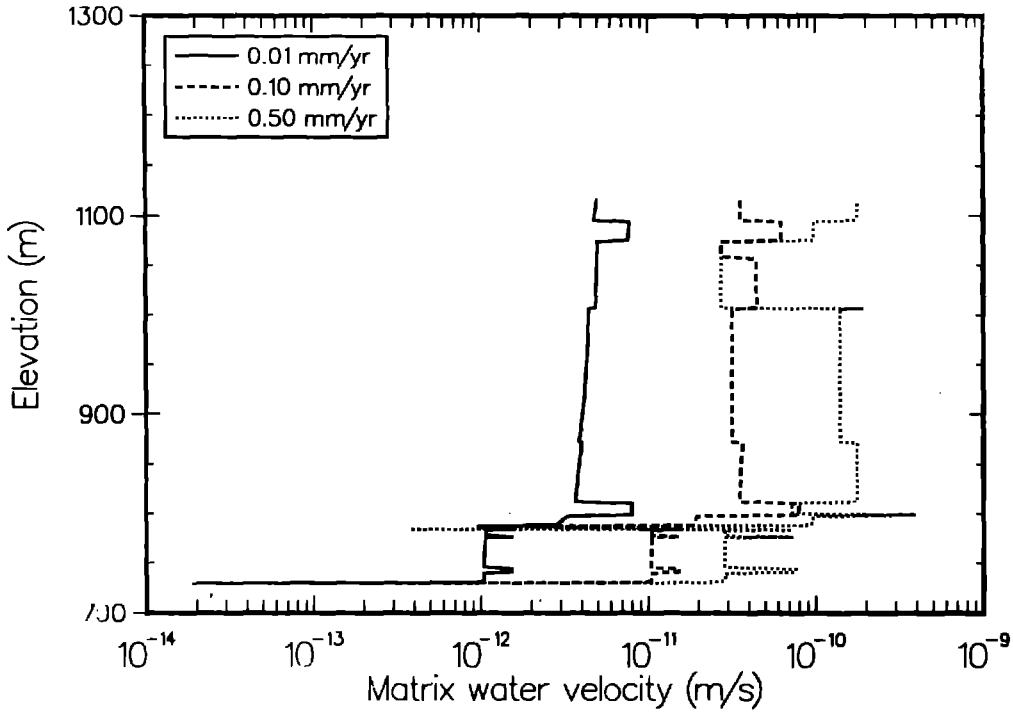

Figure 16. Matrix water velocities for hole UE-25a.

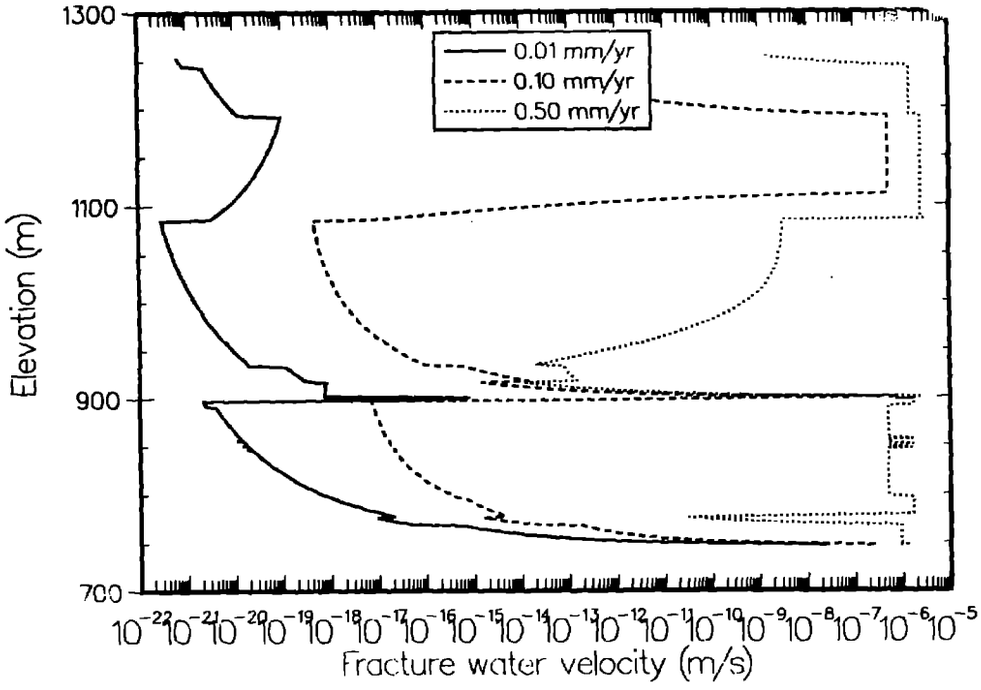

Figure 17. Fracture water velocities for hole G-1 (The very small values are presented for future code comparisons, and are probably not realistic).

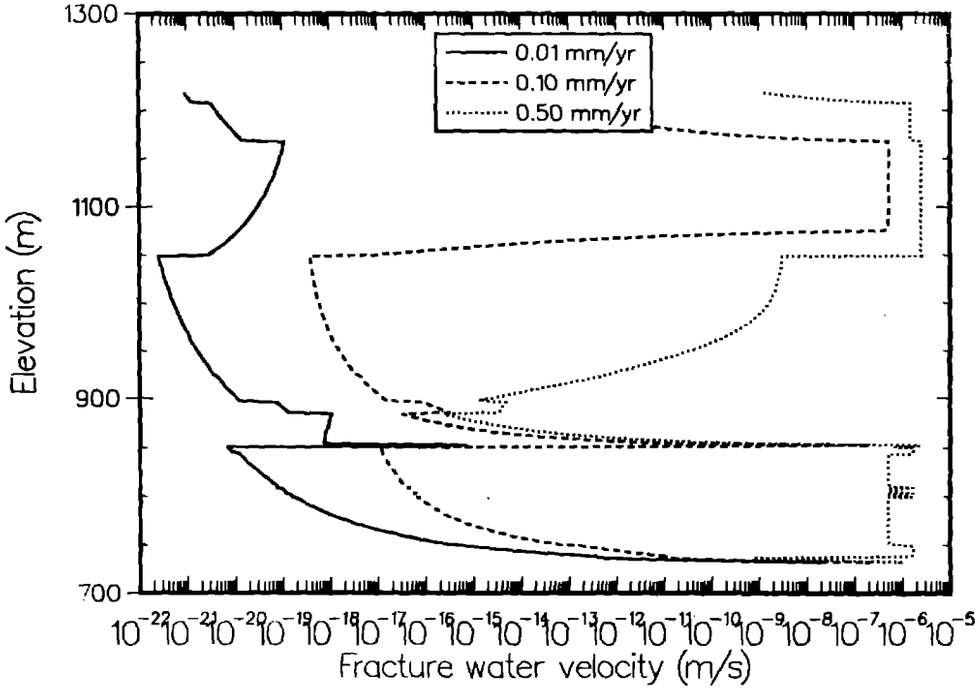

Figure 18. Fracture water velocities for hole H-1 (The very small values are presented for future code comparisons, and are probably not realistic).

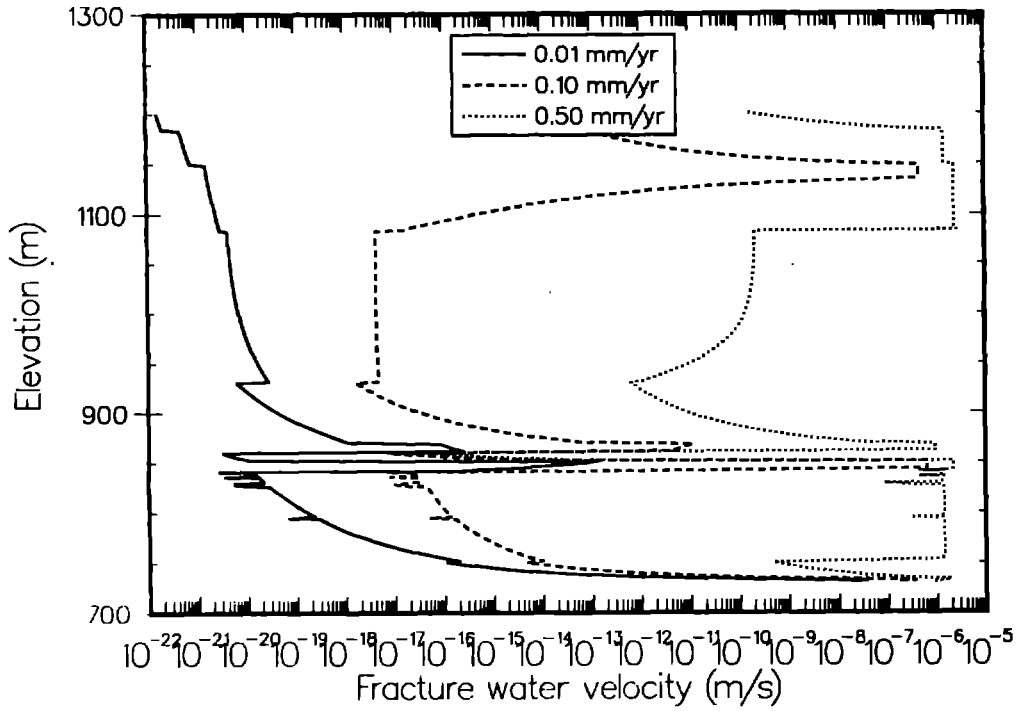

Figure 19. Fracture water velocities for hole G-4 (The very small values are presented for future code comparisons, and are probably not realistic).

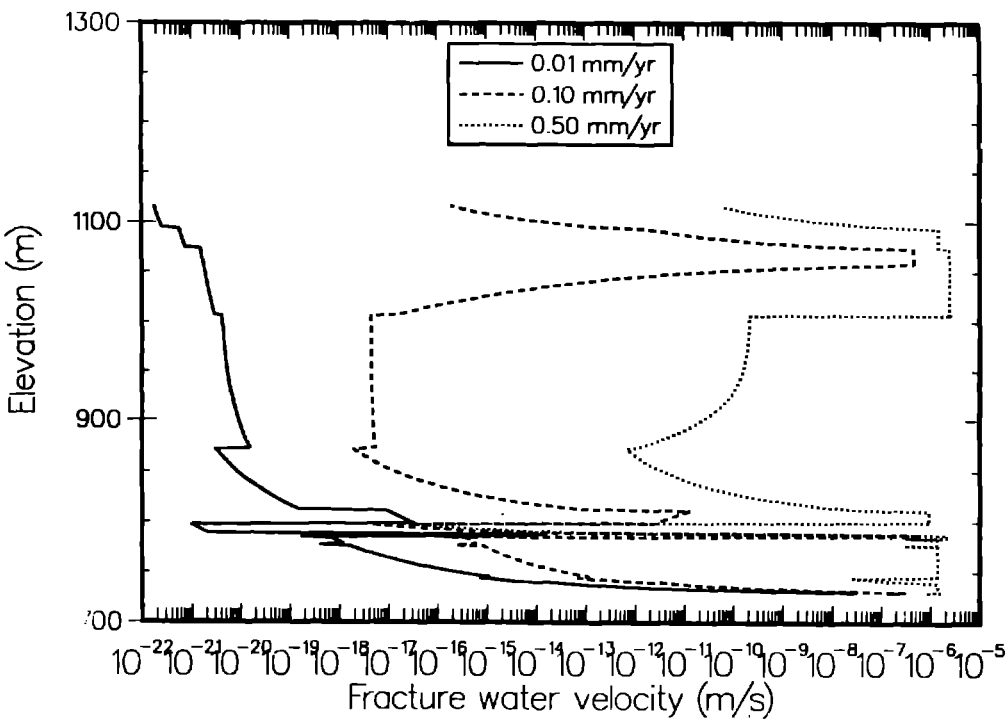

Figure 20. Fracture water velocities for hole UE-25a (The very small values are presented for future code comparisons, and are probably not realistic).

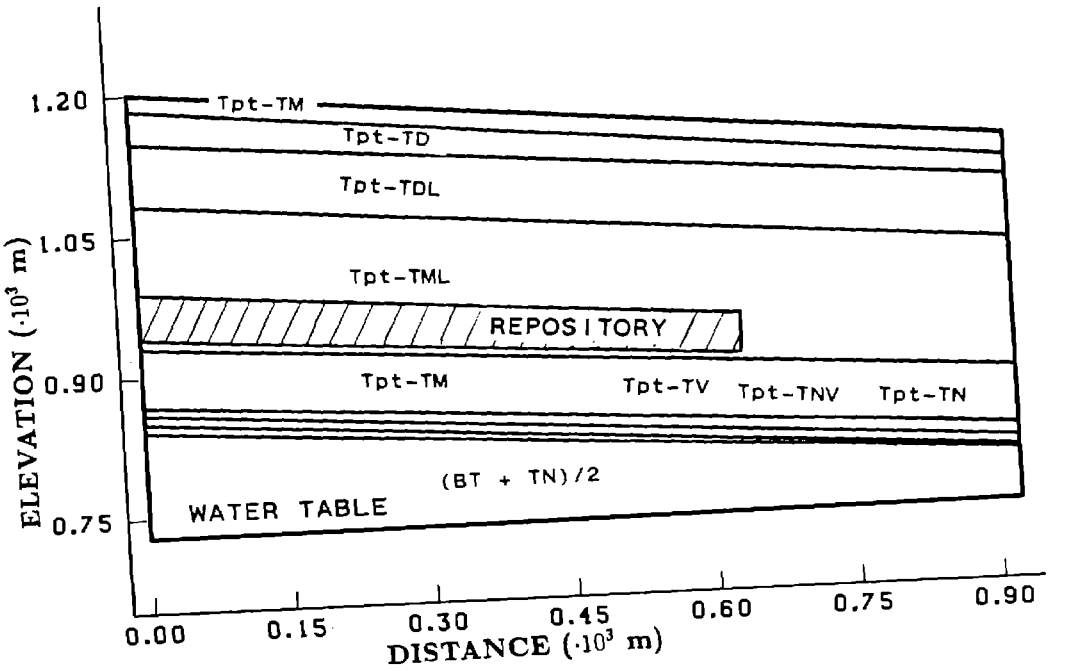

Figure 21. Two-dimensional geometry of material regions. (Drillhole G-4 at the left boundary and UE-25a at the right boundary)

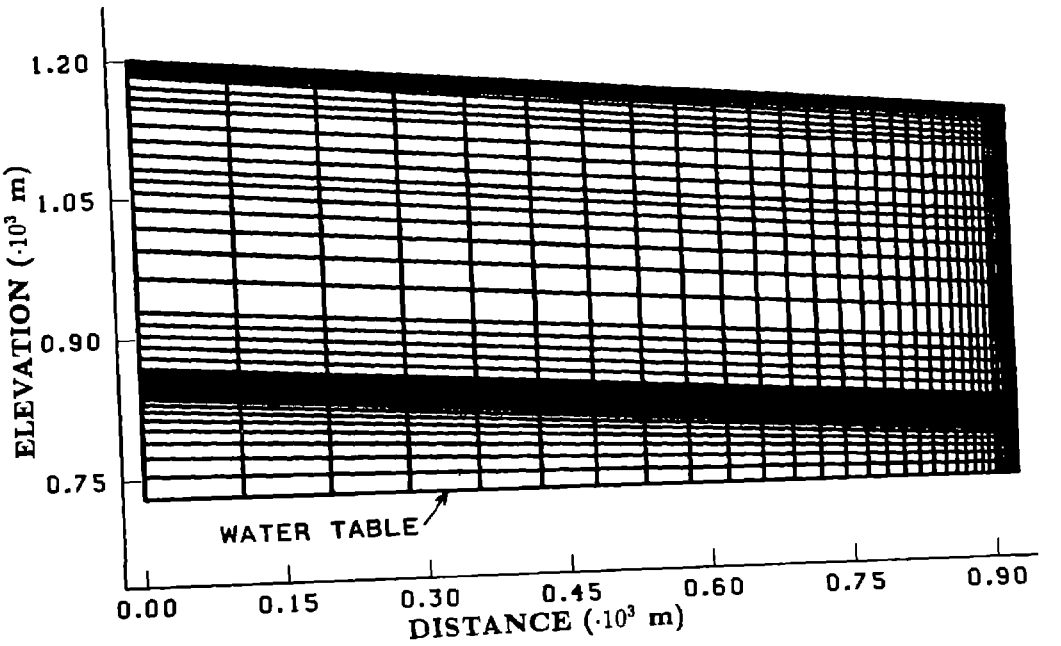

Figure 22. Two-dimensional finite element geometry, 1260 elements.

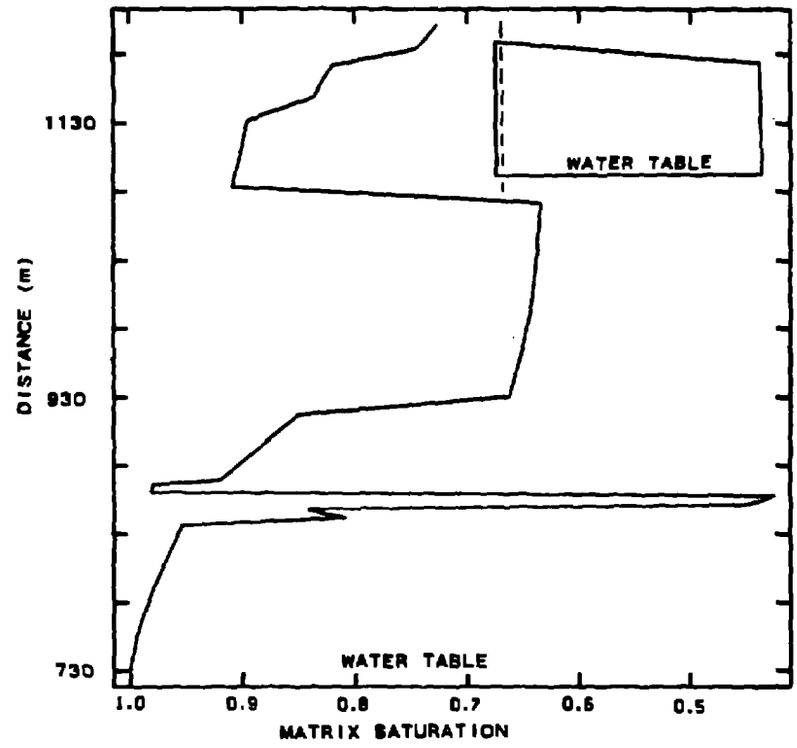

Figure 23. Matrix saturation profile for two-dimensional geometry, 0.01 mm/yr infiltration, Hole G-4.

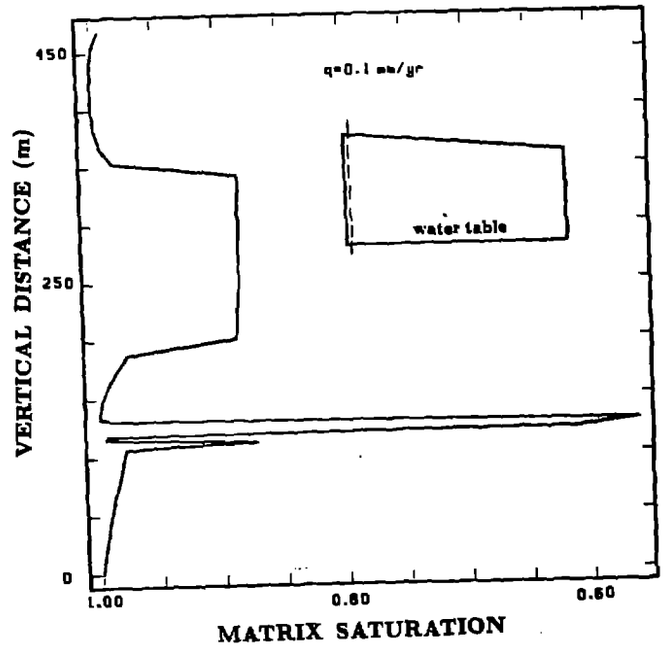

Figure 24. Matrix saturation profile for two-dimensional geometry, 0.1 mm/yr infiltration, Hole G-4.

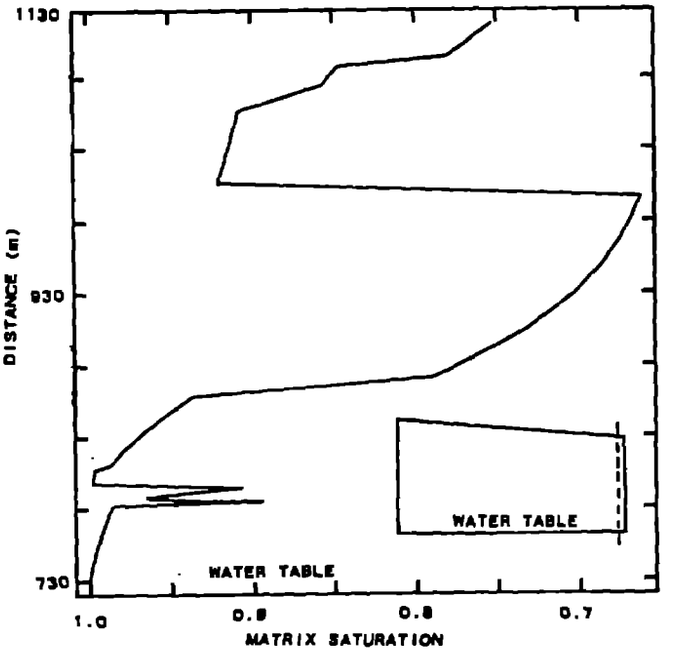

Figure 25. Matrix saturation profile for two-dimensional geometry, 0.01 mm/yr infiltration, Hole UE-25a.

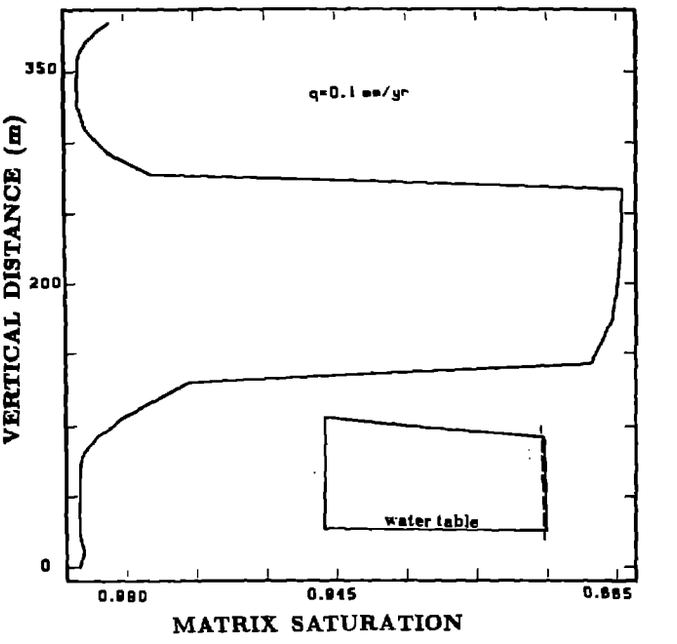

Figure 26. Matrix saturation profile for two-dimensional geometry, 0.1 mm/yr infiltration, Hole UE-25a.

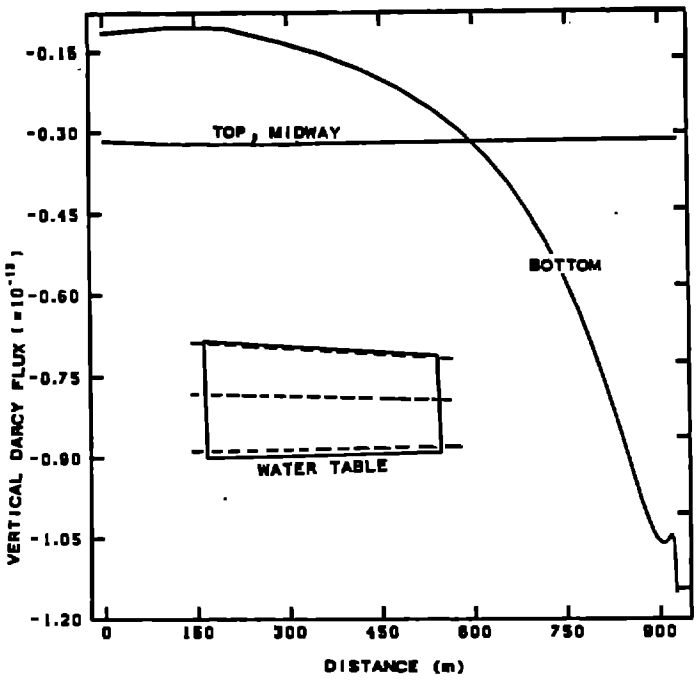

Figure 27. Total vertical water flux profile near top and bottom of two-dimensional region, 0.01 mm/yr infiltration.

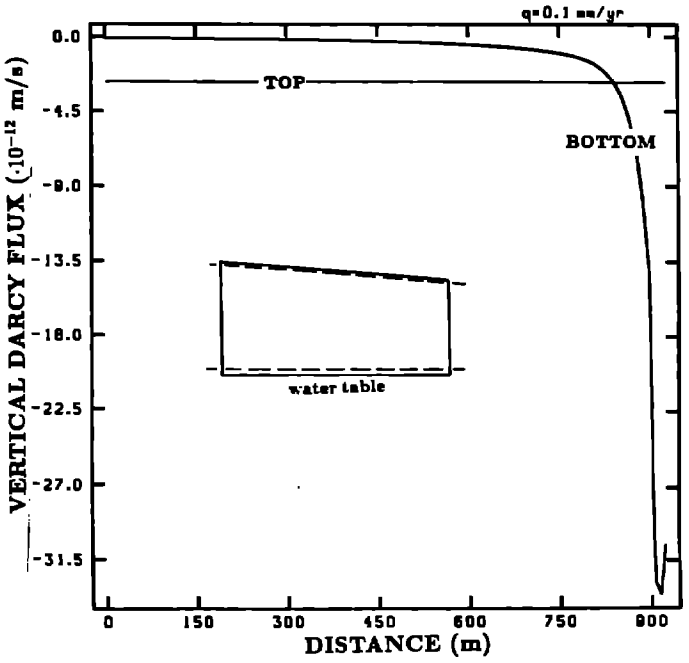

Figure 28. Total vertical water flux profile near top and bottom of two-dimensional region, 0.1 mm/yr infiltration.

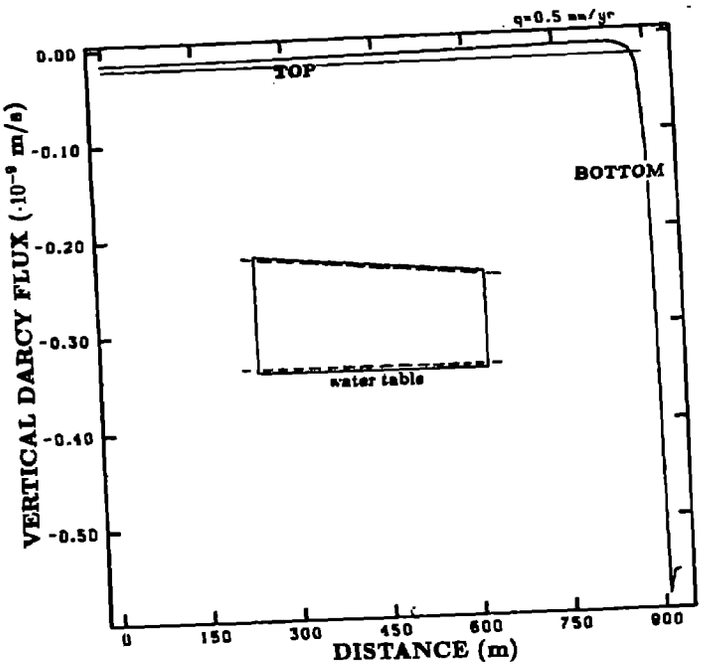

Figure 29. Total vertical water flux profile near top and bottom of two-dimensional region, 0.5 mm/yr infiltration.

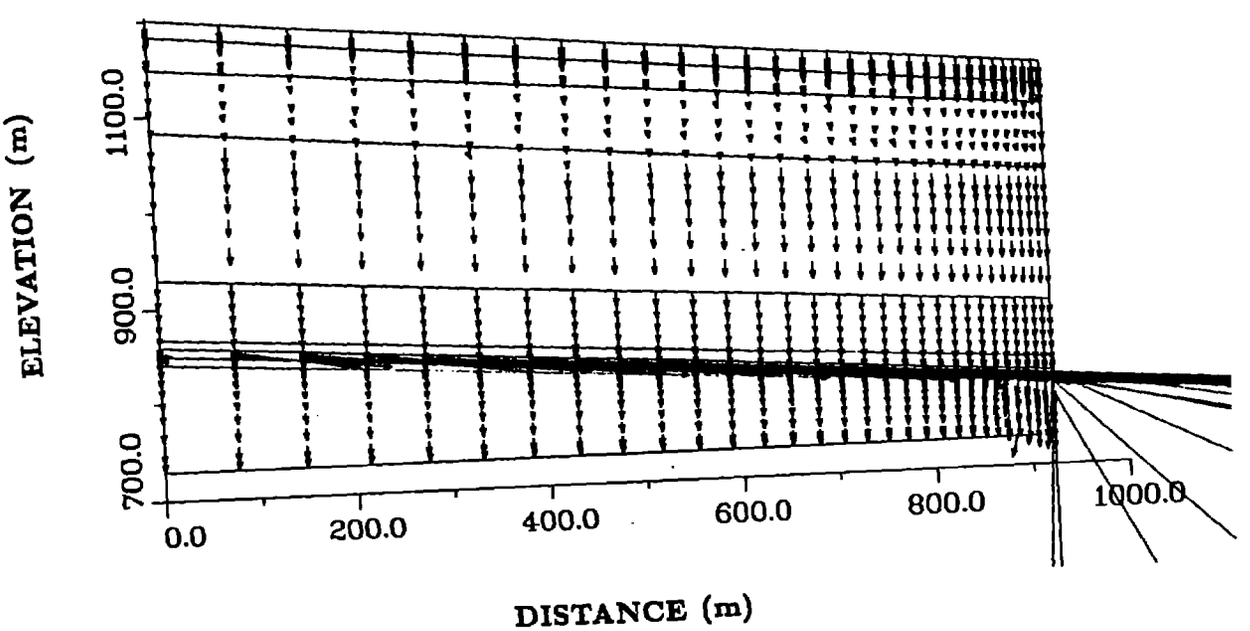

Figure 30. Darcy matrix velocity vectors, 0.5 mm/yr infiltration.

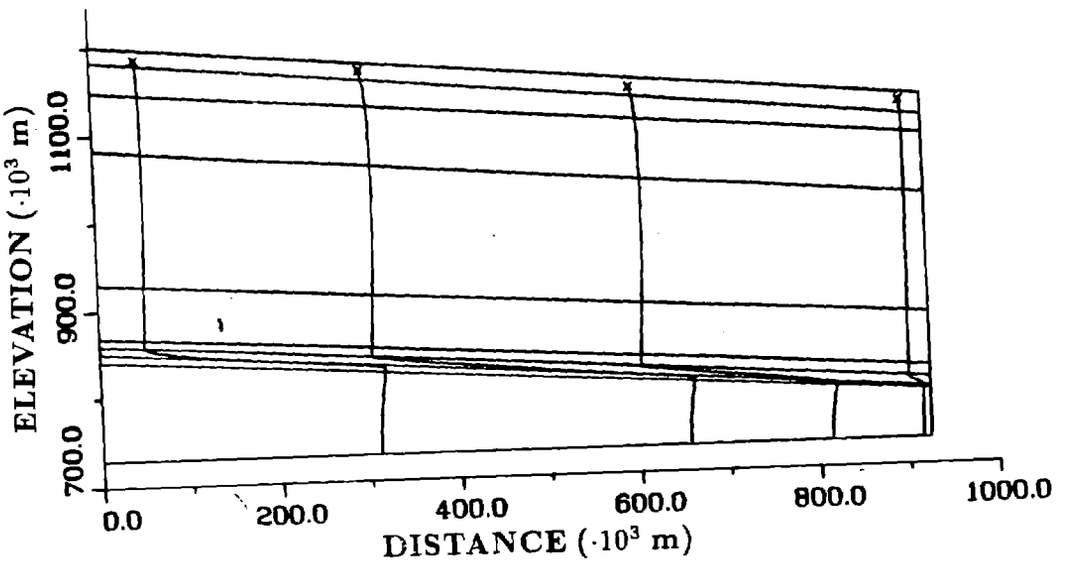

Figure 31. Particle pathlines, 0.01 mm/yr infiltration.

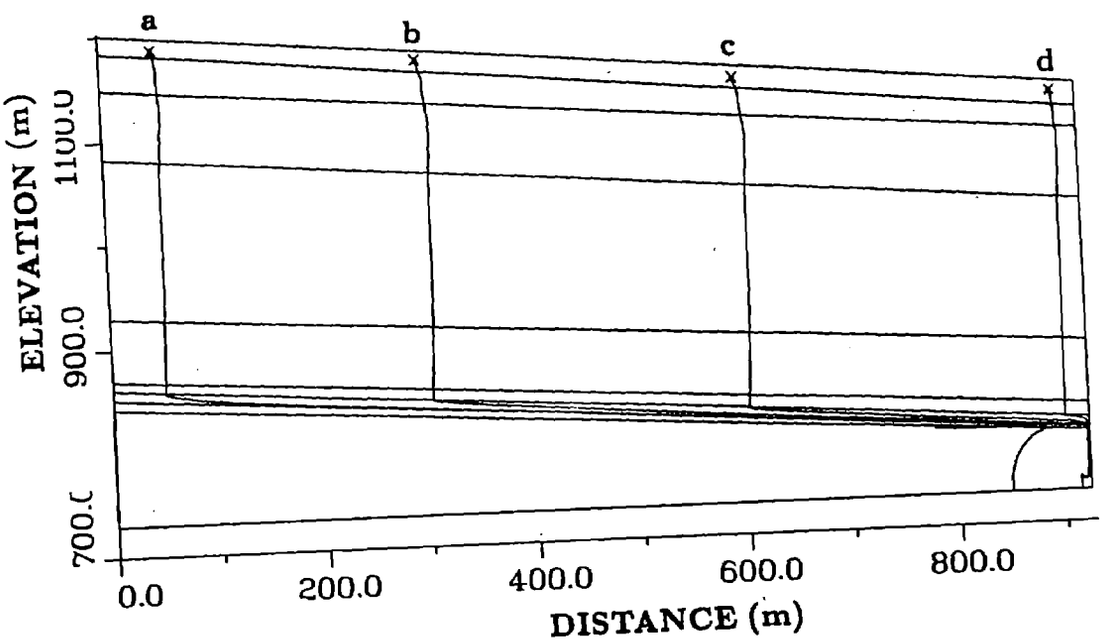

Figure 32. Particle pathlines, 0.1 mm/yr infiltration.

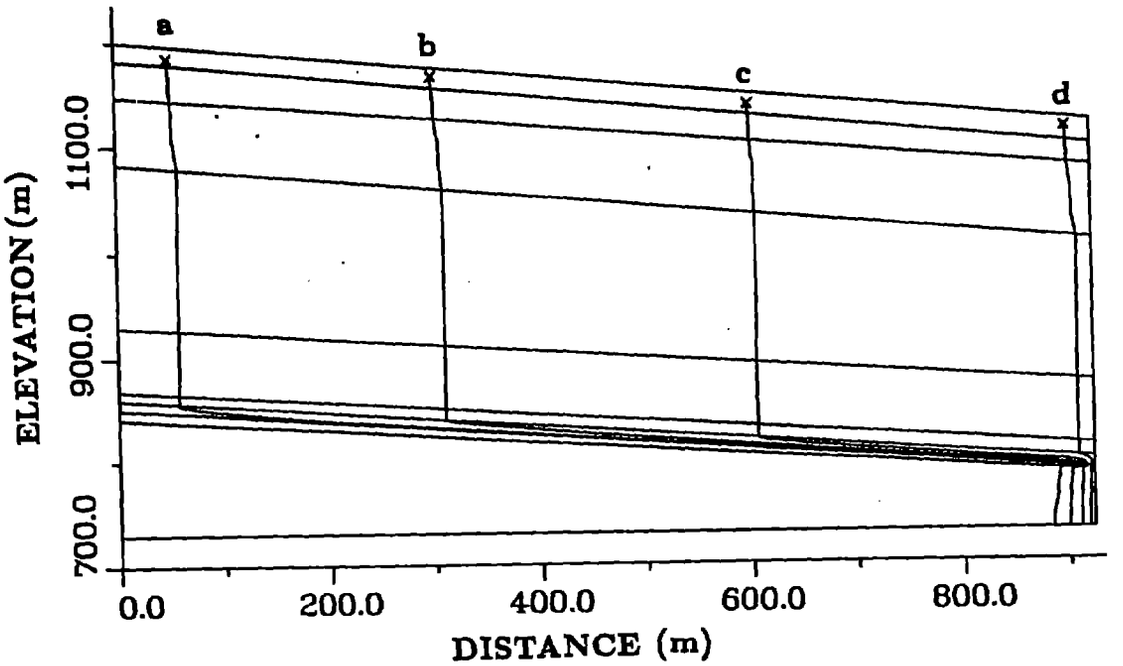

Figure 33. Particle pathlines, 0.5 mm/yr infiltration.

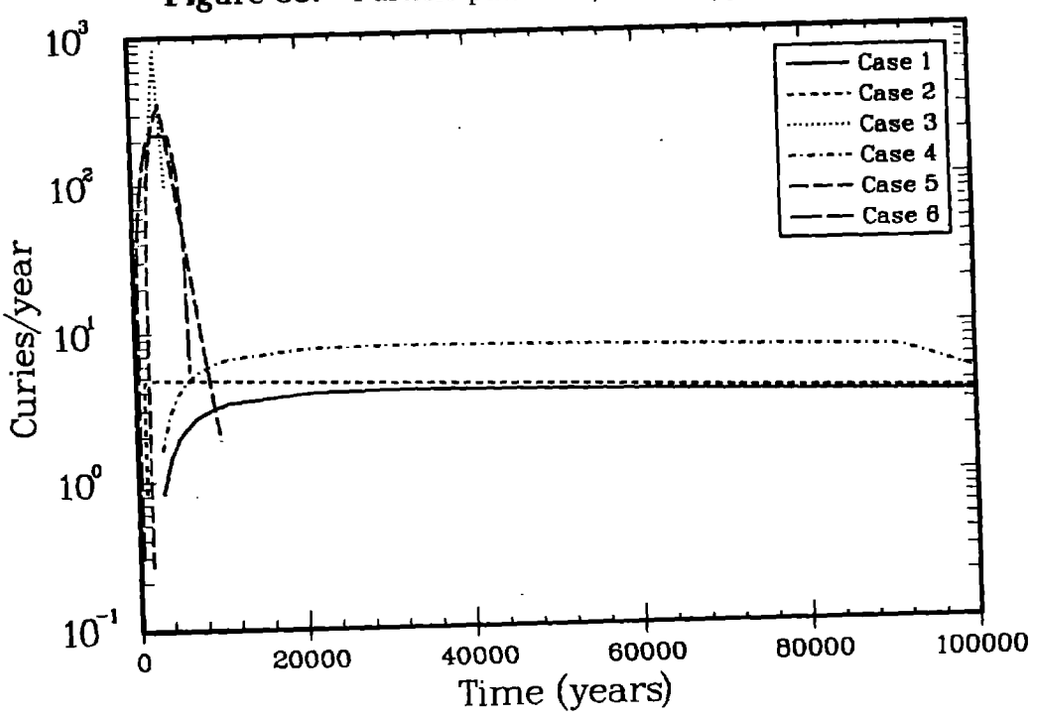

Figure 34. I-129 source terms for Cases 1 through 6.

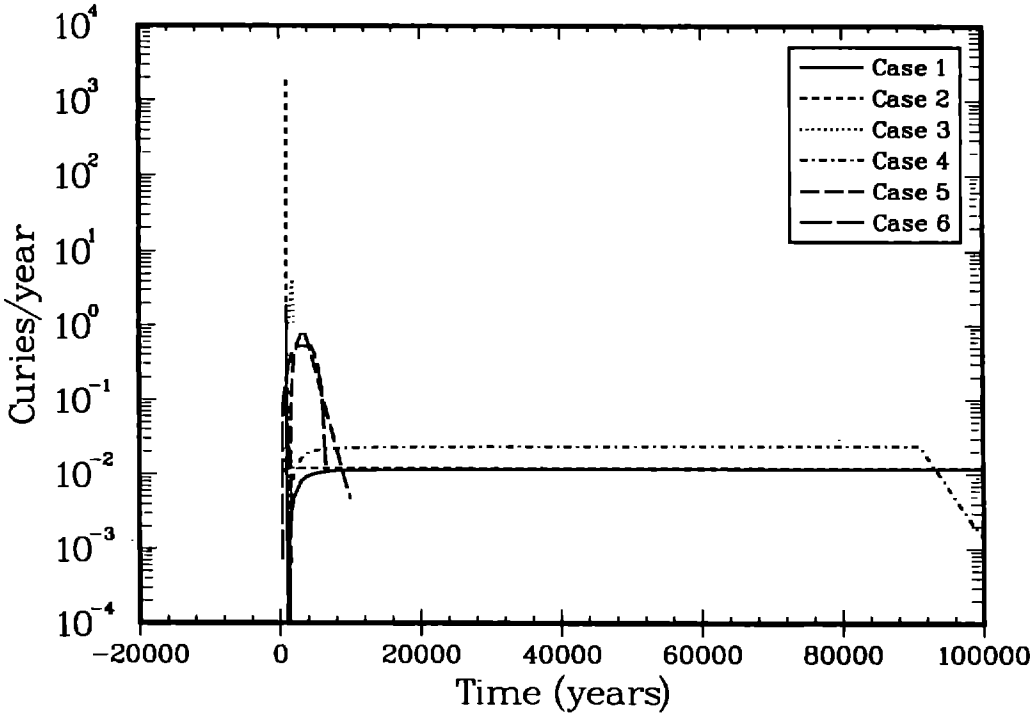

Figure 35. Tc-99 source terms for Cases 1 through 6.

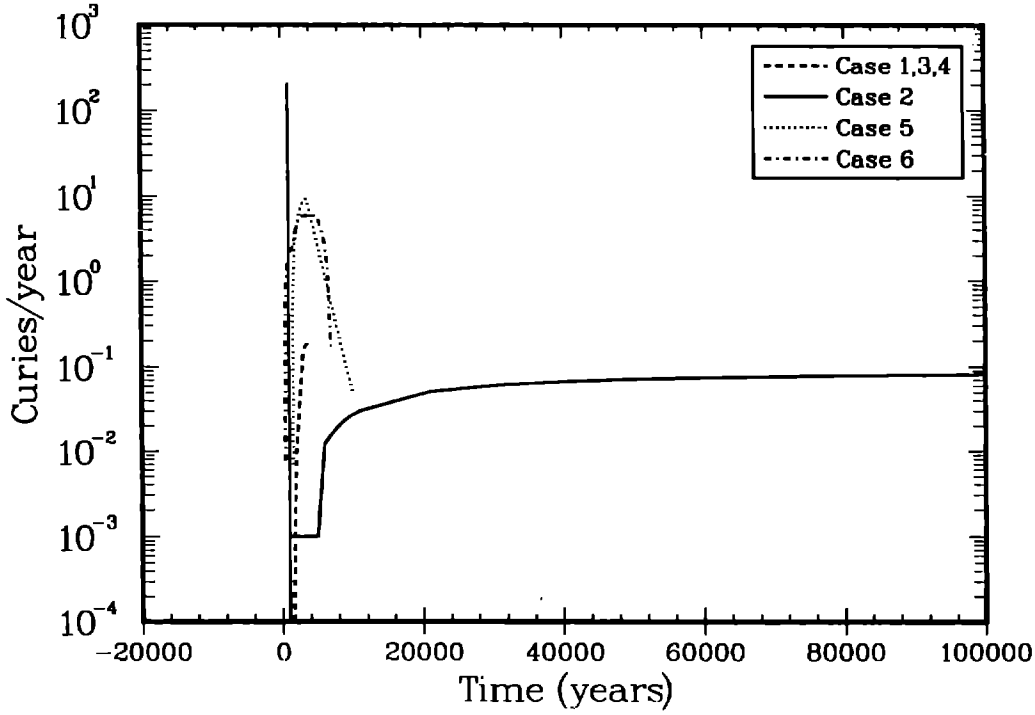

Figure 36. Cs-135 source terms for Cases 1 through 6.

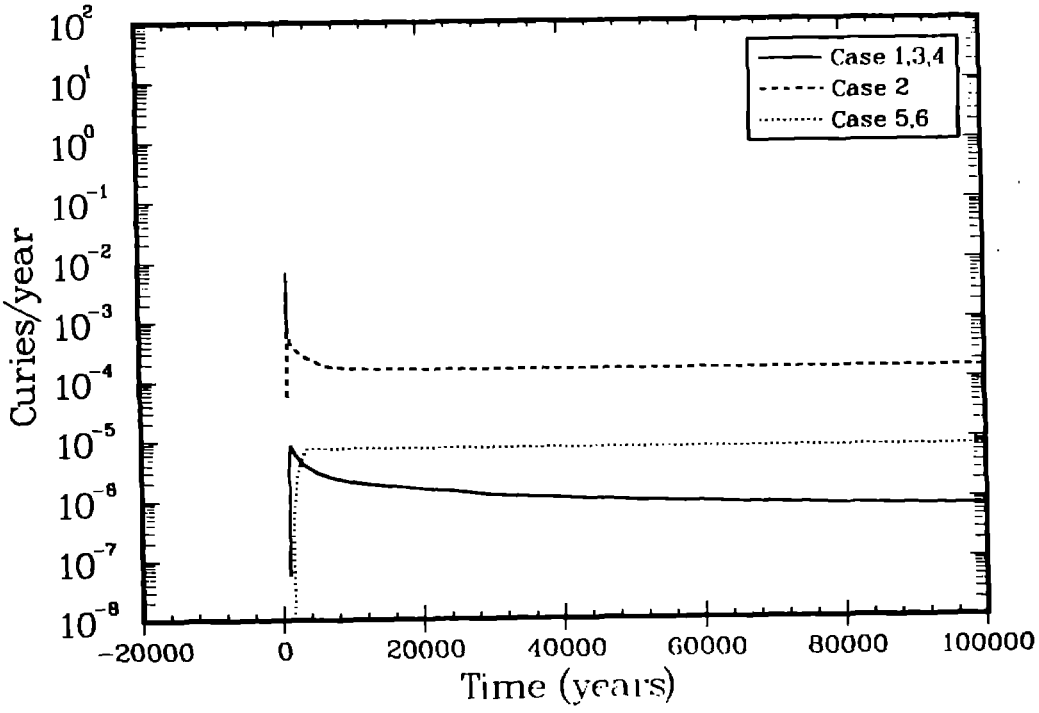

Figure 37. Np-237 source terms for Cases 1 through 6.

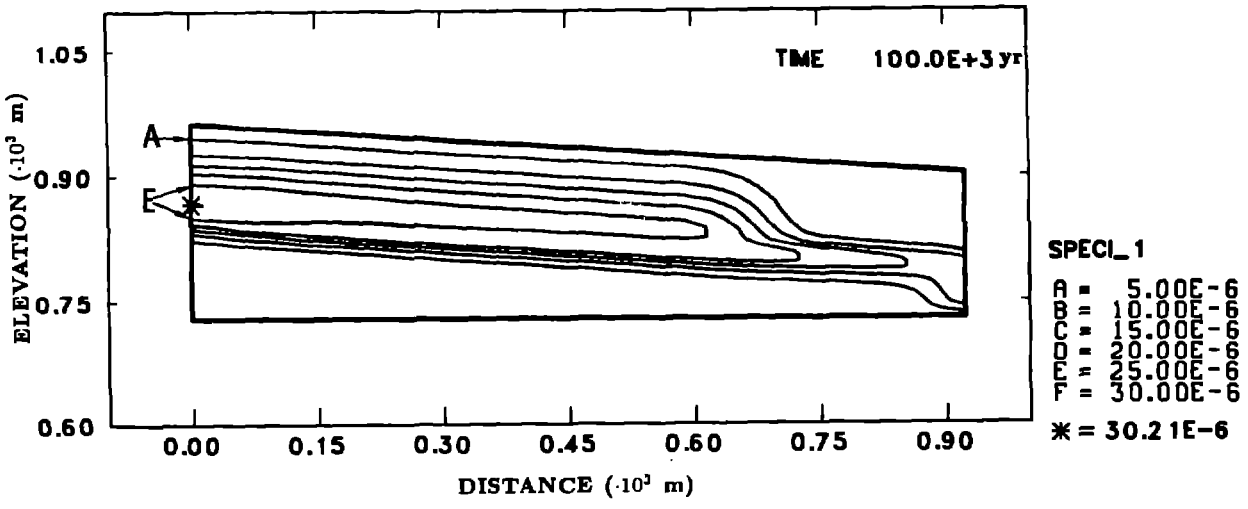

Figure 38. Concentration (curie/m^3) of I-129 for 0.1 mm/yr infiltration and Case 3 release at 100,000 yr.

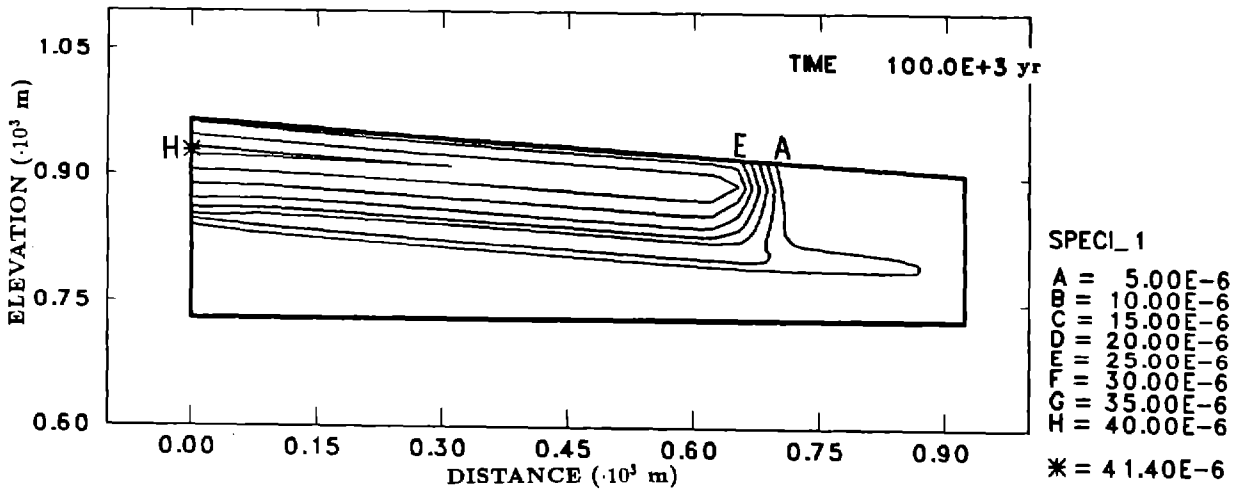

Figure 39. Concentration (curie/m^3) of I-129 for 0.1 mm/yr infiltration and Case 4 release at 100,000 yr.

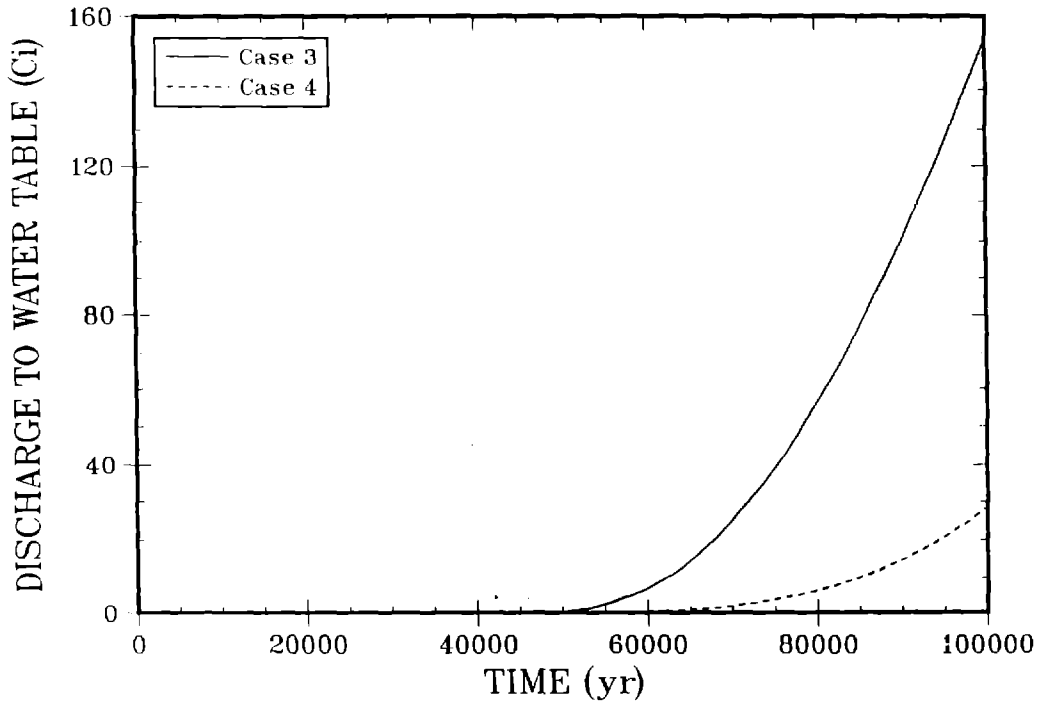

Figure 40. Cumulative discharge of I-129 to the water table for 0.1 mm/yr infiltration and Case 3 and 4 release models.

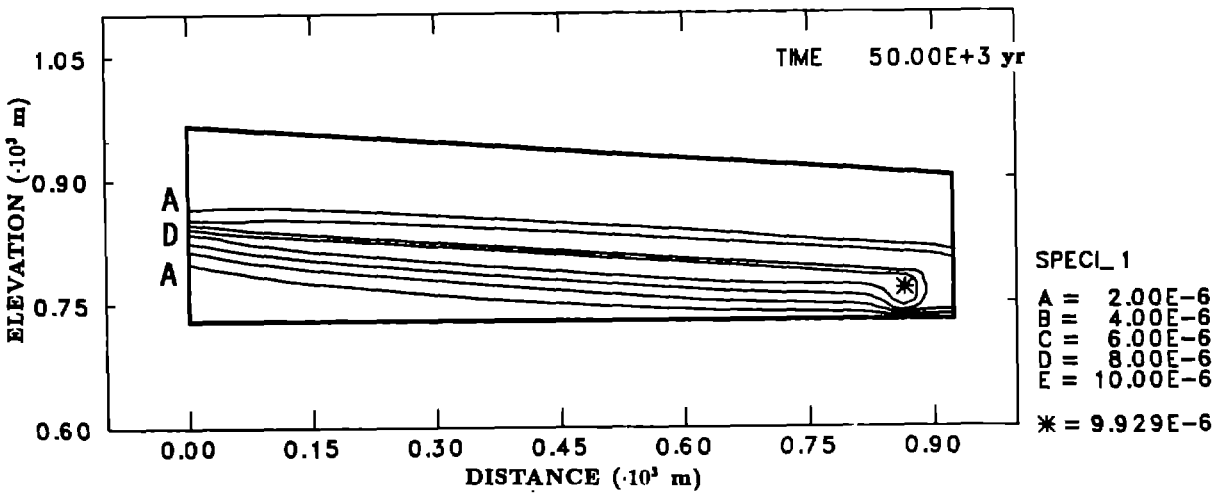

Figure 41. Concentration ($curie/m^3$) of I-129 for 0.5 mm/yr infiltration and Case 3 release at 50,000 yr

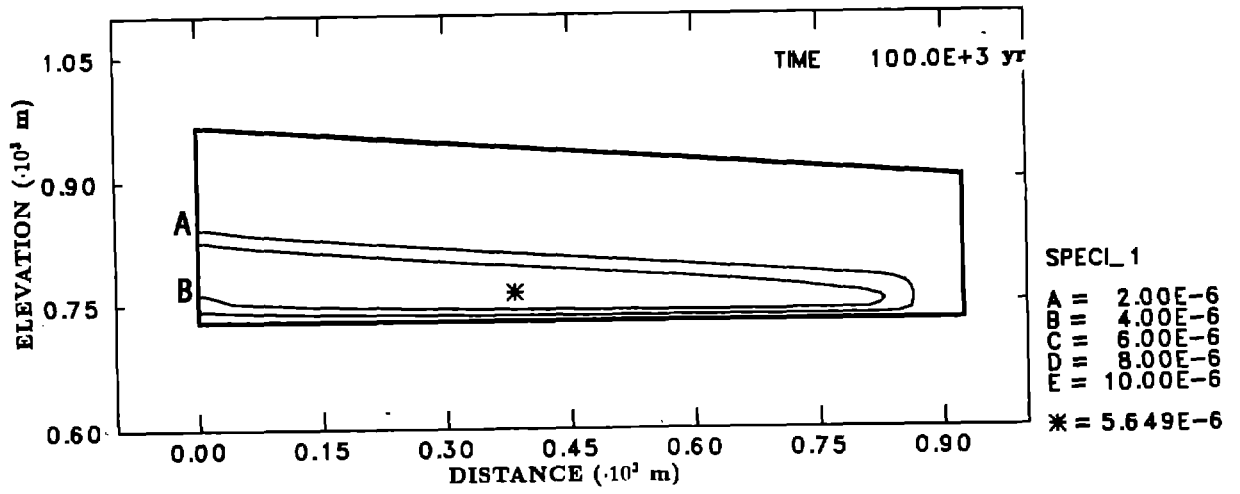

Figure 42. Concentration ($curie/m^3$) of I-129 for 0.5 mm/yr infiltration and Case 3 release at 100,000 yr.

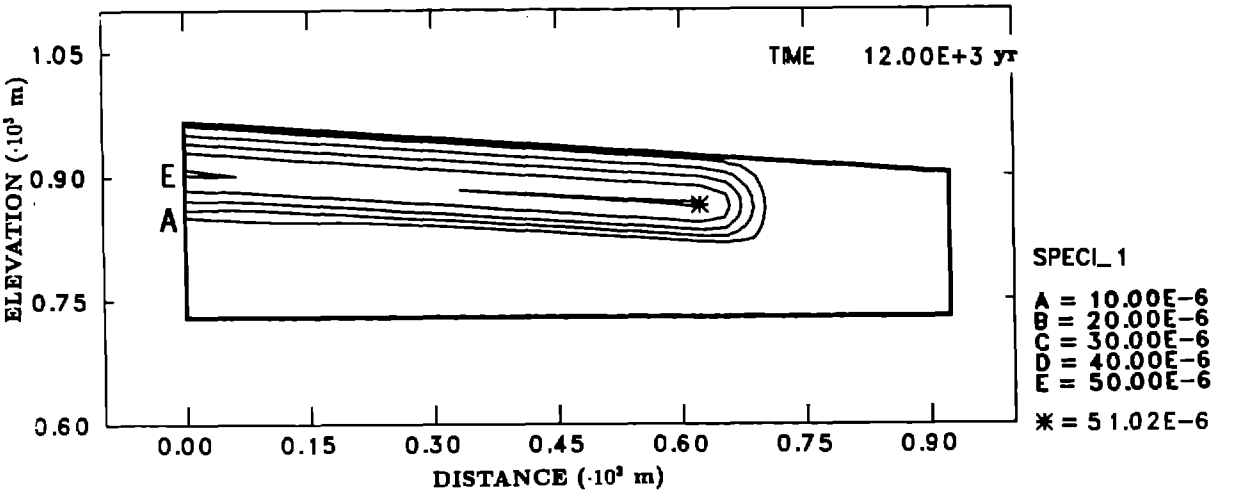

Figure 43. Concentration ($curie/m^3$) of I-129 for 0.5 mm/yr infiltration and Case 3 release at 12,000 yr

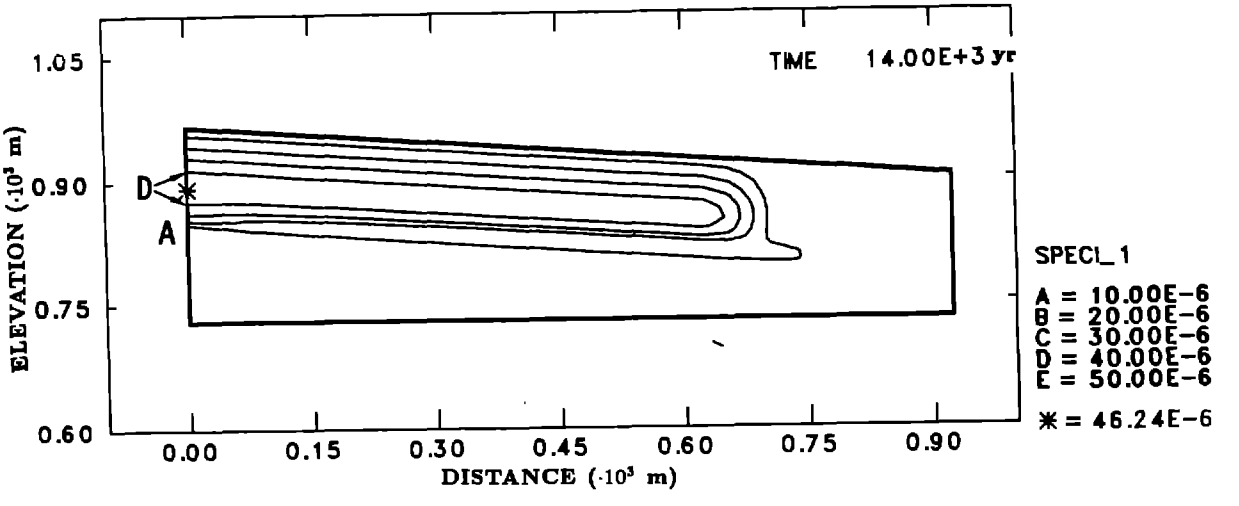

Figure 44. Concentration ($curie/m^3$) of I-129 for 0.5 mm/yr infiltration and Case 3 release at 14,000 yr.

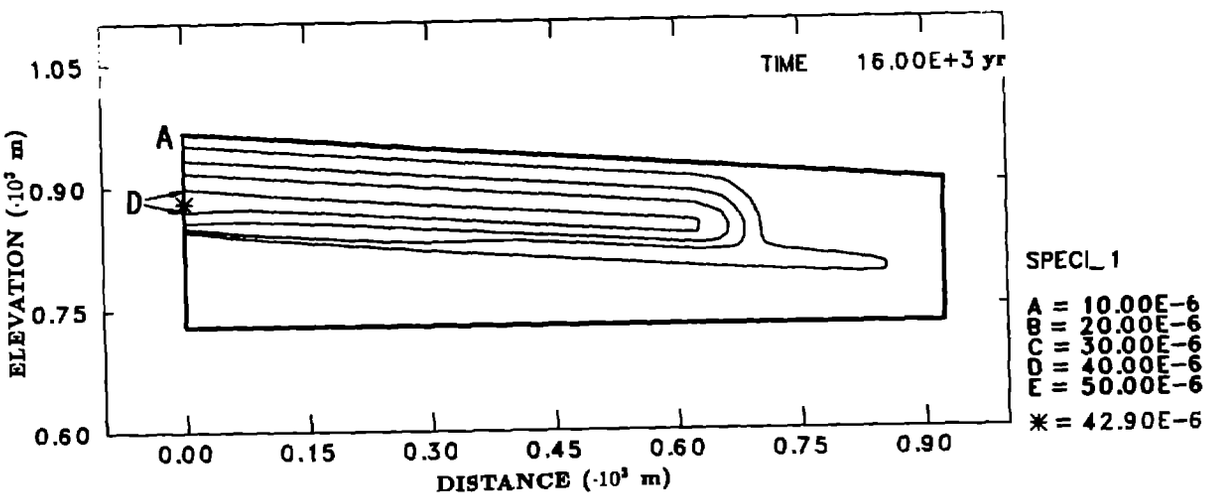

Figure 45. Concentration ($curie/m^3$) of I-129 for 0.5 mm/yr infiltration and Case 3 release at 16,000 yr.

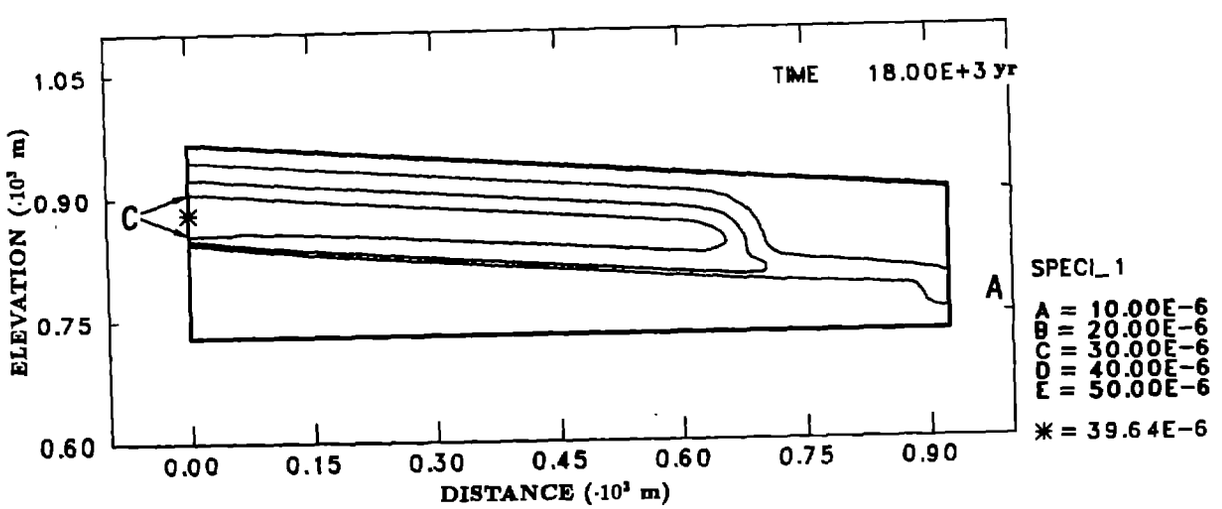

Figure 46. Concentration ($curie/m^3$) of I-129 for 0.5 mm/yr infiltration and Case 3 release at 18,000 yr.

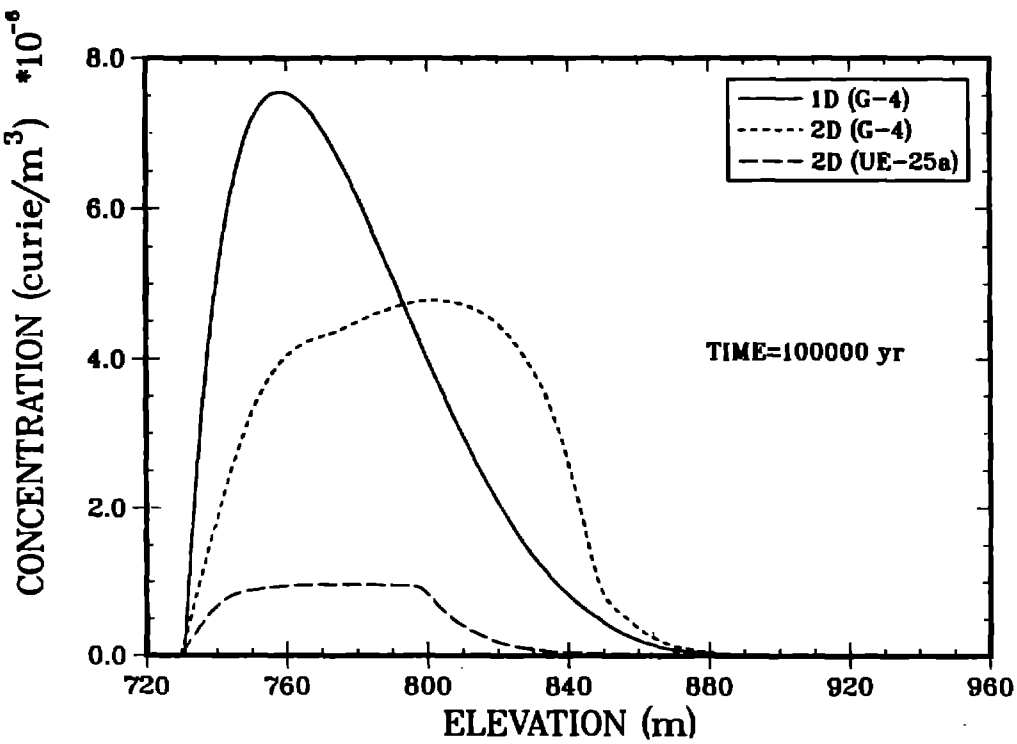

Figure 47. Concentration ($curie/m^3$) of I-129 at 100,000 yr along Holes G-4 and UE-25a for 0.5 mm/yr infiltration and Case 3 release.

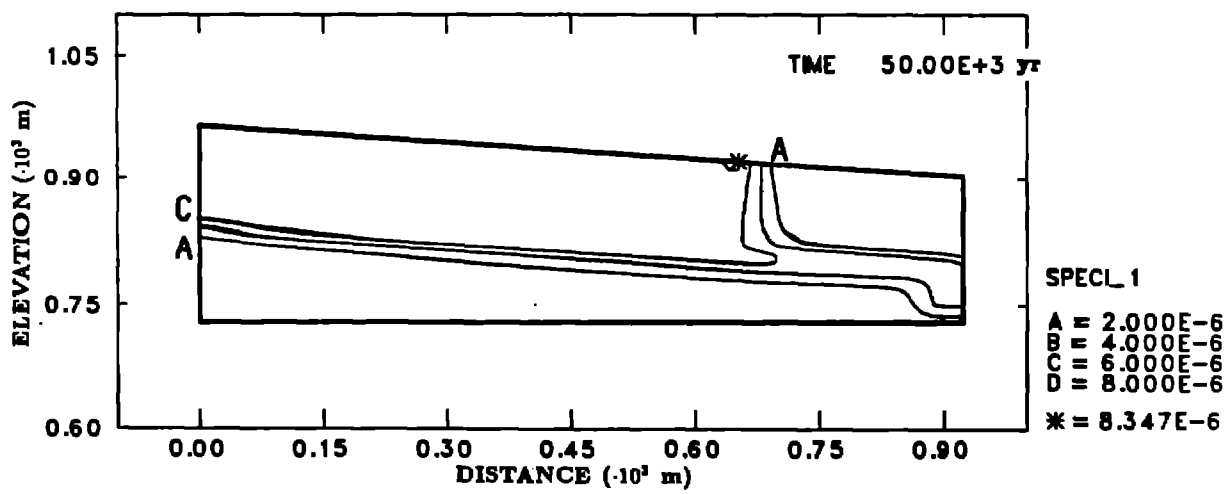

Figure 48. Concentration ($curie/m^3$) of I-129 at 50,000 yr for 0.5 mm/yr infiltration and Case 4 release.

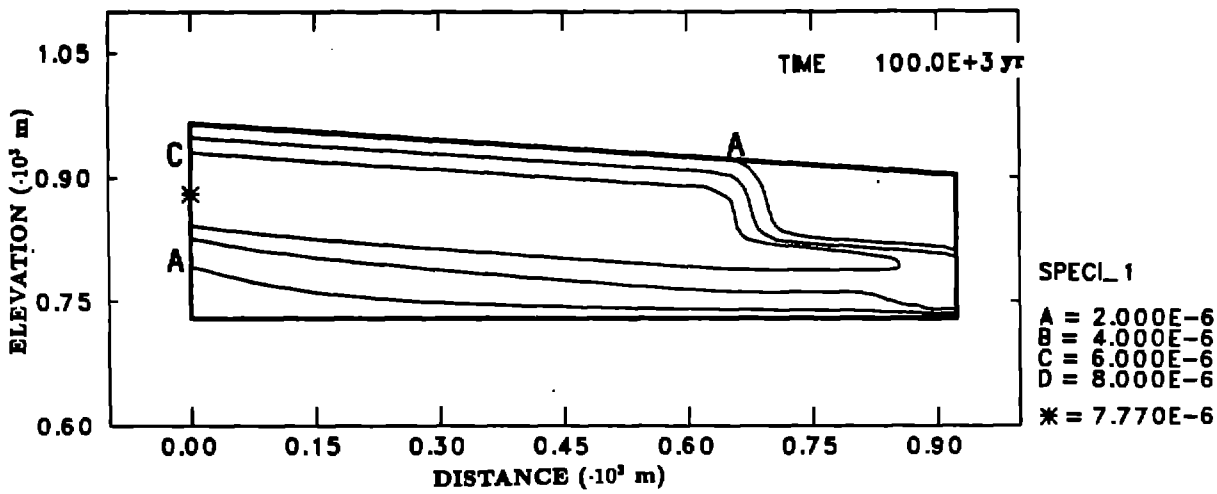

Figure 49. Concentration($curie/m^3$) of I-129 at 100,000 yr for 0.5 mm/yr infiltration and Case 4 release.

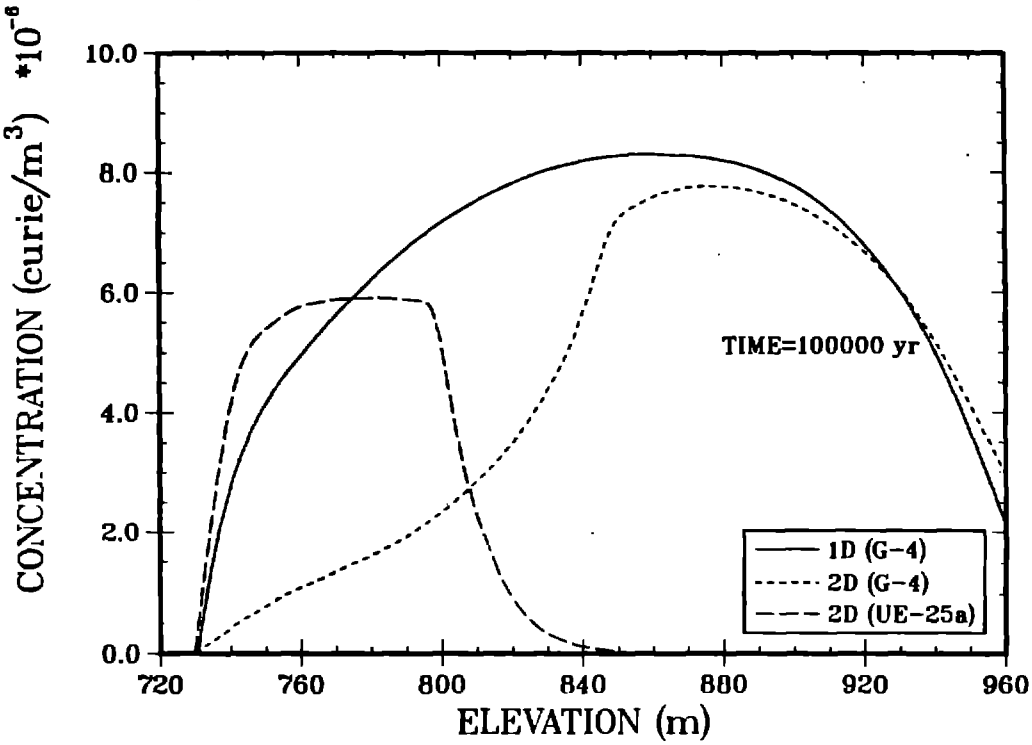

Figure 50. Concentration of I-129 at 100,000 yr along holes G-4 and UE-25a for .5 mm/yr infiltration and Case 4 release.

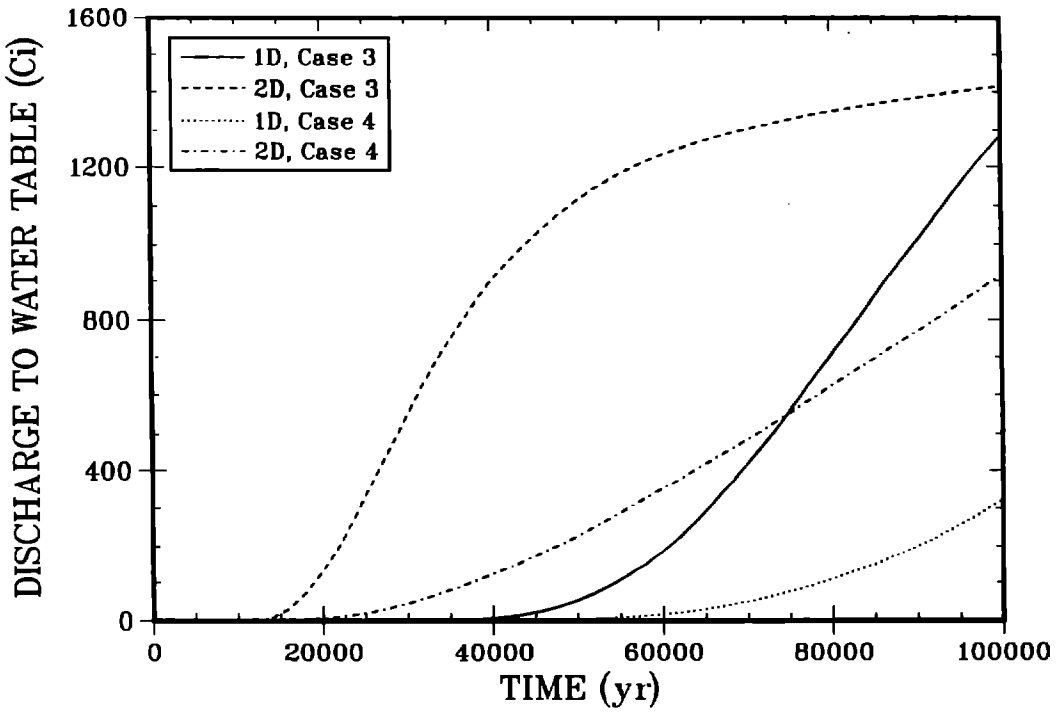

Figure 51. Cumulative dicharge of I-129 to the water table for 0.5 mm/yr infiltration and Case 3 and 4 release models, 100,000 yr.

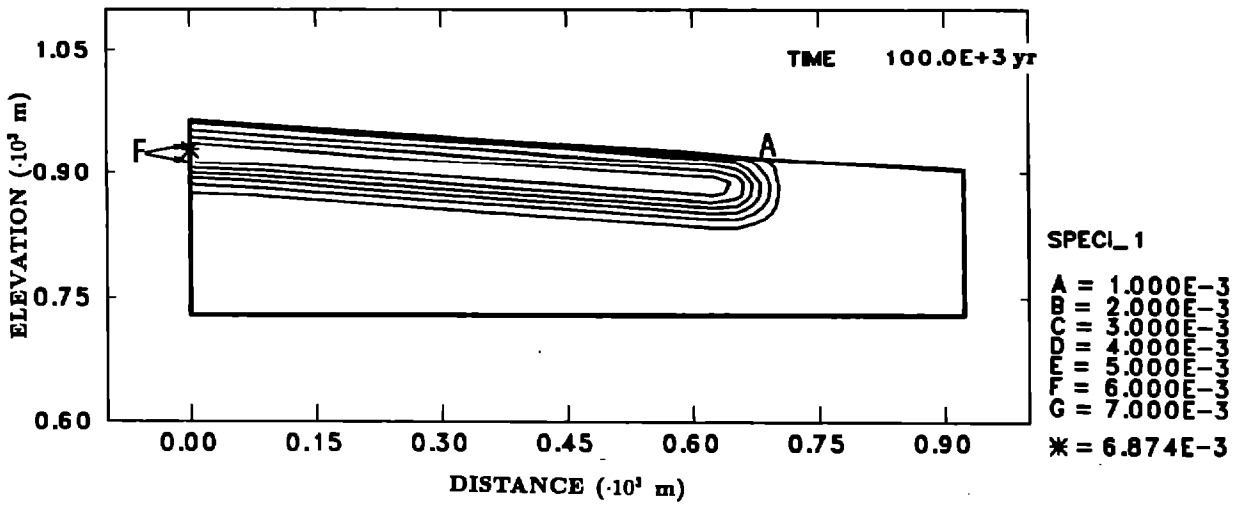

Figure 52. Concentration (curie/m^3) of Tc-99 for 0.1 mm/yr infiltration and Case 3 release at 100,000 yr.

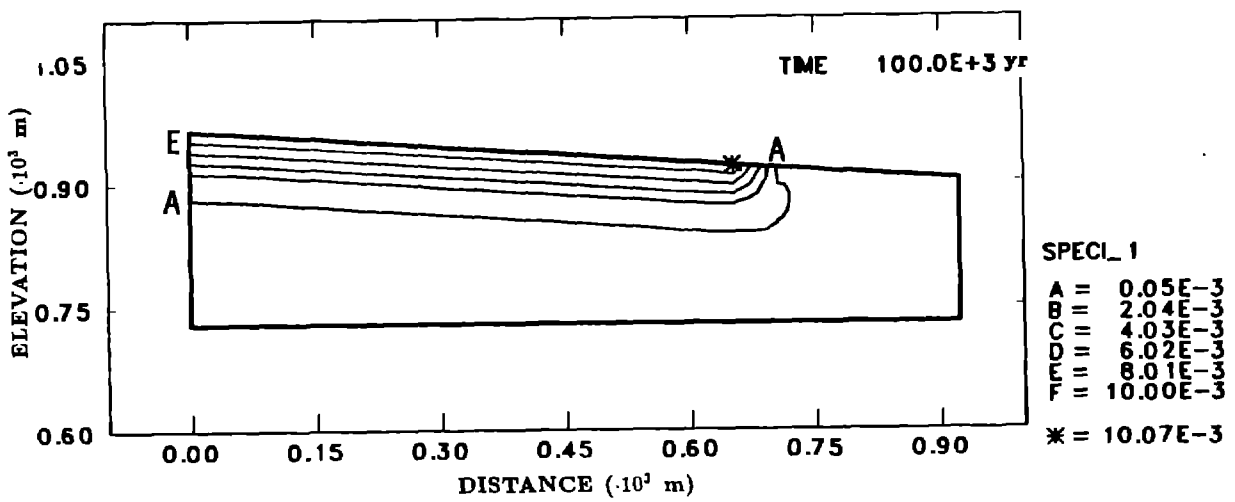

Figure 53. Concentration (curie/m^3) of Tc-99 for 0.1 mm/yr infiltration and Case 4 release at 100,000 yr.

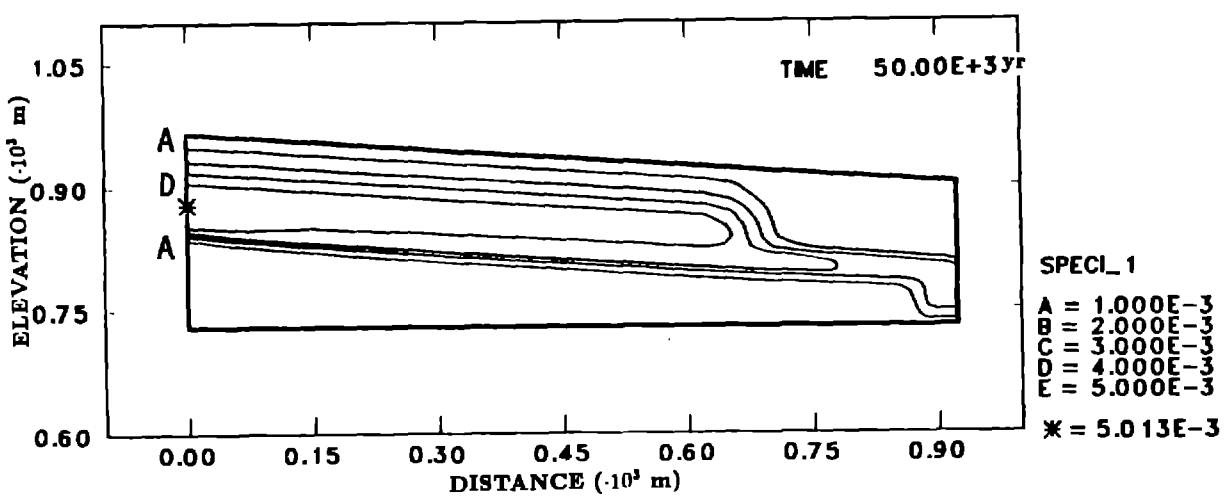

Figure 54. Concentration (curie/m^3) of Tc-99 for 0.5 mm/yr infiltration and Case 3 release at at 50,000 yr.

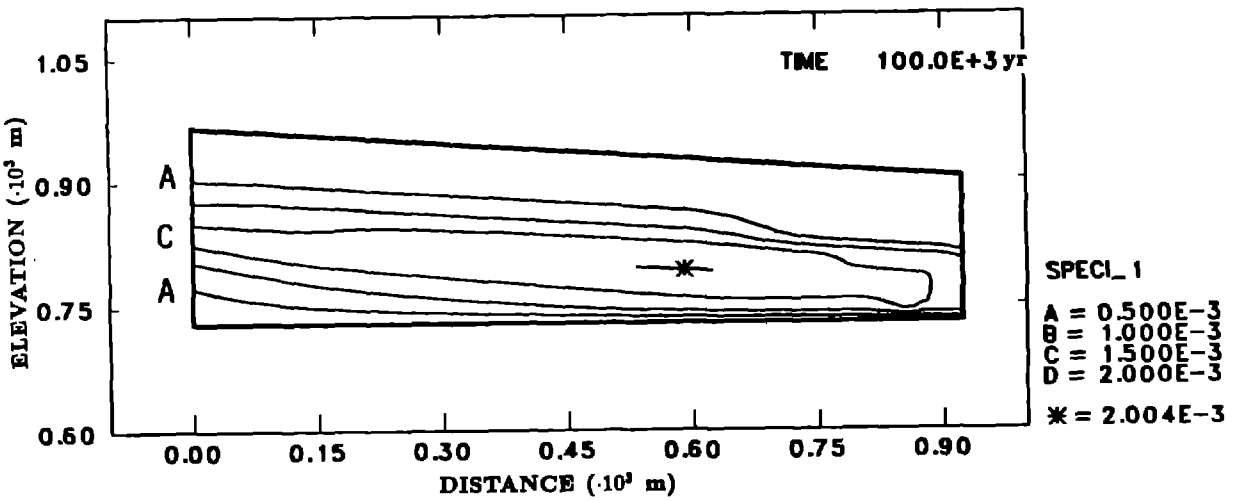

Figure 55. Concentration (curie/m^3) of Tc-99 for 0.5 mm/yr infiltration and Case 3 release at 100,000 yr.

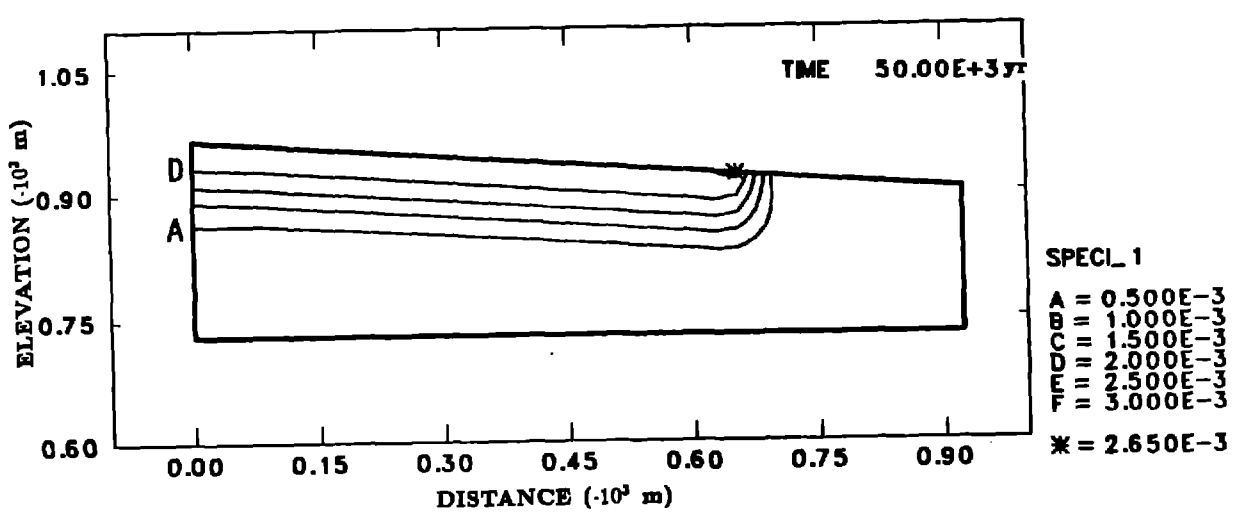

Figure 56. Concentration (curie/m^3) of Tc-99 for 0.5 mm/yr infiltration and Case 4 release at 50,000 yr.

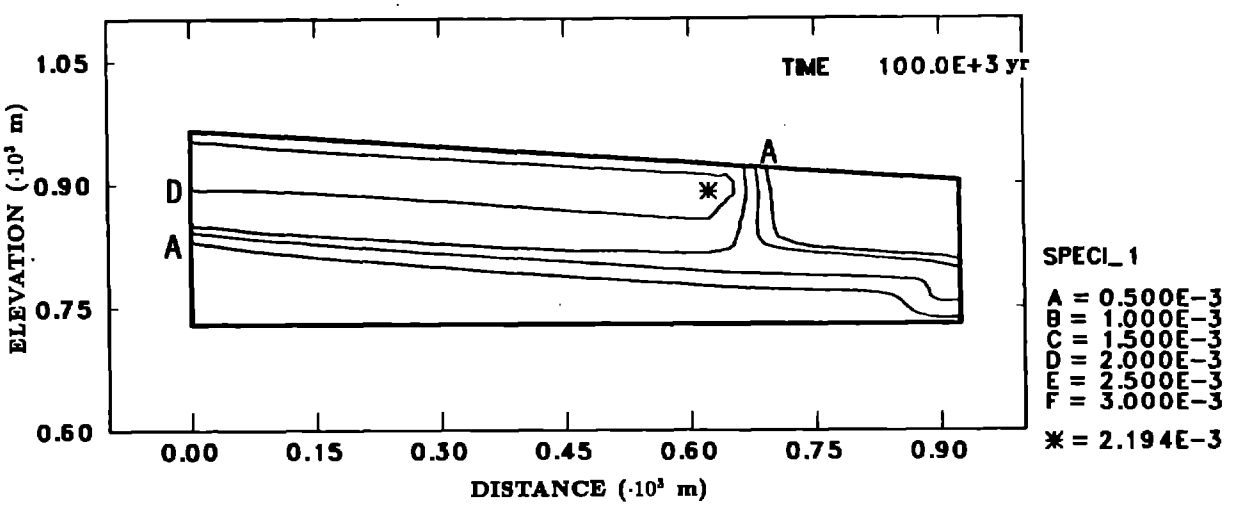

Figure 57. Concentration (curie/m^3) of Tc-99 for 0.5 mm/yr infiltration and Case 4 release at 100,000 yr.

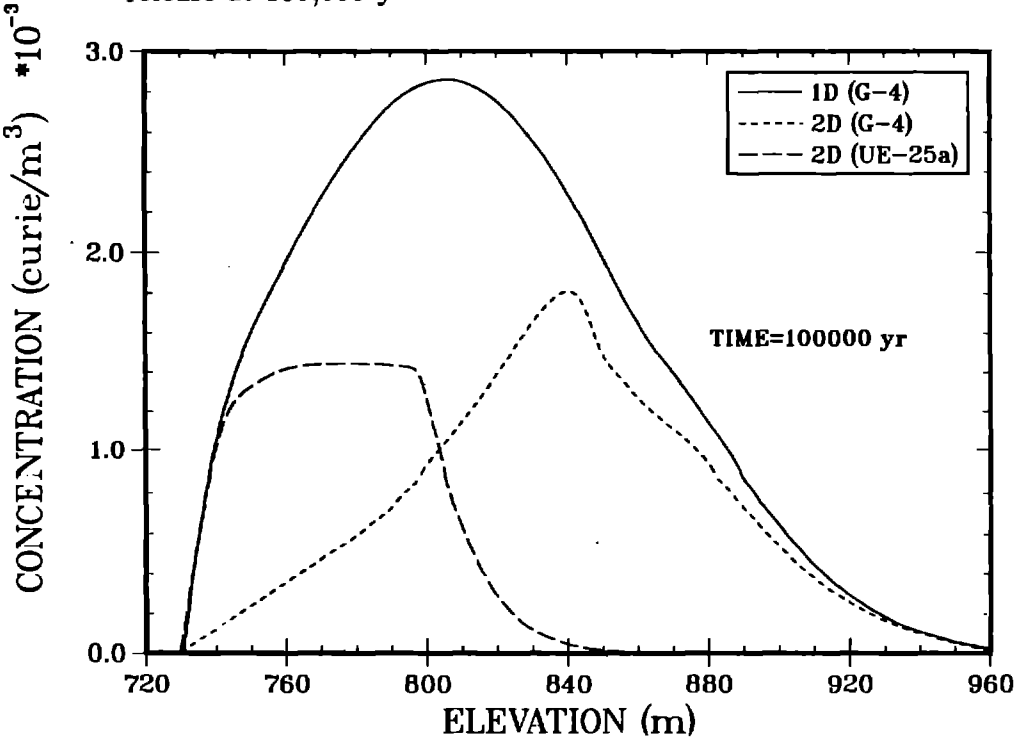

Figure 58. Concentration of Tc-99 at 100,000 yr along Holes G-4 and UE-25a for 0.5 mm/yr infiltration and Case 3 release.

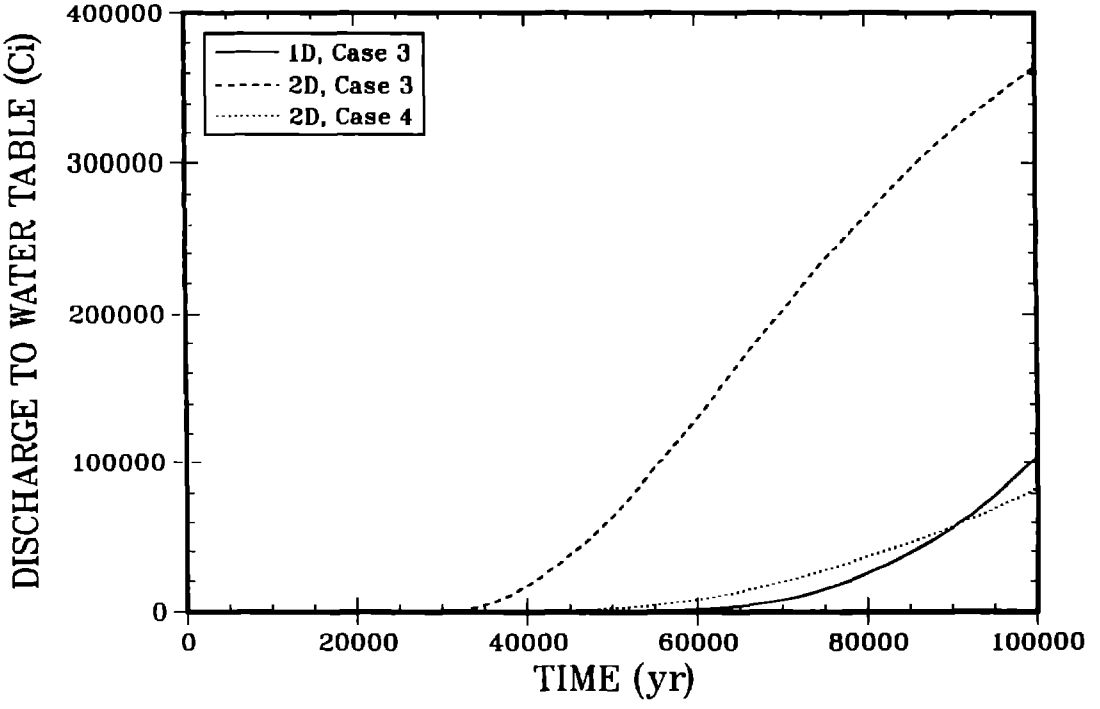

Figure 59. Cumulative discharge of Tc-99 to the water table for 0.5 mm/yr infiltration and Case 3 and 4 release models.

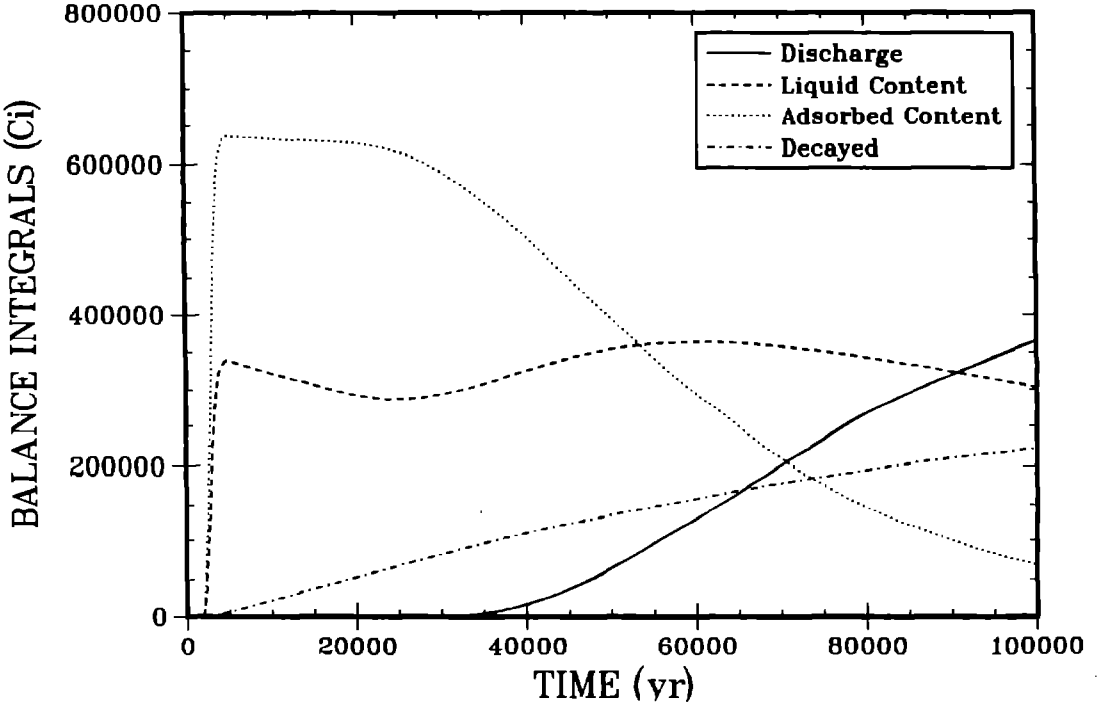

Figure 60. Cumulative balance integrals for Tc-99 for 0.5 mm/yr infiltration and the Case 3 release model.

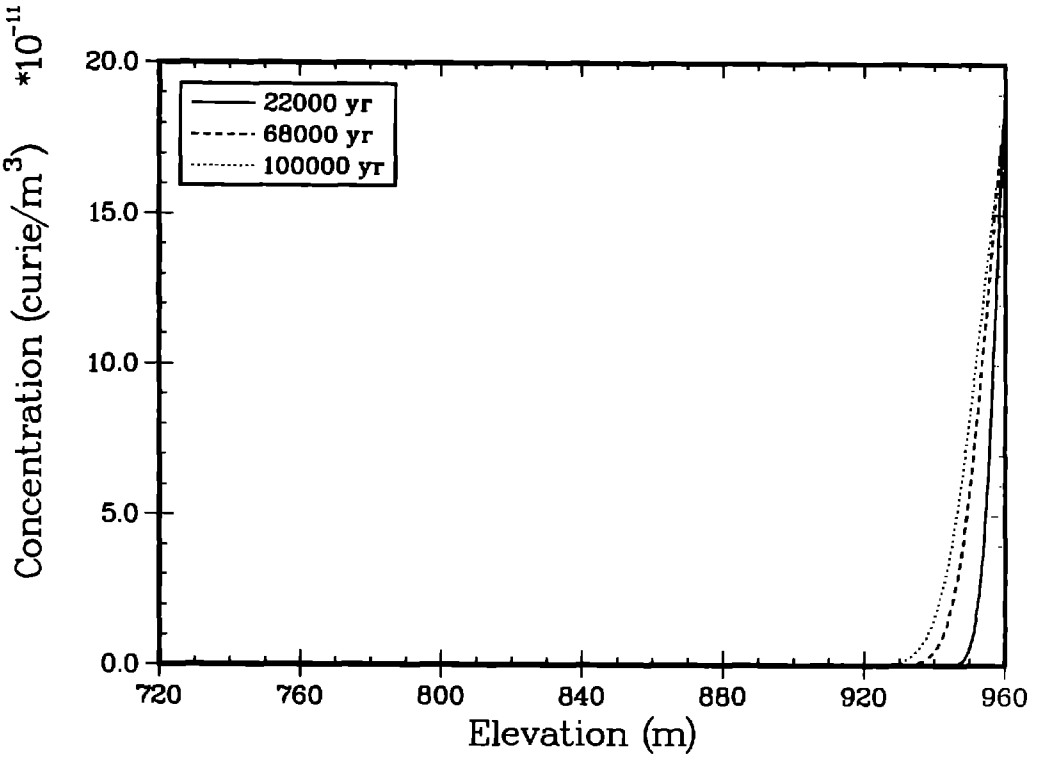

Figure 61. Concentration of Np-237 along Hole G-4 (1-D geometry) for 0.5 mm/yr infiltration and Case 3 release.

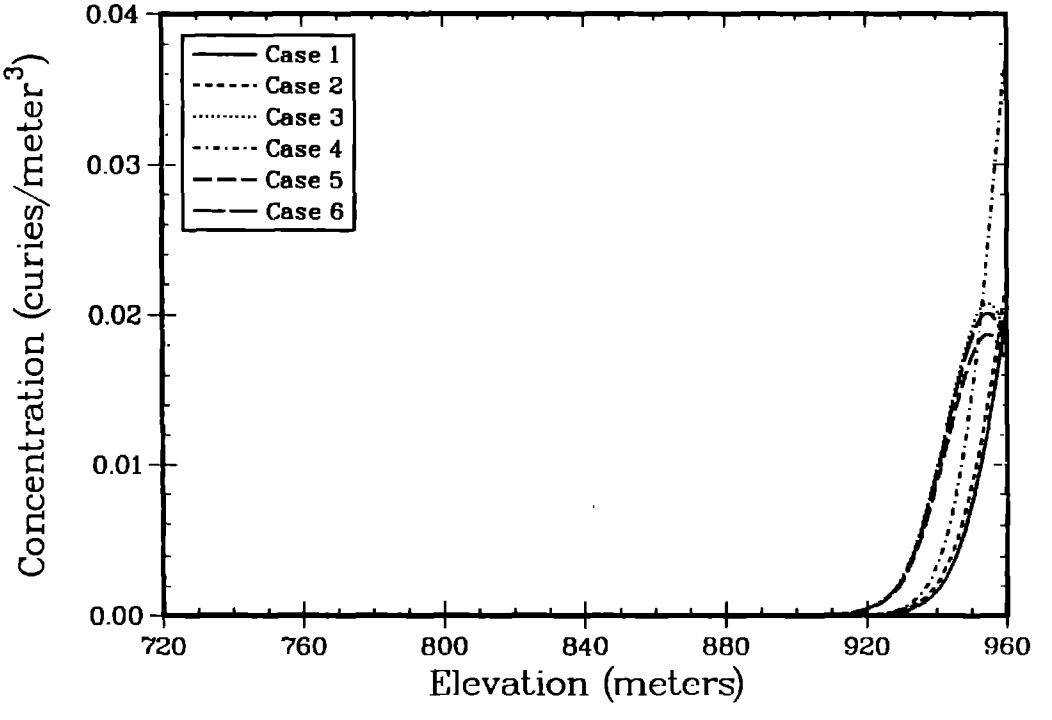

Figure 62. Concentration of Tc-99 along Hole G-4 (1-D geometry) for 0.01 mm/yr infiltration, 100,000 yr, releases for Cases 1 through 6, dual continuum.

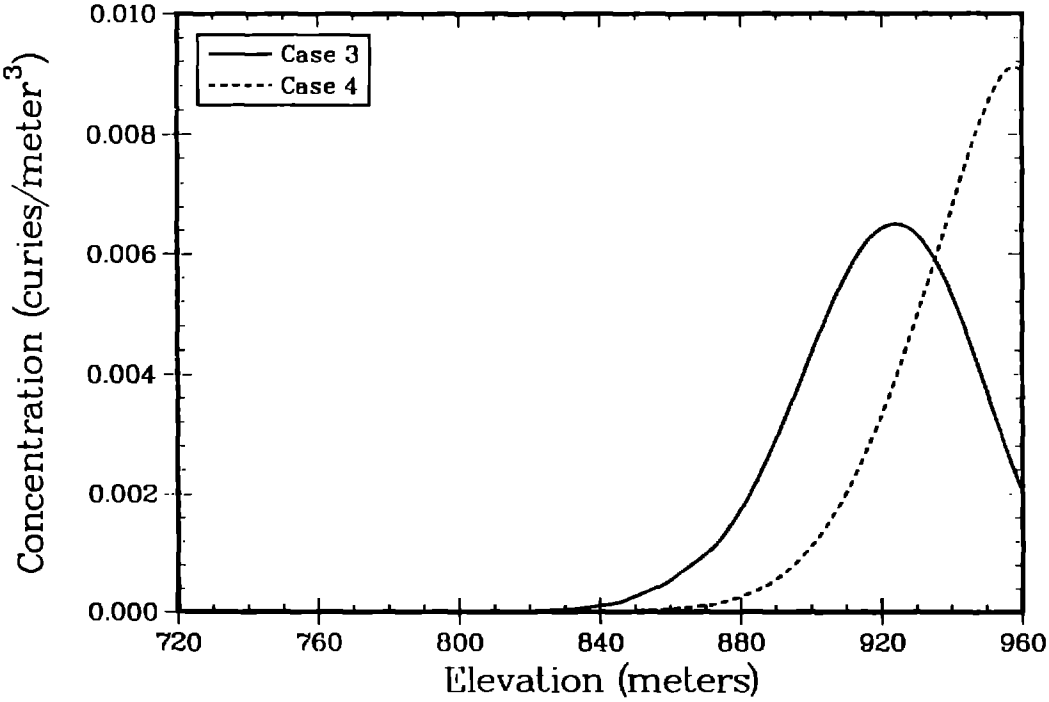

Figure 63. Concentration of Tc-99 along Hole G-4 (1-D geometry) for 0.1 mm/yr infiltration, releases for Cases 3 and 4, dual continuum, at 100,000 years.

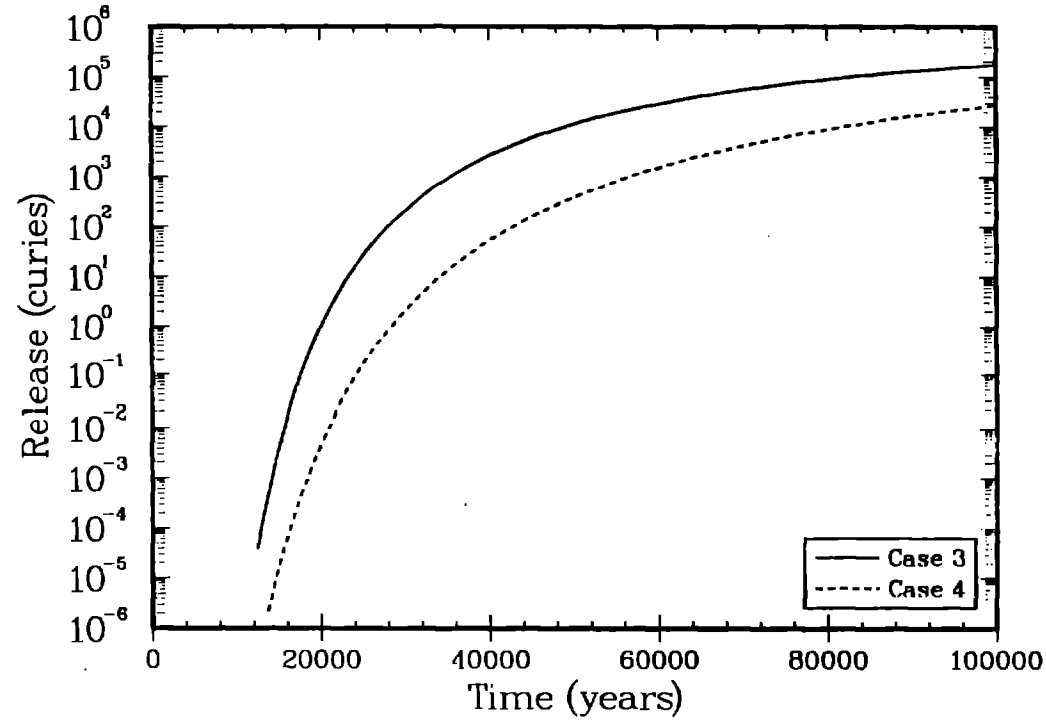

Figure 64. Integrated release of Tc-99 to water table, Cases 3 and 4, 0.5 mm/yr, dual continuum.

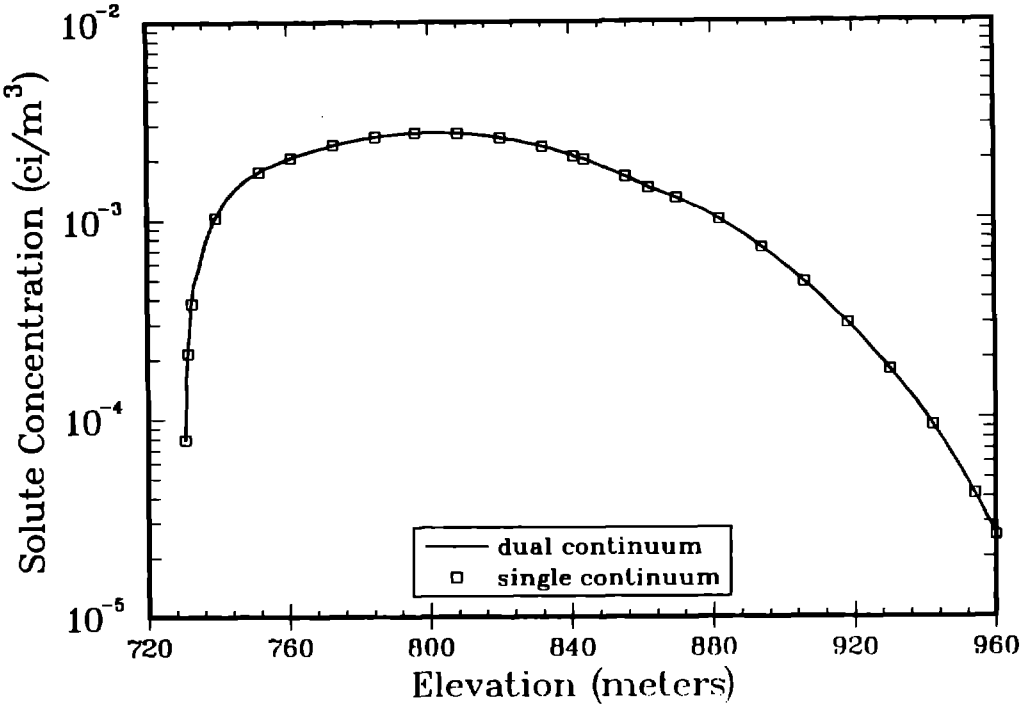

Figure 65. Comparsion of dual and single continuum models for Tc-99, Case 3, 0.5 mm/yr, solute distribution.

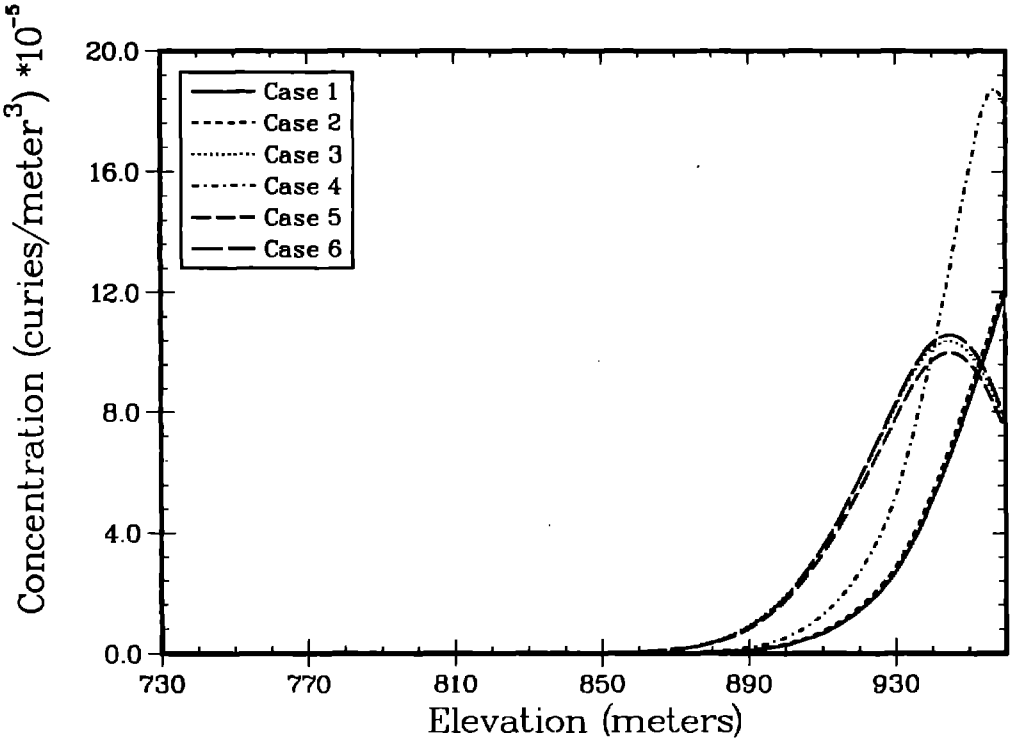

Figure 66. Concentration of I-129 along Hole G-4 (1-D geometry) for 0.01 mm/yr infiltration, 100,000 yr, Cases 1 through 6, dual continuum.

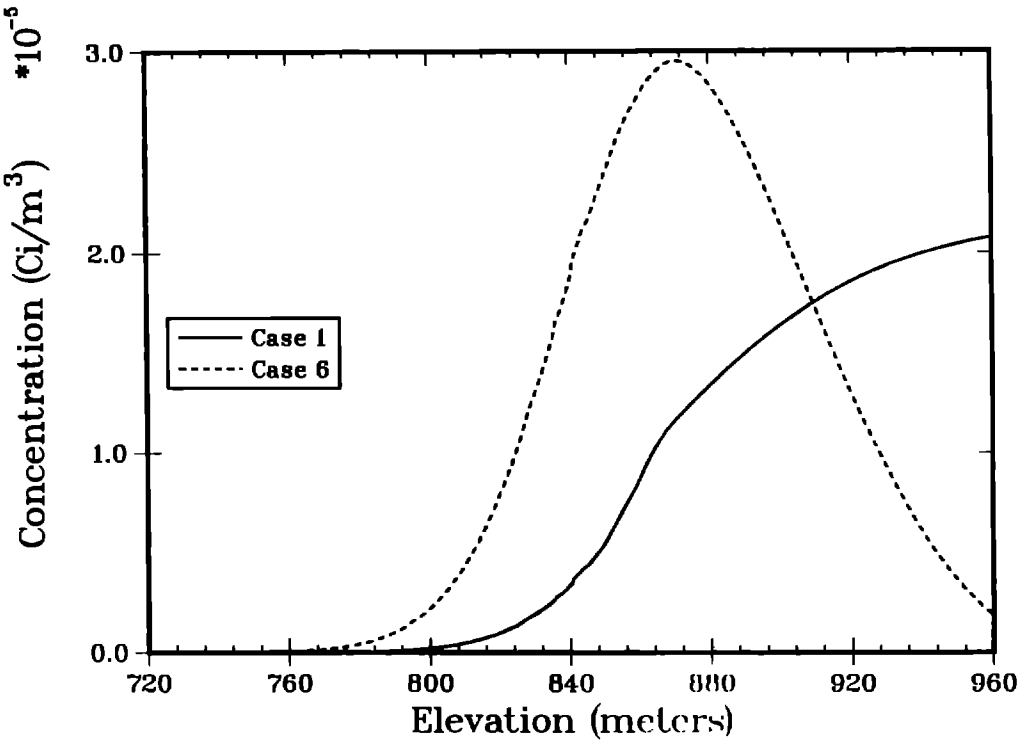

Figure 67. Concentration of I-129 along Hole G-4 (1-D geometry) for 0.1 mm/yr infiltration, 100,000 yr, Cases 1 and 6, dual continuum.

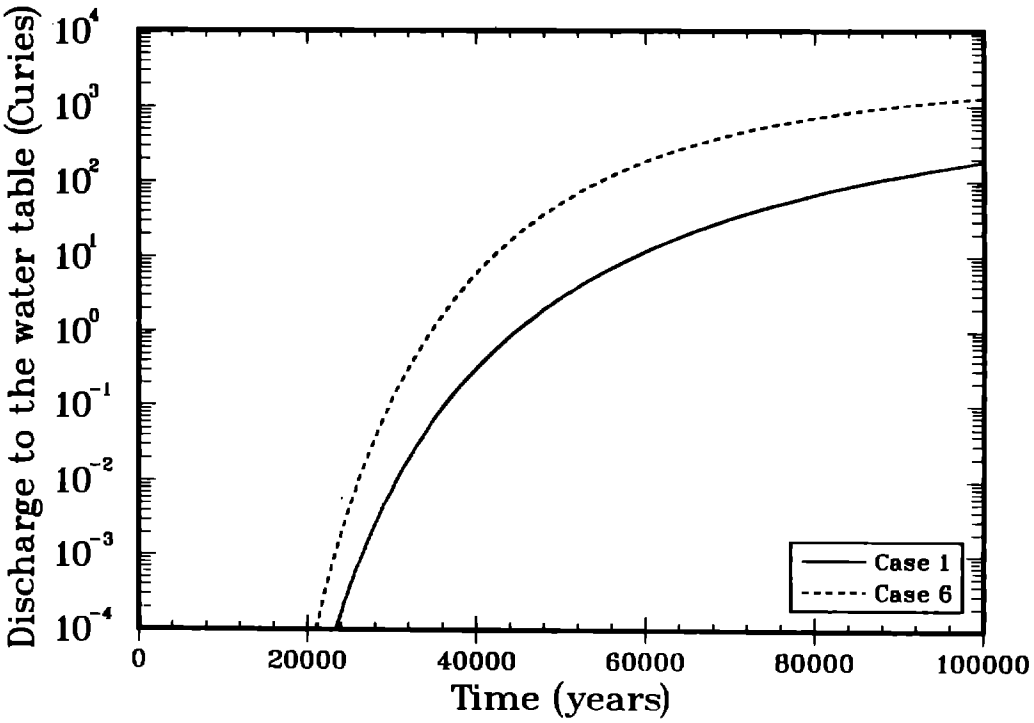

Figure 68. Integrated release of I-129 to water table, Cases 1 and 6, 0.5 mm/yr infiltration, dual continuum.

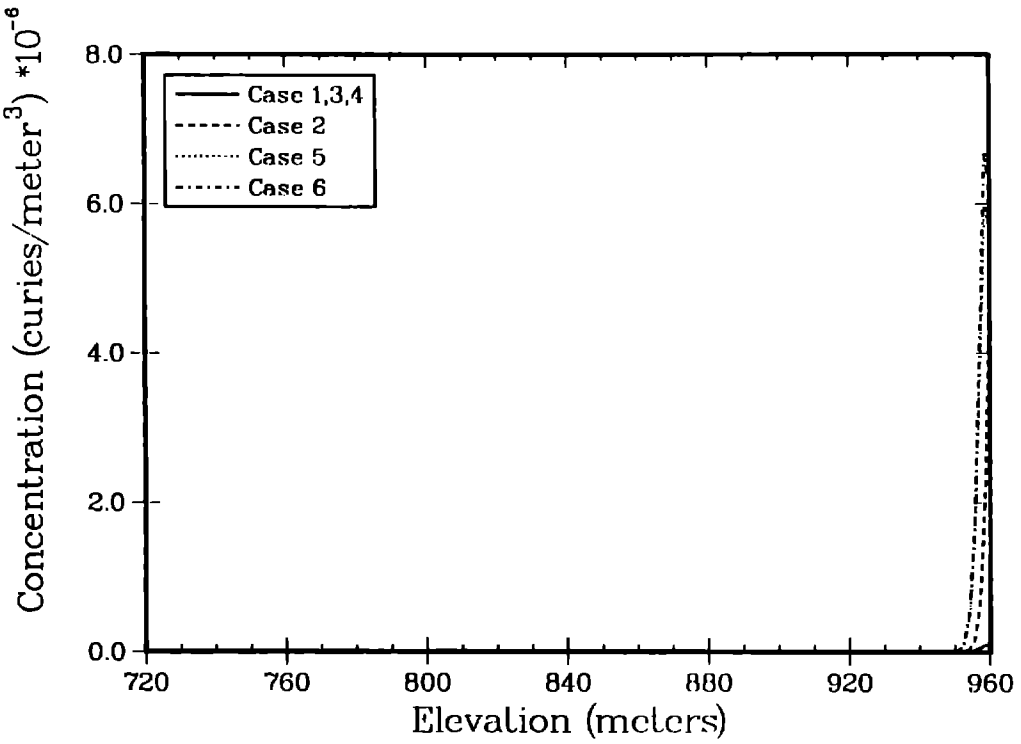

Figure 69. Concentration of Cs-135 along Hole G-4 (1-D geometry) for 0.5 mm/yr infiltration, 100,000 yr, releases for Cases 1 through 6, dual continuum.

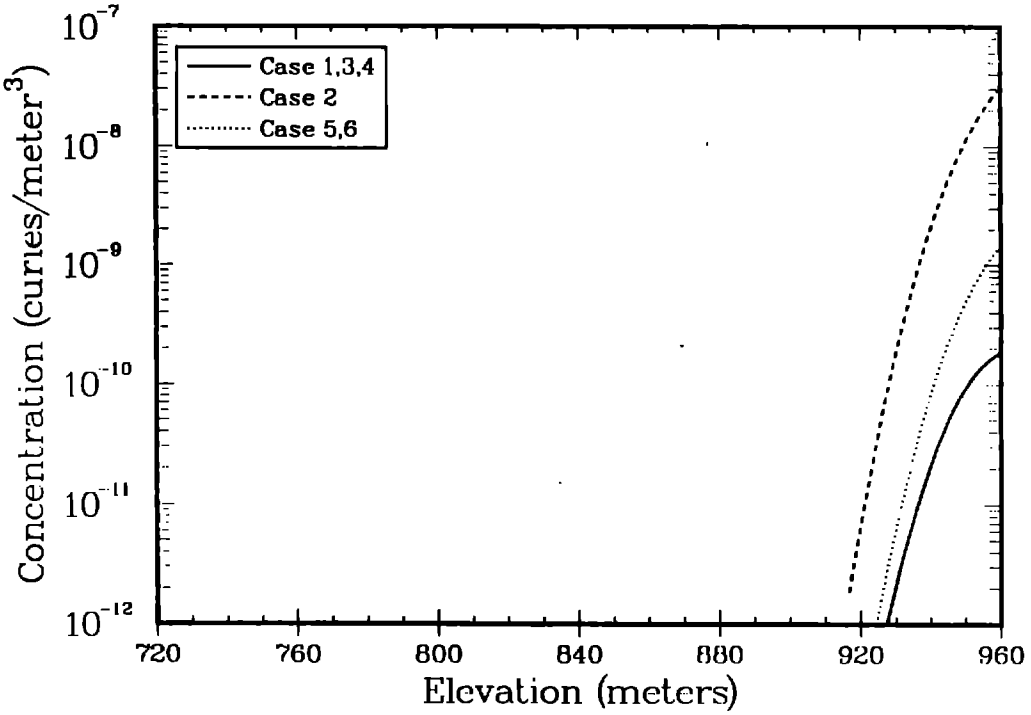

Figure 70. Concentration of Np-237 along Hole G-4 (1-D geometry) for 0.5 mm/yr infiltration, 100,000 yr, releases for Cases 1 through 6, dual continuum.

Appendix A. Material Properties

Material properties for 4 drillholes (G-1, H-1, G-4, and UE-25a), each with 22 different hydrologic layers are given below. These tables were compiled by Merlin Wheeler of Los Alamos Technical Associated, Incorporated. Material properties for a total of 22 hydrological units are given. Additionally, retention parameters for four radionuclides are defined. The repository and water table elevations are also given.

Table A.1 presents the drillhole location data. Table A.2 and A.3 present the material properties found from the drillhole cores for the matrix flow subsystem. The fracture properties are given in Table A.4.

Source terms for releases of radionuclides from the waste canisters were also provided. These source terms are plotted in Figures 34 through 37 in this report.

Finally, retention coefficients were given for the four representive radionuclides. These are given in Table A.5.

Table A.1. DRILLHOLE LOCATIONS (meters)

Drillhole	Easting	Northing	Surface Elev.	Water Table Elev.
USW G-1	170992.9	234848.5	1325.5	746.3
USW G-4	171627.3	233417.9	1270.1	730.6
USW H-1	171415.9	234773.5	1302.8	731.4
UE-25a	172623.5	233141.6	1198.7	728.8

Table A.2. MATERIAL PROPERTIES, DRILLHOLES G-4 AND UE-25a (Van Genuchten Coefficients)

Unit	Total Poros	Bulk Density g/cm^3	K_s Matrix m/sec	α m^{-1}	β	S_r	Grain Density g/cm^3	G-4 Elev. m	UE-25a Elev. m
UO(a)								1219.2	1137.7
Tpc-TN	.50	1.14	2.0E-11	0.004	1.5	0.15		1212.2	1127.1
Tpc-BT	.22	1.95	2.4E-6	0.016	10.0	0.10	2.45	1200.6	1116.4
Tpt-TM	.10	2.30	2.0E-11	0.005	1.9	0.10	2.57	1183.2	1093.6
Tpt-TD	.06	2.45	5.0E-12	0.004	2.0	0.15		1148.2	1073.7
Tpt-TDL	.08	2.40	2.0E-12	0.003	1.8	0.10		1082.9	1006.4
Tpt-TML	.12	2.25	2.0E-11	0.01	1.7	0.05	2.50	930.2	871.1
Tpt-TM	.10	2.30	2.0E-11	0.005	1.9	0.10	2.53	868.6	810.7
Tpt-TV	.04	2.25	3.0E-12	0.002	1.7	0.0	2.38	860.1	797.3
Tpt-TNV	.20	1.90	2.4E-6	0.03	2.2	0.15		850.9	787.2
Tpt-TN	.36	1.54	3.0E-12	0.02	1.2	0.0	2.35	841.2	784.2
Tpt-BT	.23	1.79	2.0E-11	0.002	1.6	0.10	2.32	840.6	783.3
Tcb-TN	.36	1.54	1.0E-11	0.004	1.5	0.15	2.28	836.0	776.9
Tcb-BT	.23	1.79	2.0E-11	0.002	1.6	0.10	2.32	835.4	775.9
Tcb-TN	.36	1.54	1.0E-11	0.004	1.5	0.15	2.28	829.0	743.9
Tcb-BT	.23	1.79	2.0E-11	0.002	1.6	0.10	2.32	826.3	739.1
Tcb-TN	.36	1.54	1.0E-11	0.004	1.5	0.15	2.28	794.6	716.5
Tcb-BT	.23	1.79	2.0E-11	0.002	1.6	0.10	2.32	793.7	715.6
Tcb-TN	.36	1.54	1.0E-11	0.004	1.5	0.15	2.28	750.4	653.4
Tcb-BT	.23	1.79	2.0E-11	0.002	1.6	0.10	2.32	733.3	639.4
Tcpp-TN	.28	1.60	5.0E-12	0.001	3.0	0.20	2.33	730.6	630.3
Tcpp-TN	.28	1.60	1.0E-11	0.004	1.6	0.15	2.33	721.4	604.4
Tcpp-TP	.25	1.90	5.0E-8	0.01	2.7	0.05	2.59	660.5	584.9

Table A.3. MATERIAL PROPERTIES, DRILLHOLES G-1 AND H-1 (Van Genuchten Coefficients)

Unit	Total Poros	Bulk Density g/cm^3	K_s Matrix m/sec	α m^{-1}	β	S_r	Grain Density g/cm^3	G-1 Elev. m	H-1 Elev. m
UO(a)								1280.2	1241.8
Tpc-TN	.50	1.14	2.0E-11	0.004	1.5	0.15		1264.5	1225.1
Tpc-BT	.22	1.95	2.4E-6	0.016	10.0	0.10	2.45	1253.8	1217.8
Tpt-TM	.10	2.30	2.0E-11	0.005	1.9	0.10	2.57	1243.2	1207.1
Tpt-TD	.06	2.45	5.0E-12	0.004	2.0	0.15		1191.9	1167.2
Tpt-TDL	.18	2.06	2.0E-12	0.005	1.52	0.0		1084.7	1048.6
Tpt-TML	.12	2.23	2.0E-11	0.005	1.52	0.0	2.50	959.7	923.7
Tpt-TM	.08	2.30	2.0E-11	0.005	1.49	0.0	2.53	933.2	895.9
Tpt-TV	.04	2.32	4.0E-11	0.005	1.46	0.0	2.38	916.4	883.7
Tpt-TNV	.33	1.59	3.0E-10	0.02	4.0	0.20		900.6	852.6
Tpt-TN	.36	1.57	3.0E-12	0.02	1.20	0.0	2.35	897.8	850.5
Tpt-BT	.24	2.00	7.0E-12	0.003	1.65	0.06		891.1	843.8
Tcb-TN	.36	1.57	2.0E-11	0.005	1.37	0.0	2.28	856.4	809.1
Tcb-BT	.24	2.00	7.0E-12	0.003	1.65	0.06	2.32	855.8	808.5
Tcb-TN	.36	1.57	2.0E-11	0.005	1.37	0.0	2.28	850.9	803.6
Tcb-BT	.24	2.00	7.0E-12	0.003	1.65	0.06	2.32	850.2	802.9
Tcb-TN	.36	1.57	2.0E-11	0.005	1.37	0.0	2.28	846.9	799.6
Tcb-BT	.24	2.00	7.0E-12	0.003	1.65	0.06	2.32	846.6	799.3
Tcb-TN	.36	1.57	2.0E-11	0.005	1.37	0.0	2.28	796.3	749.0
Tcb-BT	.24	2.00	7.0E-12	0.003	1.65	0.06	2.32	776.2	736.8
Tcpp-TN	.28	1.60	4.0E-12	0.006	1.48	0.00	2.33	767.7	729.8
Tcpp-TN	.28	1.60	2.0E-11	0.02	1.4	0.00	2.33	746.3	693.2
Tcpp-TP	.25	1.90	2.0E-5	0.01	2.7	0.05	2.59	715.9	693.2

Table A.4. FRACTURE PROPERTIES (Van Genuchten Coefficients)

Unit	Porosity	Frequency $no./m^3$	$K_{f,s}$ m/sec	Aperature μm	α $1/m$	β	S_r
Tpt-TM	3.E-5	5	4.E-5	6	1.28	4.23	0.04
Tpt-TD	3.E-5	5	4.E-5	6	1.28	4.23	0.04
Tpt-TDL	1.8E-5	3	4.E-5	6	1.28	4.23	0.04
Tpt-TML	3.E-5	5	4.E-5	6	1.28	4.23	0.04
Tpt-TM	3.E-5	5	4.E-5	6	1.28	4.23	0.04
Tpt-TV	2.E-4	10	4.E-5	20	1.28	4.23	0.04
Tpt-TNV	6.6.E-5	3	4.E-5	22	1.28	4.23	0.04
Tpt-TN	9.E-5	3	8.E-5	30	1.28	4.23	0.04
Tpt-BT	1.8.E-5	3	3.E-5	6	1.28	4.23	0.04
Tcb-TN	1.8E-5	3	3.E-5	6	1.28	4.23	0.04
Tcb-BT	1.8E-5	3	3.E-5	6	1.28	4.23	0.04
Tcpp-TN	3.E-5	3	3.E-5	6	1.28	4.23	0.04
Tcpp-TP	3.E-5	3	4.E-5	20	1.28	4.23	0.04

Table A.5. SOLUTE SORPTION COEFFICIENTS

Unit	Cs-135	Np-237	Tc-99	I-129
Tpt-TM	100	5.0	0.1	0.0
Tpt-TD	100	5.0	0.1	0.0
Tpt-TDL	100	5.0	0.1	0.0
Tpt-TML	100	5.0	0.1	0.0
Tpt-TM	100	5.0	0.1	0.0
Tpt-TV	100	0.5	0.05	0.0
Tpt-TNV	0.	0.	0.	0.0
Tpt-TN	3000	3.0	0.	0.0
Tpt-BT	3000	3.0	0.	0.0
Tcb-TN	3000	3.0	0.	0.0
Tcb-BT	3000	3.0	0.	0.0
Tcpp-TN	200	5.0	0.	0.0
Tcpp-TP	200	5.0	0.	0.0

Appendix B. Reference Information Base

Information from the Reference Information Base Used in this Report

This report contains no information from the Reference Information Base.

Candidate Information for the Reference Information Base

This report contains no candidate information for the Reference Information Base.

Candidate Information for the Site & Engineering Properties Data Base

This report contains no candidate information for the Site and Engineering Properties Data Base.

DISTRIBUTION LIST

1 J. W. Bartlett, Director (RW-1)
Office of Civilian Radioactive
Waste Management
U.S. Department of Energy
1000 Independence Avenue, S.W.
Washington, D.C. 20585

1 F. G. Peters, Deputy Director (RW-2)
Office of Civilian Radioactive
Waste Management
U.S. Department of Energy
1000 Independence Avenue, S.W.
Washington, D.C. 20585

1 T. H. Isaacs (RW-4)
Office of Strategic Planning
and International Programs
Office of Civilian Radioactive
Waste Management
U.S. Department of Energy
1000 Independence Avenue, S.W.
Washington, D.C. 20585

1 J. D. Saltzman (RW-5)
Office of External Relations
Office of Civilian Radioactive
Waste Management
U.S. Department of Energy
1000 Independence Avenue, S.W.
Washington, D.C. 20585

1 Samuel Rousso (RW-10)
Office of Program and Resources
Management
Office of Civilian Radioactive
Waste Management
U.S. Department of Energy
1000 Independence Avenue, S.W.
Washington, D.C. 20585

1 J. C. Bresee (RW-10)
Office of Civilian Radioactive
Waste Management
U.S. Department of Energy
1000 Independence Avenue, S.W.
Washington, D.C. 20585

1 C. P. Gertz (RW-20)
Office of Geologic Disposal
Office of Civilian Radioactive
Waste Management
U.S. Department of Energy
1000 Independence Avenue, S.W.
Washington, D.C. 20585

1 S. J. Brocoum (RW-22)
Analysis and Verification Division
Office of Civilian Radioactive
Waste Management
U.S. Department of Energy
1000 Independence Avenue, S.W.
Washington, D.C. 20585

1 D. D. Shelor (RW-30)
Office of Systems and Compliance
Office of Civilian Radioactive
Waste Management
U.S. Department of Energy
1000 Independence Avenue, S.W.
Washington, D.C. 20585

1 J. Roberts (RW-33)
Office of Civilian Radioactive
Waste Management
U.S. Department of Energy
1000 Independence Avenue, S.W.
Washington, D.C. 20585

1 G. J. Parker (RW-332)
Office of Civilian Radioactive
Waste Management
U.S. Department of Energy
1000 Independence Avenue, S.W.
Washington, D.C. 20585

1 Associate Director (RW-40)
Office of Storage and Transportation
Office of Civilian Radioactive
Waste Management
U.S. Department of Energy
1000 Independence Avenue, S.W.
Washington, D.C. 20585

1 Associate Director (RW-50)
Office of Contract Business
Management
Office of Civilian Radioactive
Waste Management
U.S. Department of Energy
1000 Independence Avenue, S.W.
Washington, D.C. 20585

1 C. G. Russomanno (RW-52)
Office of Civilian Radioactive
Waste Management
U.S. Department of Energy
1000 Independence Avenue, S.W.
Washington, D.C. 20585

1 D. U. Deere, Chairman
Nuclear Waste Technical
Review Board
1100 Wilson Blvd. #910
Arlington, VA 22209-2297

1 Dr. John E. Cantlon
Nuclear Waste Technical Review Board
1795 Bramble Dr.
East Lansing, MI 48823

1 Dr. Melvin W. Carter
Nuclear Waste Technical Review Board
4621 Ellisbury Dr., N.E.
Atlanta, GA 30332

1 Dr. Donald Langmuir
Nuclear Waste Technical Review Board
109 So. Lookout Mountain Cr.
Golden, CO 80401

1 Dr. D. Warner North
Nuclear Waste Technical Review Board
Decision Focus, Inc.
4984 El Camino Real
Los Altos, CA 94062

1 Dr. Dennis L. Price
Nuclear Wast Technical Review Board
1011 Evergreen Way
Blacksburg, VA 24060

1 Dr. Ellis D. Verink
Nuclear Waste Technical Review Board
4401 N.W. 18th Place
Gainesville, FL 32605

5 C. P. Gertz, Project Manager
Yucca Mountain Project Office
U.S. Department of Energy
P.O. Box 98608--MS 523
Las Vegas, NV 89193-8608

1 C. L. West, Director
Office of External Affairs
DOE Field Office, Nevada
U.S. Department of Energy
P.O. Box 98518
Las Vegas, NV 89193-85180

12 Technical Information Officer
DOE Field Office, Nevada
U.S. Department of Energy
P.O. Box 98518
Las Vegas, NV 89193-8518

1 P. K. Fitzsimmons, Director
Health Physics & Environmental
Division
DOE Field Office, Nevada
U.S. Department of Energy
P.O. Box 98518
Las Vegas, NV 89193-8518

1 D. R. Elle, Director
Environmental Protection Division
DOE Field Office, Nevada
U.S. Department of Energy
P.O. Box 98518
Las Vegas, NV 89193-8518

1 Repository Licensing & Quality
Assurance Project Directorate
Division of Waste Management
U.S. Nuclear Regulatory Commission
Washington, D.C. 20555

1 Senior Project Manager for Yucca
Mountain Repository Project Branch
Division of Waste Management
U.S. Nuclear Regulatory Commission
Washington, D.C. 20555

1 NRC Document Control Desk
Division of Waste Management
U.S. Nuclear Regulatory Commission
Washington, D.C. 20555

1 P. T. Prestholt
NRC Site Representative
301 E. Stewart Ave.
Las Vegas, NV 89101

1 E. P. Binnall
Field Systems Group Leader
Building 50B/4235
Lawrence Berkeley Laboratory
Berkeley, CA 94720

1 Center for Nuclear Waste
Regulatory Analyses
6220 Culebra Road
Drawer 28510
San Antonio, TX 78284

3 L. J. Jardine
Technical Project Officer for YMP
Mail Stop L-204
Lawrence Livermore National
Laboratory
P.O. Box 808
Livermore, CA 94550

4 R. J. Herbst
Technical Project Officer for YMP
N-5, Mail Stop J521
Los Alamos National Laboratory
P.O. Box 1663
Los Alamos, NM 87545

1 H. N. Kalia
Exploratory Shaft Test Manager
Los Alamos National Laboratory
Mail Stop 527
101 Convention Center Dr.
Suite 820
Las Vegas, NV 89109

1 J. F. Divine
Assistant Director for
Engineering Geology
U.S. Geological Survey
106 National Center
12201 Sunrise Valley Dr.
Reston, VA 22092

6 L. R. Hayes
Technical Project Officer
Yucca Mountain Project Branch--MS 425
U.S. Geological Survey
P.O. Box 25046
Denver, CO 80225

1 V. R. Schneider
Asst. Chief Hydrologist--MS 414
Office of Program Coordination
& Technical Support
U.S. Geological Survey
12201 Sunrise Valley Drive
Reston, VA 22092

1 R. B. Raup, Jr.
Geological Division Coordinator
MS 913
Yucca Mountain Project
U.S. Geological Survey
P.O. Box 25046
Denver, CO 80225

1 D. H. Appel, Chief
Hydrologic Investigations Program
MS 421
U.S. Geological Survey
P.O. Box 25046
Denver, CO 80225

1 E. J. Helley
Branch of Western Regional Geology
MS 427
U.S. Geological Survey
345 Middlefield Road
Menlo Park, CA 94025

1 Chief
Nevada Operations Office
U.S. Geological Survey
101 Convention Center Drive
Suite 860, MS 509
Las Vegas, NV 89109

1 D. Zesiger
U.S. Geological Survey
101 Convention Center Dr.
Suite 860 - MS509
Las Vegas, NV 89109

1 R. V. Watkins, Chief
Project Planning and Management
U.S. Geological Survey
P.O. Box 25046
421 Federal Center
Denver, CO 80225

1 A. L. Flint
U.S. Geological Survey
MS 721
P.O. Box 327
Mercury, NV 89023

1 D. A. Beck
U.S. Geological Survey
1500 E. Tropicana, Suite 201
Las Vegas, NV 89119

1 P. A. Glancy
U.S. Geological Survey
Federal Building, Room 224
Carson City, NV 89701

1 Sherman S. C. Wu
Branch of Astrogeology
U.S. Geological Survey
2255 N. Gemini Dr.
Flagstaff, AZ 86001

1 J. H. Sass
Branch of Tectonophysics
U.S. Geological Survey
2255 N. Gemini Dr.
Flagstaff, AZ 86001

1 DeWayne A. Campbell
Technical Project Officer for YMP
Bureau of Reclamation
Code D-3790
P.O. Box 25007
Denver, CO 80225

1 S. M. Dash
Science Applications International Corp.
14062 Denver West Parkway, Suite 255
Golden, CO 80401

1 K. W. Causseaux
NHP Reports Chief
U.S. Geological Survey
421 Federal Center
P.O. Box 25046
Denver, CO 80225

1 V. M. Glanzman
U.S. Geological Survey
913 Federal Center
P.O. Box 25046
Denver, CO 80225

1 J. H. Nelson
Technical Project Officer for YMP
Science Applications International Corp.
101 Convention Center Dr.
Suite 407
Las Vegas, NV 89109

2 SAIC-T&MSS Library
Science Applications International Corp.
101 Convention Center Dr.
Suite 407
Las Vegas, NV 89109

1 Elaine Ezra
YMP GIS Project Manager
EG&G Energy Measurements, Inc.
Mail Stop D-12
P.O. Box 1912
Las Vegas, NV 89125

1 R. E. Jackson, Program Manager
Roy F. Weston, Inc.
955 L'Enfant Plaza, Southwest
Washington, D.C. 20024

1 Technical Information Center
Roy F. Weston, Inc.
955 L'Enfant Plaza, Southwest
Washington, D.C. 20024

1 D. Hedges, Vice President,
Quality Assurance
Roy F. Weston, Inc.
4425 Spring Mountain Road, Suite 300
Las Vegas, Nevada 89102

1 D. L. Fraser, General Manager
Reynolds Electrical & Engineering Co.
Mail Stop 555
P.O. Box 98521
Las Vegas, NV 89193-8521

1 R. F. Pritchett
Technical Project Officer for YMP
Reynolds Electrical & Engineering Co.
MS 408
P.O. Box 98521
Las Vegas, NV 89193-8521

1 B. W. Colston
General Manager & President
Las Vegas Branch
Raytheon Services Nevada
Mail Stop 416
P.O. Box 95487
Las Vegas, NV 89193-5487

1 R. L. Bullock
Technical Project Officer for YMP
Raytheon Services Nevada
Suite P250, MS 403
101 Convention Center Dr.
Las Vegas, NV 89109

1 R. E. Lowder
Technical Project Officer for YMP
MAC Technical Services
101 Convention Center Drive
Suite 1100
Las Vegas, NV 89109

1 C. K. Hastings, Manager
PASS Program
Pacific Northwest Laboratories
P.O. Box 999
Richland, WA 99352

1 A. T. Tamura
Science and Technology Division
Office of Scientific and Technical Information
U.S. Department of Energy
P.O. Box 62
Oak Ridge, TN 37831

1 Carlos G. Bell, Jr.
Professor of Civil Engineering
Civil and Mechanical Engineering Department
University of Nevada, Las Vegas
4505 South Maryland Parkway
Las Vegas, NV 89154

1 C. F. Costa, Director
Nuclear Radiation Assessment Division
U.S. Environmental Protection Agency
Environmental Monitoring Systems Laboratory
P.O. Box 93478
Las Vegas, NV 89193-3478

1 ONWI Library
Battelle Columbus Laboratory
Office of Nuclear Waste Isolation
505 King Avenue
Columbus, OH 43201

1 T. Hay, Executive Assistant
Office of the Governor
State of Nevada
Capitol Complex
Carson City, NV 89710

3 R. R. Loux, Jr.
Executive Director
Nuclear Waste Project Office
State of Nevada
Evergreen Center, Suite 252
1802 North Carson Street
Carson City, NV 89710

1 C. H. Johnson
Technical Program Manager
Nuclear Waste Project Office
State of Nevada
Evergreen Center, Suite 252
1802 North Carson Street
Carson City, NV 89710

1 John Fordham
Water Resources Center
Desert Research Institute
P.O. Box 60220
Reno, NV 89506

1 Dr. Martin Mifflin
Water Resources Center
Desert Research Institute
2505 Chandler Avenue
Suite 1
Las Vegas, NV 89120

1 Eric Anderson
Mountain West Research-Southwest Inc.
2901 N. Central Ave. #1000
Phoenix, AZ 85012-2730

1 Department of Comprehensive Planning
Clark County
225 Bridger Avenue, 7th Floor
Las Vegas, NV 89155

1 Planning Department
Nye County
P.O. Box 153
Tonopah, NV 89049

1 Lincoln County Commission
Lincoln County
P.O. Box 90
Pioche, NV 89043

5 Judy Foremaster
City of Caliente
P.O. Box 158
Caliente, NV 89008

1 Economic Development Department
City of Las Vegas
400 East Stewart Avenue
Las Vegas, NV 89101

1 Community Planning & Development
City of North Las Vegas
P.O. Box 4086
North Las Vegas, NV 89030

1 Director of Community Planning
City of Boulder City
P.O. Box 367
Boulder City, NV 89005

1 Commission of the European
Communities
200 Rue de la Loi
B-1049 Brussels
BELGIUM

2 M. J. Dorsey, Librarian
YMP Research and Study Center
Reynolds Electrical & Engineering
Co., Inc.
MS 407
P.O. Box 98521
Las Vegas, NV 89193-8521

1 Amy Anderson
Argonne National Laboratory
Building 362
9700 So. Cass Ave.
Argonne, IL 60439

1	6300	T. O. Hunter
1	6310	T. E. Blejwas, Actg.
1	6310A	L. E. Shephard
1	6312	F. W. Bingham
1	6312	R. W. Barnard
1	6312	H. A. Dockery
1	6312	P. G. Kaplan
1	6313	L. S. Costin
1	6315	F. B. Nimick, Actg.
1	6316	R. P. Sandoval
2	6318	R. J. Macer for 100/12149/SAND90-3165/NQ
1	6319	R. R. Richards

1	1510	J. C. Cummings
1	1511	J. S. Rottler
1	1511	R. R. Eaton
1	1511	P. L. Hopkins
1	1511	M. J. Martinez
1	1513	R. C. Dykhuizen
1	1513	R. D. Skocypec
5	3141	S. A. Landenberger
8	3145	Document Processing for DOE/OSTI
3	3151	G. C. Claycomb
20	6341	WMT Library
1	6410	D. J. McCloskey, Actg.
1	8523-2	Central Technical Files

SAND90-3165

The number in the lower right-hand corner is an accession number used for Office of Civilian Radioactive Waste Management purposes only. It should not be used when ordering this publication.

NNA.911202.0032

Org.	Bldg.	Name	Rec'd by	Org.	Bldg.	Name	Rec'd by

Sandia National Laboratories